8-2018

Micropropulsion Trade Study and Investigation for Attitude Control of Nanosatellites

Katherine L. Fowee
Purdue University

MICROPROPULSION TRADE STUDY AND INVESTIGATION FOR ATTITUDE CONTROL OF NANOSATELLITES

A Thesis

Submitted to the Faculty

of

Purdue University

by

Katherine L. Fowee

In Partial Fulfillment of the

Requirements for the Degree

of

Master of Science

August 2018

Purdue University

West Lafayette, Indiana

THE PURDUE UNIVERSITY GRADUATE SCHOOL
STATEMENT OF THESIS APPROVAL

Dr. Alina Alexeenko, Chair

School of Aeronautics and Astronautics

Dr. Alexey Shashurin

School of Aeronautics and Astronautics

Dr. Stephen Heister

School of Aeronautics and Astronautics

Dr. Jordi Puig-Suari

California Polytechnic State University, Aerospace Engineering

Approved by:

Dr. Wayne Chen

Head of the School of Aeronautics and Astronautics Graduate Program

Mom and Dad for making me a space cadet.

Jordan for keeping one of my feet on the ground.

My teachers and mentors for giving me my wings.

sic itur ad astra

ACKNOWLEDGMENTS

I would like to acknowledge several people who have helped me reach my academic success so far. I would first like to thank Prof. Alexeenko for being a fantastic advisor and a role model for success as a female engineer. Thank you for your patience, your encouragement, and for giving me a chance. Thank you to my committee, to the School of Aeronautics and Astronautics, and the team at NASA for teaching me more in the last two years than I think I learned in the previous four. Thank you to Prof. Macheret for allowing me to experience teaching and realize that spreading knowledge is as rewarding as gaining knowledge. Thank you to my "kiddos", who did phenomenal work with FEMTA and taught me probably more than I taught them.

Thank you to Prof. Dumbacher, who took my passion for space from a small fire to an SSME. Thanks for the chance of a lifetime at EFT1 and for helping me go to Space Prom. You turned me into more than just a rocket scientist

Thank you to my research group for the support and camaraderie. You all have made me feel like I belong since I was an undergrad. Special thanks to Tony for being patient and being a phenomenal teacher. There is no one else I would rather spend 8 hours in the clean room with.

Thank you to the Winn Machine for kindly donating material and labor to the second iteration FEMTA duplex thrust cells. The Gasaways have always been so interested and helpful throughout this process.

Thank you Mac, for being a shoulder (albeit a bony one) since fall 2014. Thanks for helping me set up the model and for being a great friend. Thank you Liesl, for the ice cream trips, the movies, the sing-alongs, and your undying humor. We are going to kill these next few years. Thank you Dukes, for being my Aero-Bae (and introducing me to Liesl). When we are both running the Moon and Mars one day, we will still meet up for grilled cheese and tomato soup for two.

Thank you Jordan, for everything. You are supportive and bring me joy on even the most frustrating of days. You manage to remind me that, "Hey now, this is what dreams are made of" and you remind me that there is life outside of academia. I love you a million Swedish Fish.

Thank you to my family. I have been blessed with many advantages in life, not the least of which is a family that has supported and encouraged my educational endeavors. And special thanks to my parents, how made sure I was curious about everything. Mom, and every choice you have helped me make has turned out well. and best proof reader ever. Thank you for being an amazing role model and for teaching me to never procrastinate. Dad, we saw a rocket launch. I know you thought I might be a history major, but, in all honesty, there is no way I was ever going to be anything other than what I am. One of these days, I'll be like you and patent a graph.

TABLE OF CONTENTS

Page

LIST OF TABLES

Table Page

LIST OF FIGURES

Figure Page

SYMBOLS

m	mass
v	velocity
v_e	exit velocity
θ	angle
P	power
P_{in}	power input
p	pressure
ρ	density
Isp	specific impulse
F	force or thrust
I	impulse
$\dot{m}$	mass flow rate
t	time
τ	shear stress
$\bar{\tau}$	torque
$\bar{H}$	angular momentum
$\bar{\omega}$	angular velocity
$\bar{\Omega}$	change in angle
$\mathbf{I}$	moment of inertia
$\bar{r}$	moment arm
T	temperature

ABBREVIATIONS

CMG	Control-Momentum Gyroscope
FEMTA	Film Evaporation MEMS Tunable Array
MEMS	Microelectromechanical System
PPT	Pulsed Plasma Thruster
FEEP	Field Emission Electric Propulsion
SEM	Scanning Electron Microscope
MCS	Momentum Control System

ABSTRACT

Fowee, Katherine L. M.S., Purdue University, August 2018. Micropropulsion Trade Study and Investigation for Attitude Control of Nanosatellites . Major Professor: Alina A. Alexeenko.

Since their inception two decades ago, CubeSats have become dominant in the small satellite market, enabling new mission architectures, technology development, and education opportunities. However, the limited mass, power, and volume inherent in this small platform, constrains the on board subsystems and thus the capabilities compared to larger satellites. Attitude control is essential to maximizing the potential of CubeSats and other nanosatellites, though traditional momentum control systems such as reaction wheels are not feasible on the smallest CubeSats. Micropropulsion is an intriguing alternative to traditional methods, and many miniaturization efforts have been made for chemical and electrical propulsion systems. One such micropropulsion unit is Film Evaporation Microelectromechanical System Tunable Array (FEMTA). FEMTA manipulates the temperature dependence of liquid water capillary action to produce controllable and precise thrust in the 10 to 100 microNewton range. FEMTA has been demonstrated in both thrust tests and in single axis rotation tests. This work describes the further characterization of FEMTA technology through these tests and compares it to other micropropulsion technologies in a trade study for micropropulsion as attitude control devices on various sizes of CubeSats.

1. INTRODUCTION

1.1 Motivation and Research Objectives

The first man-made spacecraft launched into orbit was the aptly named Sputnik 1 (Спутник is Russian word for satellite) in 1957, propelling the world of technology development into orbit with it. In the 60 years since Sputnik 1, technology has seen a major shift in our reliance on land based systems to our reliance on space based systems creating a global market: Businesses rely on satellite based communications systems, the military depend upon satellite surveillance for intelligence, and citizens rely on global positioning systems for navigation.

Sputnik 1 was 83.6 kg, 23 inch sphere that weighed 184lbs [1]. From there, satellites and deep space probes grew as launch vehicles became more powerful and successful. NASA Mariner and Pioneer missions to our nearest planetary neighbors in the 60s and early 70s reached half a metric ton, NASA Surveyor missions were approximately one metric ton, and the USSR Luna missions were over 5 metric tons by the end of the 70s [2].[1]

At the end of the Space Race, it became more economical to build super satellites and deep space probes such as Cassini/Huygens (5.7 metric tons [2]) and Envisat Earth Observation satellite (8.2 metric tons [3]. In theory, cost reduction would be achieved by including as many scientific instruments as possible with a single space craft bus. However, this approach drove up cost of space science so that only government agencies could feasibly pay for the price tag and compensate for the inevitable development delays [3].

While massive, versatile satellites and probes, such as the James Webb Space Telescope, will always have their place in protracted missions, the last three decades

[1]See appendix A for a chronology of missions and mass from 1957 to 2000.

have seen a new distinct trend in the ubiquity of small satellites. The emergence of low-power nanoelectronics in the 90s greatly influenced the aerospace industry and allowed for more compact scientific instruments and satellites [4] [5]. The small satellites are categorized by mass as shown in table 1.1.

Table 1.1.: Small Satellite Categories by Mass

Prefix	**Mass (kg)**
Mini	100 - 500
Micro	10 - 100
Nano	1 - 10
Pico	0.1 - 1
Femto	< 0.01

As figure 1.1 illustrates, trends have shown that since 2013 small satellites have accounted for more than half of the satellite launches. Small satellites are predominantly used for 5 mission types: technology development, remote sensing, scientific missions, communications, and intelligence. Until 2017, the majority of small satellites launched were technology development missions [6].

Small Satellites occupy an expanding niche market for economic access to space and they have great potential to further revolutionize the way space missions are conducted. Small satellite constellations and formation flight will facilitate better data collection and communication and maneuverable small satellites will allow for cheaper and less risky deep space probes. However, to fully realize this potential, small satellites must make significant advances.

One such enabling technology is propulsion. Propulsion on small satellites, especially nanosatellites, has proven to be a difficult and complicated challenge. Traditional satellite propulsion systems have been more difficult to miniaturize at the same rate as other components and often require more power and volume than smaller plat-

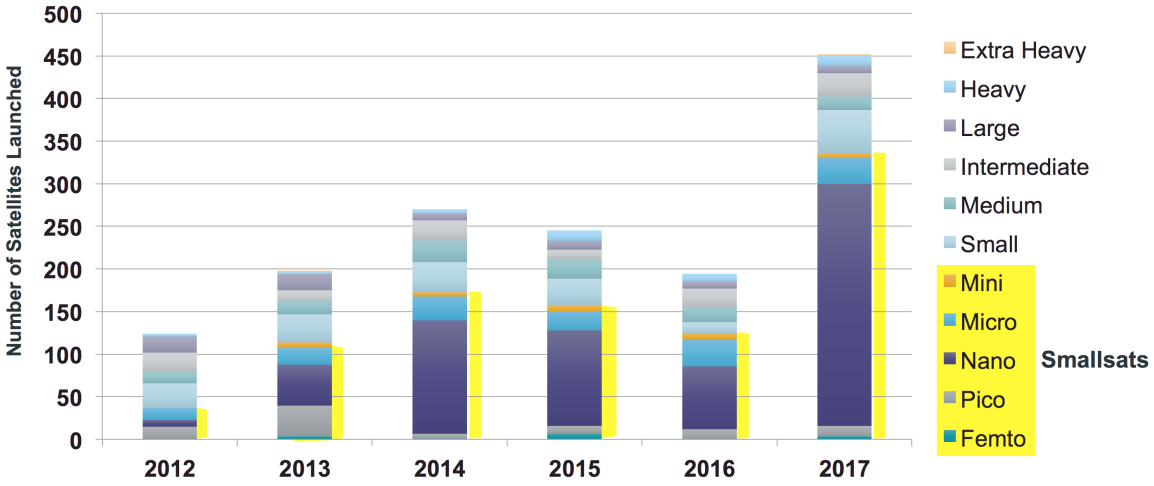

Figure 1.1.: Satellite Launched from 2012-2017 by Type [6].

forms can provide. This is also true of many attitude control systems (ACS), which often require rotating masses to help react to torques applied to a satellite. Small satellite propulsion and attitude control devices are varied in their levels of technology readiness and applications. To this end, the objectives of this thesis are:

- **Conduct a survey of propulsion and ACS technologies for small satellites.** This survey is a catalog of available commercial off the shelf (COTS) systems and systems at various stages of development. Electric, chemical, gold gas, and light sails are considered for propulsion, while reaction wheels, gyroscopes, and torque rods are considered for ACS.

- **Demonstrate controllability of a model small satellite in a vacuum chamber using Film Evaporation microelctromechanical systems (MEMS) tuneable array (FEMTA) micropropulsion.** FEMTA has been demonstrated on a microthrust stand to produce thrust at the microNewton level. This portion of the work was done to verify the system as a viable attitude control system.

- **Perform a tradestudy of micropropulsion and ACS systems for attitude control.** The focus of this tradestudy is to determine the trade offs of different systems and understand which systems should be used in which circumstances.

1.2 Unique Challenges for Small Satellites and CubeSats

The most expensive portion of a satellite or a probe mission is the price of launch. A few of the most successful scientific satellites and probes have also been some of the most massive ever launched. The Hubble Space telescope was 11.4 metric tons [7], roughly the size of a school bus, and Cassini/Huygens, as mentioned before, was 5.7 metric tons [2], roughly the same as an elephant. The more massive the payload, the bigger and more powerful the rocket must be. Small satellites at their most massive are equivalent to a large refrigerator and at their smallest, a softball or a water bottle. The smaller platform drastically reduces the total cost of launch and allows launch ride shares so that multiple payloads are launched at the same time, effectively reducing the launch price for each payload.

The cost reduction allowed the academy to enter the satellite market, using the smaller platform to test new technologies and collect data that otherwise would need to become a secondary or tertiary objective on a larger satellite. This was the impetus that drove scientists, engineers, and professors at Stanford University and California Polytechnical State University to develop the CubeSat Standard in 1999. Following experiences in student-built microsatellites, SAPPHIRE and OPAL, it was clear that not only was there value in student-built satellites, but there was a need for standardization [8]. A CubeSat, as defined in the CubeSat Design Specifications, is a 10cm cube with a mass of up to $1\frac{1}{3}$ kg [9]. A single cube is referred to a unit or a U. This means a 3U CubeSat is an arrangement of three cubes in a row with a combined mass of 4kg. There was also a standardization of a CubeSat Deployment system called

Poly Picosatellite Orbital Deployer (P-Pod) to safely release the CubeSats without damaging other payloads or the launch vehicle [10].

The standardization offered a lower development time and more launch possibilities. The platform was accepted readily into academia as a teaching tool. Not only has it allowed the chance to collect data in space, but it offers a hands-on learning experience in building a satellite that helps students be more marketable to employers [5]. Since 2012, nearly a quarter of Small Satellite launches have been academic with the number of institutions launching CubeSats nearly quadrupling during that time frame. Academia still favors the CubeSat form factor, with 75% of academic small satellites being CubeSats [6]. The majority of Small Satellites launched are in the 4-6kg range, or the 3U size, and this trend is expected to continue in the next 5 years [11].

Academia is not the only body of scientists to imagine the possibilities of the CubeSat format. NASA has readily accepted the advantages offered by CubeSats, and have said that arrays of small CubeSats will be more valuable than a single conventional probe because of system redundancy, system robustness, and distributed measurements. The constellations would allow for arrays of Martian and lunar weather stations, asteroid seismographs, and planetary imaging [12].

CubeSats have also allowed for a boom in technology development and commercial ventures. Companies such as Spire Global, Inc. and Planet Labs would not have been able to emerge in a market that did not have space for small satellites. CubeSats were a disruptive technology, with smaller satellites able to do the same tasks as their larger cousins with more value per kilogram and with quicker development time, allowing investors and customers to see return on their capital in less time [13]. Commercial companies have also capitalized on the need for CubeSat compatible components ranging from satellite buses, to specific control systems, to communication systems.

There is also a tendency for CubeSat designers to gravitate toward COTS subsystems that are not designed for use in a space environment. Conventional hobbyist robotics components are an economic option for many educational CubeSats, espe-

cially during initial testing and design phases [14]. Such COTS devices do need to be considered carefully, as electronics can perform very differently in the harsh thermal and radiation environment of space. Radiation will become an even larger concern as more CubeSats are used for deep space science and exploration and pass through the Van Allen Belts [15].

While small Satellites and CubeSats allowed non-traditional vendors and customers to enter the satellite game, small satellites still have more restrictions than larger satellite platforms. CubeSats are limited in available mass, power, and volume and cannot include as many subsystems as their larger counterparts. Even with the miniaturization of electronics, it can still be difficult to fit all of the necessary systems for a functional satellite and a scientific or commercial payload on board. Many traditional subsystems are forgone on CubeSats, which significantly limits mission capabilities.

One such traditional subsystem is propulsion. Traditional propulsion systems draw large amounts of power and necessary pressurization systems are not space efficient and add significant system complications. Most CubeSats use solar panels to generate their consumable power. CubeSat batteries typically store 50-100 kJ and power systems tend to operate at only 8 Volts and 10-20 Watts [15] while many compact propulsion systems require the upper limit or more power to function.

There is a distinct need for propulsion and attitude control, especially for formation flying [16]. CubeSats are being developed for deep space (such as EQUULEUS [17], APEX [18], and Mars CubeSat One [19] [20]) and low Earth orbit (LEO) (such as RAVAN [21], SASI^2 [22], PicSat [23], RadSat [24], and Dellingr [25]). As micropropulsion is further integrated onto CubeSats, mission capabilities and objectives will expand.

2. SURVEY OF MICROPROPULSION THECHNOLOGIES

2.1 Important Parameter Definitions

Propulsion is, at its most basic, a perfect example of Newton's Second and third Laws of motion,

> The alteration of motion is ever proportional to the motive force impressed; and is made in the direction of the right line in which that force is impressed.
>
> To every action there is always opposed and equal reaction: or the mutual action of two bodies upon each other are always equal, and directed to contrary parts [26].

The second law outlines that a body will move in the direction of and proportionally to a net force. We know this relationship as,

$$F = ma \tag{2.1}$$

where F is the force, m is the mass of the body, and a is the acceleration. Equation 2.1 describes how to change the motion of a satellite. Exerting a force on the satellite will predictably and repeatably affect the motion of the satellite.

The third law explains how a propulsion system is able to accomplish that goal. Propulsion systems rely on a change in momentum from ejecting fuel to produce a force on the spacecraft. Push the exhaust in one direction, and the payload will move in the opposite direction. Connecting the second and third law means that the thrust of the propulsion system is equal and opposite the the time rate of change of the momentum of the propellant. Momentum is mass multiplied by velocity. Thus the

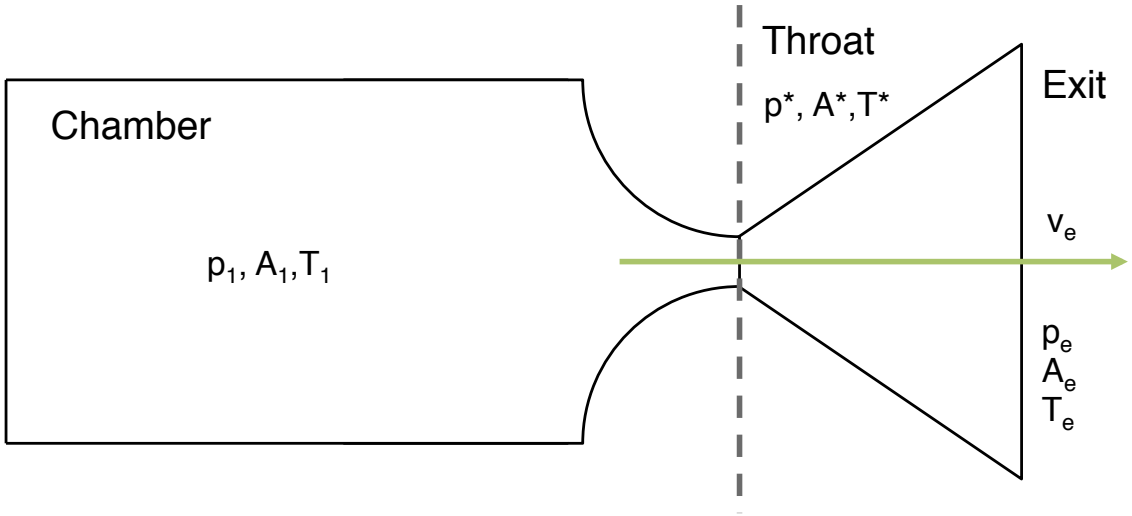

Figure 2.1.: Traditional Rocket Chamber With Values Labeled.

time rate of change of momentum is the exit velocity of the propellant, multiplied by the time rate of change of the mass.

The thrust equation for a traditional rocket propulsion system is given in equation 2.2. Figure 2.1 is a visual representation of the temperature, area, velocity and pressure values in a traditional rocket chamber. This equation includes the pressure change term, due to the the difference in exit and atmospheric conditions.

$$F = \dot{m}V_2 + (p_2 - p_3)A_2 \tag{2.2}$$

F is the thrust produced by the engine, $\dot{m}$ is mass flow rate (a constant in a rocket engine), p designate pressure, A designates area, T designates temperature, and the subscripts 1, t, 2, and 3 are the chamber, throat, exit, and atmospheric values respectively. Equation 2.2 is modifiable for more accurate use in rarefied gas environments, such as low Earth orbit [27].

In electric propulsion systems, such as Hall effect and ion thrusters, the mass flow rate for thrust is the ion mass flow rate, given in equation 2.3, which is a function of ion beam current, I_b, ion mass, M and charge, q. The exhaust velocity of ions is

a function of the net voltage, V_b, ion mass, and charge. The expression for exhaust velocity is given in equation 2.4.

$$\dot{m} = \frac{I_b M}{q} \tag{2.3}$$

$$v_2 = sqrt\frac{2qV_b}{M} \tag{2.4}$$

Multiplying equations 2.3 and 2.4 gives equation 2.5, which relates electric thruster parameters to thrust.

$$T = \dot{m}v_2 = \sqrt{\frac{2MV_b}{q}}I_b \tag{2.5}$$

Other important parameters for thrusters are the total impulse, I, specific impulse, Isp and change in velocity, ΔV. An impulse is a force integrated over a time interval (defined in equation 2.6. An impulse is dimensionally equivalent to momentum. This makes the total impulse an indication of the potential momentum change that the propulsion system can impart. In equation 2.6, the exit velocity v_2 would be the equivalent velocity for a typical rocket propulsion system where the equivalent velocity is the exit velocity plus the difference between the exit and atmospheric pressures multiplied by the exit area and divided my the mass flow rate.

$$I = \int F dt = F\Delta t = mv_2 \tag{2.6}$$

The impulse bit is the smallest impulse or momentum change that a thruster can impart. Typically it is given as the thrust over the shortest time that the thruster can be engaged. The specific impulse, defined in equation 2.7, is the total impulse divided by the weight (mass multiplied by the acceleration due to gravity, g_0) of the propellant. Specific impulse is essentially the ratio of thrust produced to the weight flow of the propellant. Specific impulse is considered to be a propulsion efficiency parameter, as it gives the amount of thrust produced for the amount of mass ejected from the

system. The larger the specific impulse, the more mass efficient the propulsion system is.

$$Isp = \frac{I}{mg_0} = \frac{F}{\dot{m}g_0} \tag{2.7}$$

The change in velocity that a propulsion system imparts is a function of propellant mass m_p, inert mass, m_i, and exit velocity of the ejected propellant. Equation 2.8 is called the ideal rocket equation or the Tsiolkovsky equation.

$$\Delta V = v_e \ln\left(\frac{m_i + m_p}{m_i}\right) \tag{2.8}$$

It is important to note that equation 2.8 can be applied to a single thruster burn, as long as the burn time and original mass of the propellant is known. The propellant mass is equal to the mass flow rate multiplied by the burn time. Each time a burn is executed, the initial mass should include the mass of all propellant that remains after the burn.

2.2 Chemical Propulsion Technologies

It is reasonable that the first propulsion systems on spacecraft would emulate the propulsion systems that are used in launch vehicles. Chemical propulsion technologies include solid propellant, mono-propellant, bi-propellant, and Cold Gas thruster systems. Schematics for these systems are shown in figure 2.2 Chemical propulsion systems capitalize on enthalpy and gaseous expansion to provide thrust, as described in equation 2.2 [28].

Chemical thrusters are able to provide larger amounts of momentum change over short amounts of time compared to their electrical counterparts, but they also come with complex pressure systems and the propellants can be toxic. The specific impulse is limited by secondary endothermic reactions that reduce the exhaust velocity and the dimensional restrictions of the expansion nozzles [29]. Leakage is a primary concern

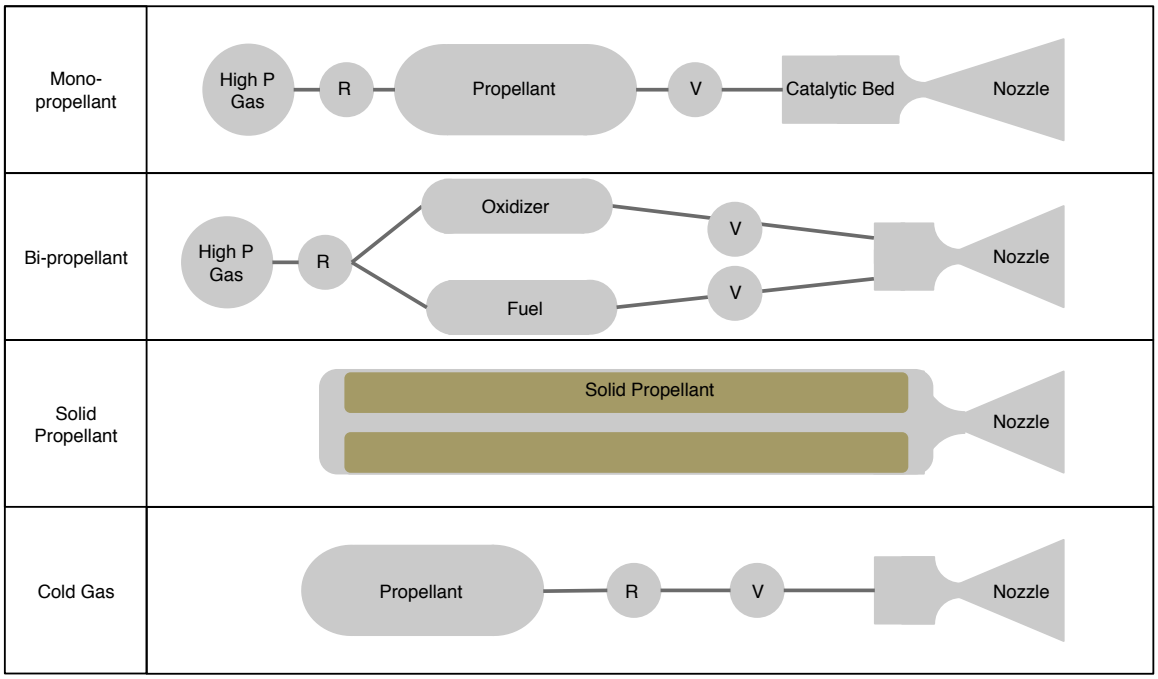

Figure 2.2.: Illustrative Schematics for Chemical Propulsion Systems (modified from [28]).

for chemical propellant systems, as the mission lifetime can be limited by propellant mass, and chemical propellants can be toxic and pose an exposure hazard. [30].

2.2.1 Mono-propellant Thrusters

Mono-propellant thrusters have one liquid on-board propellant that undergoes an exothermic, decomposition reaction as it flows over a high pressure catalytic bed (liquid permanganates, solid manganese dioxide, platinum, or iron oxide). The product gases then expand through a nozzle [28] [31]. Typically the propellant used is hydrazine (N_2H_4), but hydrazine is extremely toxic making it difficult to handle and highly restricted. This is why other propellants, such as Nitrous Oxide (NO_2) and green propellants (discussed more in section 2.2.2), are being considered [32]. Table 2.1 gives a short list of mono-propellant thrusters.

Table 2.1.: Sample of mono-propellant thrusters

Name	Entity	Propellant	Thrust (mN)	Isp (sec)	Power (W)	Source
MPS-120	Aerojet Rocketdyne	Hydrazine	250-280	217	10	[33]
MRE-0.1	Northrop Grumman	Hydrazine	800-1000	216	15	[34]
Nitrous Oxide Thruster	University of Toronto	Nitrous Oxide	100	131	30	[32]
MONARC-1	Moog	Hydrazine	1000	228	18	[35]

2.2.2 Green Propellant Thrusters

Green propellant thrusters are a subset of mono-propellant thrusters that use lower toxicity propellants such as hydroxylammonium nitrate (AF-M315E, NH_3OHNO_3) or ammonium dinitramide (LMP-103S , $NH_4N(NO_2)_2$). AF-M315E has been seen to have a slightly higher specific impulse and a higher density than hydrazine while posing no safety threat to extended environmental exposure. The United States Air Force has rated a leak of AF-M315E as critical whereas a hydrazine leak is considered catastrophic. AF-M315E is difficult to freeze, allowing reduced system complexities and lower power requirements for propellant management and thermal conditioning. [36] [31]. Table 2.2 lists examples of green propellant thrusters in development.

2.2.3 Bi-propellant Thrusters

Bi-propellant systems carry a fuel and an oxidizer which are combusted, and their products exhausted to produce thrust. This is a ubiquitous rocket technology where

Table 2.2.: Sample of Green Propellant Thrusters

Name	Entity	Propellant	Thrust (mN)	Isp (sec)	Power (W)	Source
BGT-X5	Busek	AF-M315E	500	225	20	[37]
ArgoMoon	VACCO	LMP-103S	100		20	[38]
AMAC	Busek	LMP-103S	100-500	220	20	[39]
100 mN HPGP	ECAPS	LMP-103S	30-100	209	8	[40]
500 mN HPGP	ECAPS	LMP-103S	120-500	231	10	[40]

liquid oxygen and and RP-1 ($C_{12}H_{26}$) or liquid nitrogen are common oxidizer fuel pairs, though hypergolics such as mixed oxides of nitrogen (dinitrogen dioxide with nitric oxide) and monomethylhydrazine ($CH_3(NH)NH_2$, a hydrazine based chemical) have been used on micropropulsion systems [41] [31]. These systems tend to provide more thrust specific impulse than their mono-propellant counterparts but tend to be significantly more complex with necessary cryocooling and pressurization handling systems for both oxidizer and fuel. Often helium vessels are required to provide the necessary injection pressure for combustion [28]. These requirements add extra mass and require more volume, making them less desirable for microsatellite missions.

One method of solving the complexity of storing the propellants, is electrolysis. Electrolysis propulsion systems use electricity to decompose water into its constituent oxygen and hydrogen. The combustion of hydrogen and oxygen provides high specific impulse and exit velocities while producing inert water that will not harm any spacecraft payloads. The stored water may also act as a kinetic energy damper to stabilize the spacecrafts rotation [42]. However, this system has its own share of complexity in the decomposition and recombustion of the propellants. Table 2.3 includes a thruster with separated fuel and oxidizer and an electrolysis thruster.

Table 2.3.: Sample of bi-propellant and electrolysis thrusters

Name	Entity	Propellant	Thrust (mN)	Isp (sec)	Power (W)	Source
Hydros-M	Tethers Unlimited	Water	1200	310	10	[43]
DST-12	Moog	MMH/MON	22000	302	9	[41]
5lbf	Moog	MMH/MON	22000	292	15.6	[41]

2.2.4 Solid Propellant Thrusters

Solid propellant thrusters consist of a combustion chamber that encases a solid mixture of oxidizer grains (commonly ammonium perchlorate) bound by a rubber fuel. Solid propellant thrusters are designed to burn at known rates and deliver a specific thrust profile. These systems are very compact as they do not require the intricate feed systems to deliver pressurized propellants [44].

However, solid propellants do not provide throttlable thrust and often are a single burn device, making them less desirable for satellite missions. There have been studies into the MEMS versions of these thrusters, although, solid propellant thrusters currently remain most suited to heavy launch vehicles [31].

2.2.5 Cold Gas Thrusters

A cold gas thruster differs from the other chemical combustion propulsion systems in that they do not require combustion. High pressure gas is expanded through a micronozzle to produce the necessary thrust [45]. Propellants are normally refrigerants or inert gases such as Nitrogen. Butane has also been flown as a cold-gas propellant on Snap-1. The propellant can either be liquid or gaseous when stored, in order to reduce sloshing or propellant volume. Cold gas thrusters are among the

most flight proven propulsion technologies due to their relative simplicity and lower power consumption. [31]. Table 2.4 includes a sample list of cold gas thrusters.

Table 2.4.: Sample of Cold Gas Thrusters

Name	**Entity**	**Propellant**	**Thrust (mN)**	**Isp (sec)**	**Power (W)**	**Source**
Reaction Control	VACCO	R134a	10	40	10	[46]
CNAPS	University of Toronto	Sulfur Hexafluoride	12-50	45		[47]
POPSAT-HIP1	μspace Rapid	Argon	1			[31]
240 mN	Moog	Nitrogen	10-40	60	10	[48]
MEMS Cold Gas	NanoSpace	Nitrogen	0.01-1	50	3	[49]
SNAP 1	SSTL	Butane	50	43		[31]

The thrust produced is directly related to the stored pressure of the propellant and is affected by the heat of the system. As propellant is expended, the plenum pressure will decrease, resulting in a decrease in the maximum thrust provided by the system and solar heating could cause a variance in the performance of a thruster [31].

Cold gas thrusters do not add energy by combusting propellant. This decreases the specific impulse and thrust compared to other chemical systems. However, the lack of chemical reaction allows for a much simpler thruster design and can allow for more compact systems [31].

When first modeling the cold gas systems, researchers were investigating whether to use quasi-two dimensional modeling or full three dimensional modeling, and found that a quasi-two dimensional model was sufficient if not more accurate [50]. It was

later confirmed that in low reynolds number flows (Re $<$ 1000) the larger viscous effects essentially truncated the nozzles. In lower reynolds, where the pressure thrust in equation 2.2 is negligible and an expansion nozzle unecessary, an orifice is sufficient [51] [27]. The elimination of a nozzle is a significant reduction in mass and volume required for a propulsion system.

2.3 Electric Propulsion Technologies

As shown in equation 2.5, electric propulsion generates thrust by exhausting electrically charged ions. The spacecraft power is used to generate these ions from a propellant. The ejection speed is directly related to the voltage applied to thruster, which imposes less thrust and specific impulse limitations compared to chemical systems [28]. Electric propulsion systems are very power demanding and most flight proven electric propulsion hardware used on deep space missions exceed the available power on small and microsatellites as well as exceeding the restricted mass and volume [52]. Many systems are in development to address these issues.

Table 2.5 includes examples of Resistojet, gridded ion, and hall thrusters. Table 2.6 lists examples of electrospray, pulsed plasma thrusters, and helicon thrusters.

2.3.1 Resistojet & Arcjet Thrusters

Resistojets are electrically enhanced cold gas thrusters, which improves their specific impulse. The working fluid passes over an electrical heating element, which allows the exhaust to be accelerated to supersonic speeds through the nozzle. This is often accomplished through inducing phase change in the propellant through vaporization [44] [53]. Figure 2.3 includes a schematic for resistrojets.

In a similar way, arcjet thrusters are electrically augmented monopropellant thrusters. An electric arc discharge is used to heat the combustion products and amplify the work obtained from the gaseous expansion of the exhaust. The combustion products pass through an annulus where the arc discharge is created between a central cathode

and the coaxial anode [53] [30]. While this does not impede mass flow rate, it does constrict the effective cross sectional area by ionizing the gasses, allowing much higher exit velocities and increased specific impulse [28].

2.3.2 Gridded Ion Engines

Gridded ion engines ionize a neutral gas with radio frequency (RF) or direct current (DC) discharge to create a weakly ionized plasma. This plasma is then passed through high voltage grids to extract the positive ions to create an positive ion beam

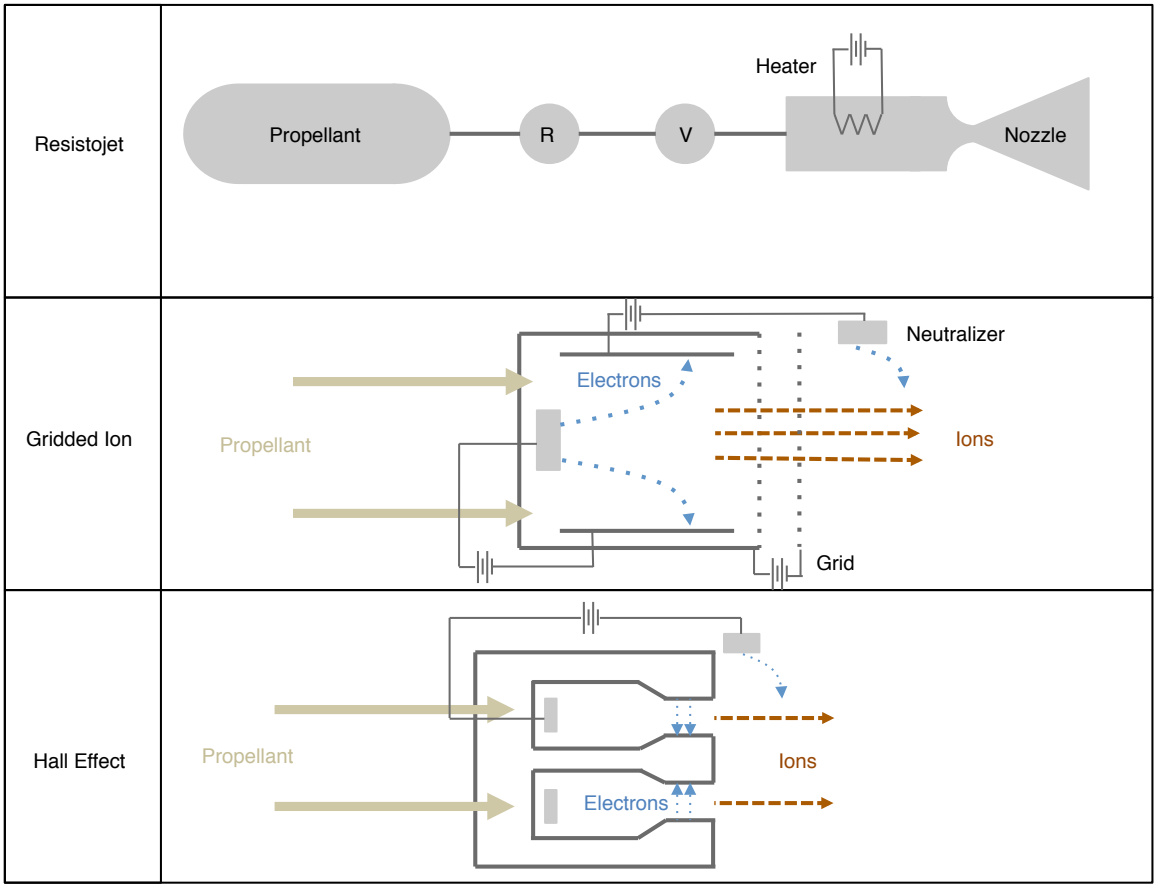

Figure 2.3.: Illustrative schematics for electrical propulsion systems, I (modified from [28])

which is used to generate thrust. This beam is neutralized with the electrons collected in the creation of the beam in order to avoid spacecraft charging [54] [28]. These systems have extremely high specific impulse due to increased exit velocity. A diagram of a gridded ion engine is provided in figure 2.3.

Miniaturization of ion thrusters has been impeded by physical limits. Decreasing the ionization chamber dimensions can lead to the mean free path of ionizing electrons to become larger than the chamber which can quell the production of ions without a burdensome, powerful magnetic field [30].

2.3.3 Hall Effect Thrusters

The Hall effect thruster exploits a the Hall effect using high voltage biasing and a magnetic field to produce thrust. Electrons are generated inside a hollow cathode which are then sent through a magnetic field before reaching the anode upstream. The magnetic field traps the electrons, which then form Hall currents. This current ionizes a neutral propellant and those ions are then accelerated by the large potential difference between the anode and cathode [30]. Figure 2.3 provides a schematic for Hall effect thrusters.

Hall thrusters, like gridded ion engines, are a heritage space propulsion technology that has been used for decades. Hall thrusters tend to have higher thrust densities than gridded ion engines but lower specific impulse [54]. There is also less risk of spacecraft charging with a Hall thruster due because there are no gridded electrodes [28].

2.3.4 Electrospray Thrusters

Electrospray thrusters can be separated into two categories based on ion production method: Colloid and field emission electric propulsion (FEEP). Like Gridded Ion Engines, Colloid thrusters use two high voltage electrodes to accelerate propellant particles ionized by a Taylor cone to generate thrust. When liquid metal, such

Table 2.5.: Sample of Electric Propulsion Technologies I

Name	Type	Entity	Prop.	Thrust (mN)	Isp (sec)	Power (W)	Source
μarcjet	Arcjet	Univ. Washington	Argon	1.1-1.8	90	5	[55]
AQUARIUS	Resist-ojet	Univ. Tokyo	Water	4	70	20	[17]
MiXl	Ion	Cal. Tech	Xenon	0.22	3200	28.1	[56] [57]
BHT-200	Hall	Busek	Xenon	13	1375	20	[58]

Table 2.6.: Sample of Electric Propulsion Technologies II

Name	Type	Entity	Prop.	Thrust (mN)	Isp (sec)	Power (W)	Source
BET-100	Electro-spray	Busek	Ionic Liquid	0.005-0.100	1800	15	[59]
MEP	Electro-spray	JPL	Indium	0.2	3744	8.16	[45]
IFM Nano	FEEP	Enpulsion	Indium	0.01-0.50	5000	40	[60]
μ-PPT	PPT	Dawgstar	Teflon	0.02	500	12.5	[45]
RFT	RF	Phase Four	Xenon	1-15	1000	100	[61]

as indium, or a ionic liquid in a capillary interacts with the large electrical potential the liquid interface forms a cone which emits ionized particles that are accelerated in a method similar to a gridded ion thruster [44].

In FEEP engines, liquid metal propellant passes through an electric field generated by the positively charged propellant capillary and the outer cathode. The electric field

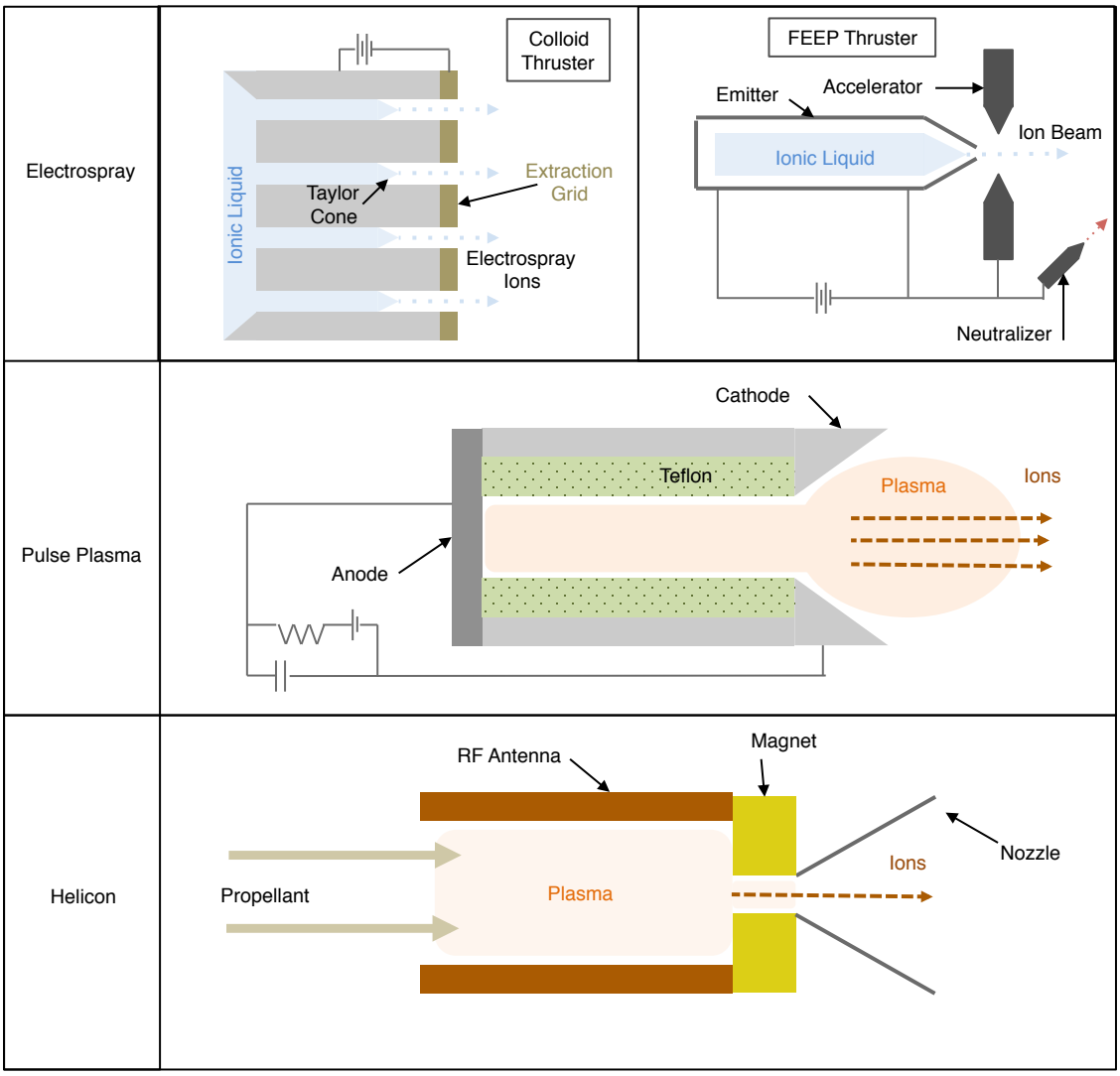

Figure 2.4.: Illustrative Schematics for Electrical Propulsion Systems, II (modified from [28] [30].)

creates a Taylor cone at the tip of the capillary, which generates ions. The electric field accelerates the ions [30]. Figure 2.4 presents both schematics for electrospray thrusters.

Electrosprays can be small and offer milliNewton increments of thrust with very high specific impulse and low power compared to other electrical systems. Unlike

plasma discharge propulsion technology, ionizing neutral particles does not diminish the power efficiency of generating the electrospray. The system also generates very little heat, which is a thermal benefit of small satellites [62]. FEEP thrusters do require neutralization to prevent spacecraft charging.

2.3.5 Pulsed Plasma Thrusters

Pulsed Plasma Thrusters (PPT) generate their plasma by ablating and ionizing solid propellant, such as Teflon (polytetrafluoroethylene). A high-current discharge across the propellant surface sublimates the propellant. The ionized propellant is then accelerated using an electromagnetic field [63] [30]. A sample diagram for a PPT is shown in figure 2.4.

The first PPT was flown on the Russian spacecraft Zond 2 in 1964, and the technology has matured though experimental and flight demonstration since. PPT are advantageous for small satellites as they have small impulse bits with high specific impulse but do require more power for the larger impulse bit [64] [65]. The plasma produced is also quasi-neutral, removing the need for a separate neutralizing component [66].

2.3.6 Helicon Thrusters

Helicon Thrusters, like gridded ion thrusters, have gaseous propellant. The propellant is ionized by an electromagnetic field around an RF antenna which creates a helicon wave in the plasma. The low frequency helicon wave is a more efficient method of plasma generation than cold plasma generation due to its higher electron density [30] [67]. Most commonly, a magnetic nozzle is used to accelerate the ions as this generates more thrust and minimizes losses. The Helicon thruster typically have more thrust than gridded ion or electrospray thrusters as they create more plasma, but they are less efficient at acceleration, which weakens their specific impulse. [45]. An example helicon thruster is shown in figure 2.4.

3. SURVEY OF SMALL SATELLITE ATTITUDE CONTROL SYSTEMS

Dynamic stability was a major challenge for the first spacecraft, as many early spacecraft would spin out of control without passive spin stabilization induced by the physical shape and weight distribution of the satellite. In the 1970s dual-spin spacecraft began to exploit a spinning rotor to further stabilize spacecraft rotation [68]. Momentum control systems (MCS) on satellites have been predominantly operating this way for decades. These systems include two major components: the stator (stationary) and the rotor (spinning). By changing the speed of the rotor, the MCS is able to change its stored angular momentum.

Angular momentum, $\bar{H}$, is directly proportional to the moment of inertia, $\mathbf{I}$, and the angular velocity, $\bar{\omega}$.

$$\bar{H} = \mathbf{I} \times \bar{\omega} \tag{3.1}$$

The moment of inertia is analogous to mass for linear momentum. It is a tensor quantity and depends on the mass distribution and spin axis of a body. The moment of inertia is the infinite sum of the all the point mass moments in the body integrated over the entire mass.

$$\mathbf{I} = \int_0^M \bar{r}^2 dm \tag{3.2}$$

Newtons second law applied to rotating systems gives the relationship for a torque, $\bar{\tau}$. A torque is the rotational equivalent to a force in a linear system and is equal to the time rate of change of angular momentum. The moment of inertia is generally assumed constant in the CMS, but the rotation rate can be changed.

Table 3.1.: MCS Systems Comparison (Modified from [68])

Actuator	**Typical Application**	**Level of Agility**	**Precession (Deg)**
Spin stabilization	Low-precision, magnetospheric science	N/A	0.1-1 in 2 axes
Gravity-gradient boom	Coarse Earth observation, technology demonstration	N/A	5-20 in 2 axes
Magnetic torquers	Momentum Dumping, nanosats in LEO	Low agility	1-10 in 2 axes
Momentum wheels	Astronomy, communications	N/A	0.001-1 in 3 axes
Reaction wheels	Astronomy, communications	Medium agility	0.001-1 in 3 axes
Control-moment gyroscopes	Earth imaging and radar, satellite servicing, asteroid grappling	High agility	0.001-1 in 3 axes

$$\bar{\tau} = \frac{\partial \bar{H}}{\partial t} = \frac{\partial}{\partial t}\left(\mathbf{I}\bar{w}\right) = \mathbf{I}\frac{\partial \bar{w}}{\partial t} \tag{3.3}$$

Spacecraft attitude and orientation is determined by the torques induced by the environment. One of these environmental torques is due to the aerodynamic drag in low earth orbit. An MCS could provide a reaction torque in order to counteract the external torque to ensure the spacecraft remains stable. If the spacecraft needed to turn or point in a different direction, the CMS could provide a torque to change the attitude of the spacecraft.

There are several methods for MCS, and these are outlined in table 3.1. Spin Stabilization is the simplest, manipulating the geometry and mass distribution of the

Table 3.2.: Sample of Commercially Available Reaction Wheels

Name	**Company**	**Momentum (Nms)**	**Max Torque (Nm)**	**Power (W)**	**Mass (kg)**	**Source**
MicroWheel	Blue Canyon	0.015	0.004	5.5	0.13	[69]
HR10	Honeywell	12	0.15	135	5.36	[70]
RW-0.003	Sinclair	0.005	0.001		0.05	[71]

satellite to stabilize the satellite in orbit. Gravity-gradient boom uses the known gravitational field and the mass distribution to keep the satellite in a desired orientation. These are both passive stabilization methods as they require no power. Magnetic torquers use electromagnetic rods that interact with the Earth's magnetic field to stabilize the spacecraft [68].

Momentum wheels, reaction wheels, and control-moment gyroscopes (CMG) are all active stabilization methods. These methods are of the most interest for attitude control as they can change the orientation of the spacecraft. Of these three, reaction wheels and control-moment gyroscopes will be the focus of the this technology survey[1].

3.1 Reaction Wheel

Reaction wheels are fixed to the spacecraft structure such that they have one degree of freedom. The spin motor changes the rotation rate of the rotor, which in turn reacts on the spacecraft with a torque. Reaction wheels require significant amounts of power, as shaft power (provided by the motor) is equal to the rotational velocity multiplied by the torque [68]

[1]Momentum wheels and reaction wheels operate with the same basic mechanisms, however momentum wheels store momentum intended for passive stabilization, while reaction wheels do not. Reaction wheels are frequently used on zero-momentum spacecraft that use other passive techniques [68]. Reaction wheels are, commercially, the most readily available of the two

Reaction wheels only operate in one axis; momentum is changed by changing the rotational velocity of the rotor. In this case, the vector magnitude is the quantity changed. The torque is limited by how fast the reaction wheel can spin. Smaller reaction wheels tend to have larger spin rates as they are used for applying less torque [68]. Figure 3.1(a) gives a schematic for a reaction wheel and table 3.2 includes a sample list of reaction wheels. Appendix D includes the full survey of commercially available reaction wheels.

Reaction wheels are generally smaller than CMGs as they do not need to gimbal, but in order to have control of every axes, three reaction wheels are required.

3.2 Control Moment Gyroscope

In a CMG, the rotor is not fixed to the spacecraft as it is in a reaction wheel. Instead of changing the magnitude of the angular momentum, a CMG changes the direction of the angular momentum. The Spin rate remains constant while the rotor is able to gimbal or tilt [68]. There are two varieties of CMGs: double-gimbal and single-gimbal.

The dynamics of a CMG allow for a slightly different definition of torque. If the rotation rate is not changing, equation 3.3 must be modified. In this case the time rate of change in momentum is due to the change in angle, θ, that the angular momentum vector passes through. Figure 3.2 depicts this change as the rotor gimbals. If the change in the angle θ with time, Ω is known, then equation 3.3 can be changed to equation 3.4

In appendix E includes a table listing the specifications for commercially available CMGs.

$$\bar{\tau} = \frac{\partial \bar{H}}{\partial t} = \frac{\partial \theta}{\partial t} \times \bar{H} = \bar{\Omega} \times \bar{H} \tag{3.4}$$

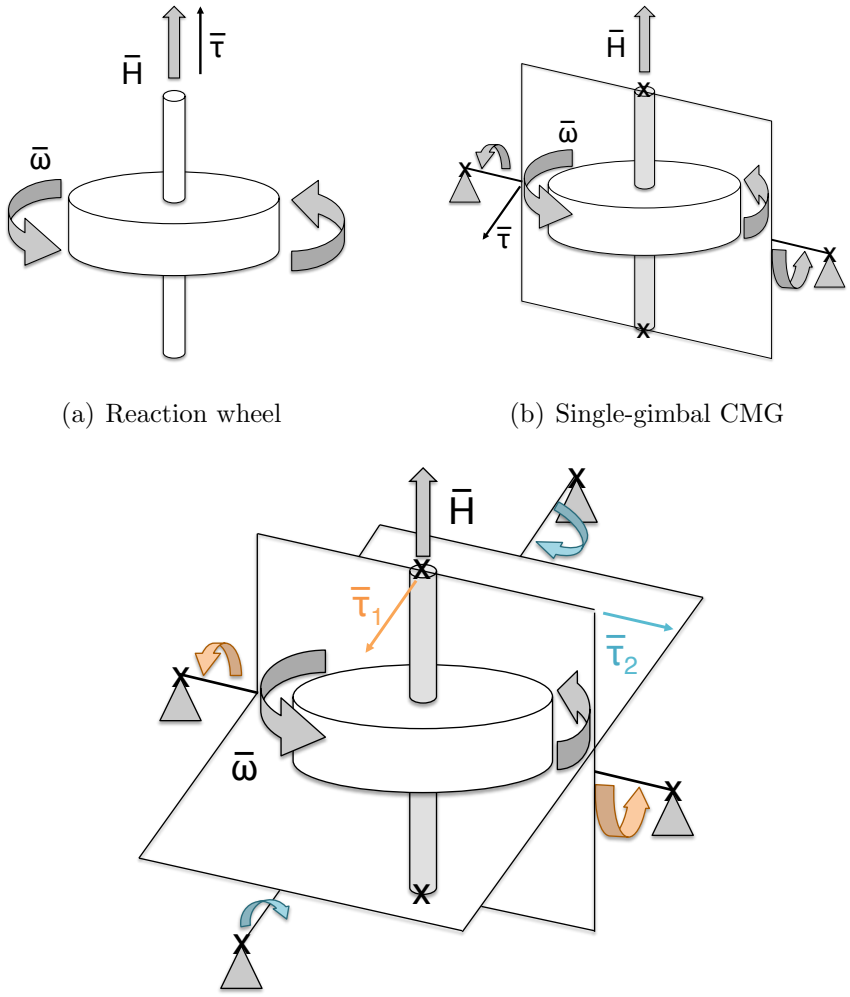

(a) Reaction wheel

(b) Single-gimbal CMG

(c) Double-gimbal CMG

Figure 3.1.: Operating Schematics for MCS (modified from [68])

3.2.1 Double-Gimbal Control Moment Gyroscope

This design allows the rotor to act as a free gyroscope. Figure 3.1(c) shows how the CMG is connected to two frames that allows it to be gimbaled in the two non-rotating axes in the spacecraft body frame. As shown in figure 3.1(c), tilting the CMG in reference to either of the other two axes changes the direction of the resultant torque.

Compared to the reaction wheel, the CMG has more degrees of freedom, and since the motor does not need to change the rotational speed of the rotor, the torque is not limited to the power available [68].

3.2.2 Single-Gimbal Control Moment Gyroscope

The single-gimbal CMG, as shown in figure 3.1(b), is a double-gimbal CMG without the outer gimballing mechanism. This constrains the torque generated to the plane perpendicular to the plane being gimballed through angleθ.

Single-gimbal CMGs are the most power efficient MCS devices as they can provide large output torques for less power [68], but they also tend to take up sinificant room as they do need to be able to rotate in a volume within the spacecraft.

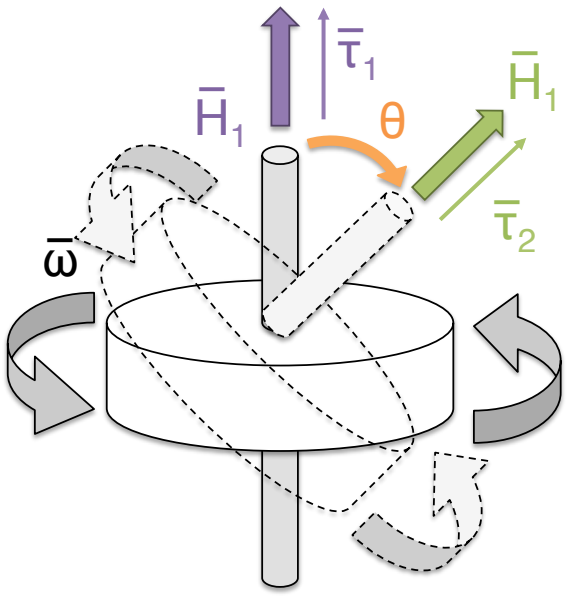

Figure 3.2.: Demonstration of a change in angular momentum without a change in spin rate. The solid and dashed objects are both at rest after having completed a slew through the angle θ.

4. FILM EVAPORATION MEMS TUNABLE ARRAY

As discussed in chapter 2, there are many electric and plasma based, and electrically enhanced chemical propulsion systems in use and being investigated. Another electrically augmented propulsion system is the Film-Evaporation MEMS Tunable Array (FEMTA) thruster, shown in figure 4.1. FEMTA has been developed since 2013 and is currently on the fourth generation of the nozzle. This chapter is primarily concerned with investigations into the performance of this generation of nozzles.

In previous investigations, FEMTA has been reported to have a mass flow rate of 80 micrograms per second, a thrust range of 6-68 microNewtons, and a linear thrust to power ration of 230 microNewtons per Watt [72].

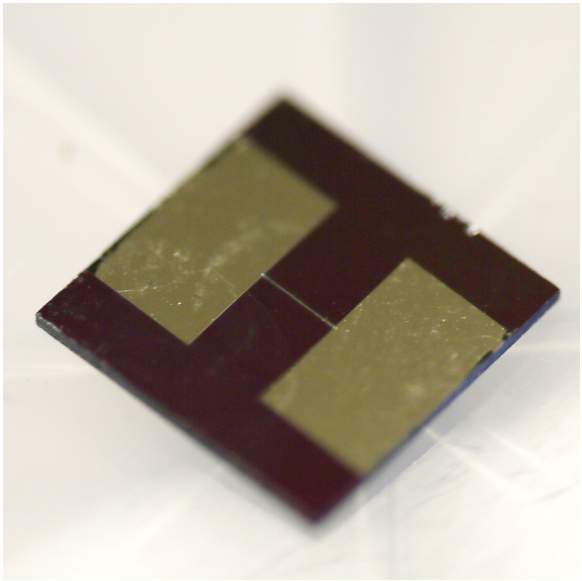

Figure 4.1.: Third generation FEMTA nozzle as seen from the inlet side

4.1 Underlying Physical Principals

FEMTA is thermal valve that manipulates the capillary action of water. This fluid phenomenon allows a liquid in a narrow tube to flow regardless of external forces, specifically gravity. Capillary action allows pipettes to draw liquid from a bulk fluid, siphons to transfer liquids from one container to another, and allows absorbent materials to wick and absorb. This effect is due to intermolecular forces at the solid-liquid interface within the capillary.

Liquids are incompressible and take the shape of their container. However, when a liquid is in free fall with no container, its surface tension and pressure will cause the water to take a spherical shape, which minimizes the surface area. This is also observed in a capillary, with the surface of the liquid forming a meniscus. Molecules in the liquid are attracted to one another by van der Waals forces, without which there would be no liquid phase of matter. The molecules at the interface of the liquid with a gas are not surrounded by other molecules, and thus these molecules exert a stronger cohesive force on their neighbors than those in the bulk fluid creating a boundary that is under tension due to that force. This amplification of the intermolecular forces is referred to as surface tension and is illustrated in figure 4.2. Surface tension can be considered the energy required to transport molecules from the bulk liquid and form a new surface area [73]. In water, hydrogen bonding[1] increases the surface tension.

The Young-Laplace equation, equation 4.1 is based on a the qualitative theory of Thomas Young and mathematically derived by Pierre-Simon Laplace. It relates the pressure difference, ΔP, across flexible boundary interface to the curvature of that interface. The pressure difference is proportional the the curvature, with the constant of proportionality the surface tension, γ, of the boundary.

$$\Delta P = \gamma \left(\frac{1}{R_1} + \frac{1}{R_2} \right) \tag{4.1}$$

[1] A hydrogen bond is formed when a hydrogen atom is bound to an atom that is more electronegative than hydrogen. Hydrogen bonds can be formed between molecules, and are slightly stronger than Van der Waals forces.

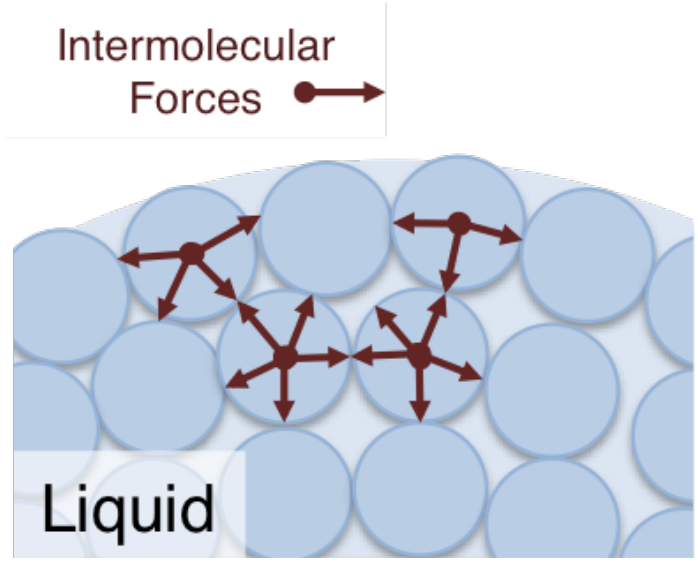

Figure 4.2.: Illustrative description of intermolecular forces. The forces at the surface are stronger because the outer molecules are not surrounded by other molecules.

R_1 and R_2 are the principal radii of curvature. Figure 4.3 depicts how these radii of curvature are defined. For a soap bubble, R_1 is equal to R_2 and is the radius of the sphere. For a cylinder that is much longer than it is wide, R_1 is the radius of the cylinder and R_2 is infinity [73]. For capillaries, equation 4.1 becomes

$$\Delta P = \gamma \left(\frac{1}{R} \right) \tag{4.2}$$

The principal of this relationship can be demonstrated with a simple example, shown in figure 4.4. Assume a thin film, such as a rubber membrane of a balloon, is placed under light tension across the opening of a cylindrical pipe that is closed at the other end so that it is flush to the opening and creates a seal between the pipe and the outer environment. In this condition, the pressure is the same both inside the pipe and the outer environment. If a vacuum pump partially evacuates the pipe, the pressure inside the pipe is lower than the atmospheric pressure and the membrane will be concave. If the pump raises the pressure of the pipe until it is greater than the atmospheric pressure, the membrane will become convex.

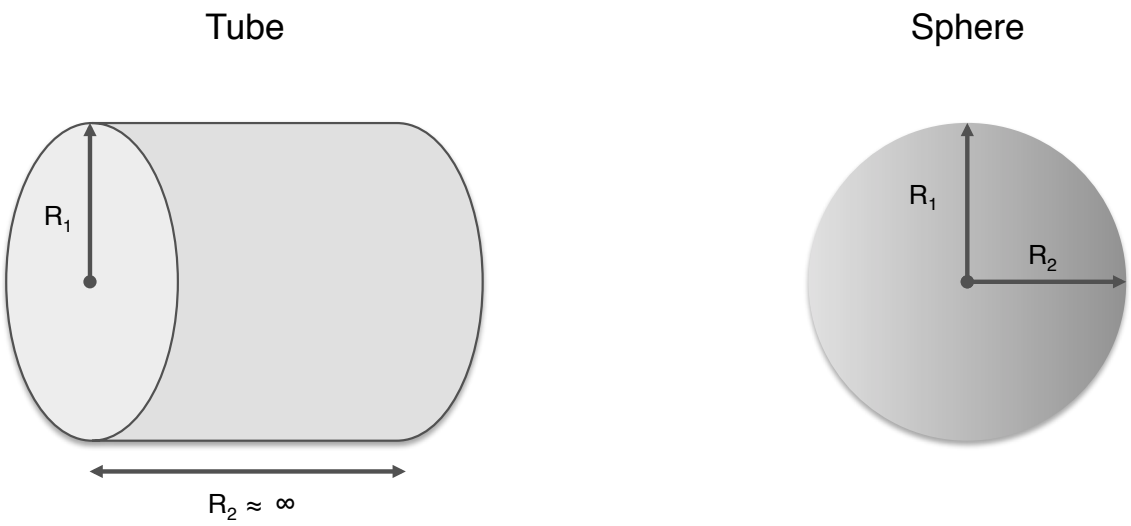

Figure 4.3.: Radii defined for Young-Laplace equation for a tube and sphere (modified from [73])

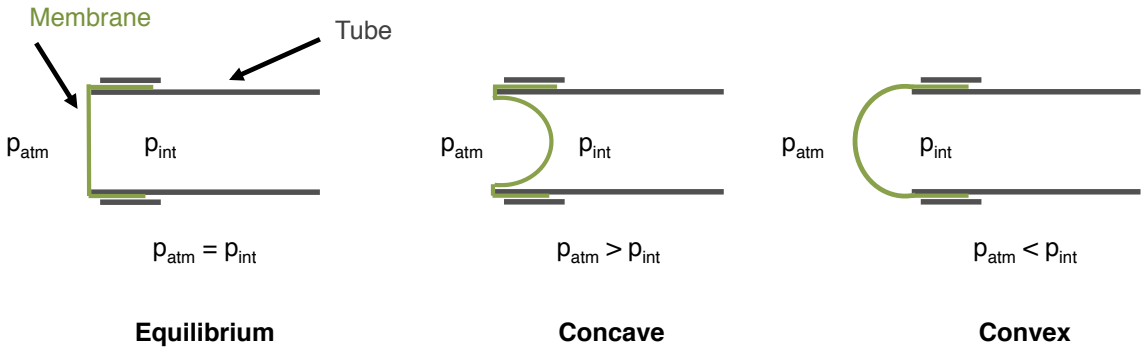

Figure 4.4.: Illustrative example of pressure differential relationship to boundary curvature; when the pressure is balanced, there is no curvature to the boundary, when the atmospheric pressure is greater, the boundary curves inward, and when the atmospheric pressure is less, the boundary curves outward (modified from [73]).

The thermal valving effect relies on holding the surface tension forces in equilibrium with the normal stresses in equilibrium. The capillary action opposes the

evaporation of the liquid when exposed to a vacuum. Balancing these forces results in a relationship where the gap diameter or width is dependent on vapor pressure of the liquid, p_{vap}, the contact angle, α, and the surface tension.

$$D = \frac{2\gamma \cos \alpha}{p_{vap}} \tag{4.3}$$

The vapor pressure is highly dependent on temperature. For a set gap size, raising the temperature of the meniscus would upset the equilibrium and initiate vacuum boiling [74]. The relationship for vapor pressure and temperature and gap size and temperature is given in figure 4.5.

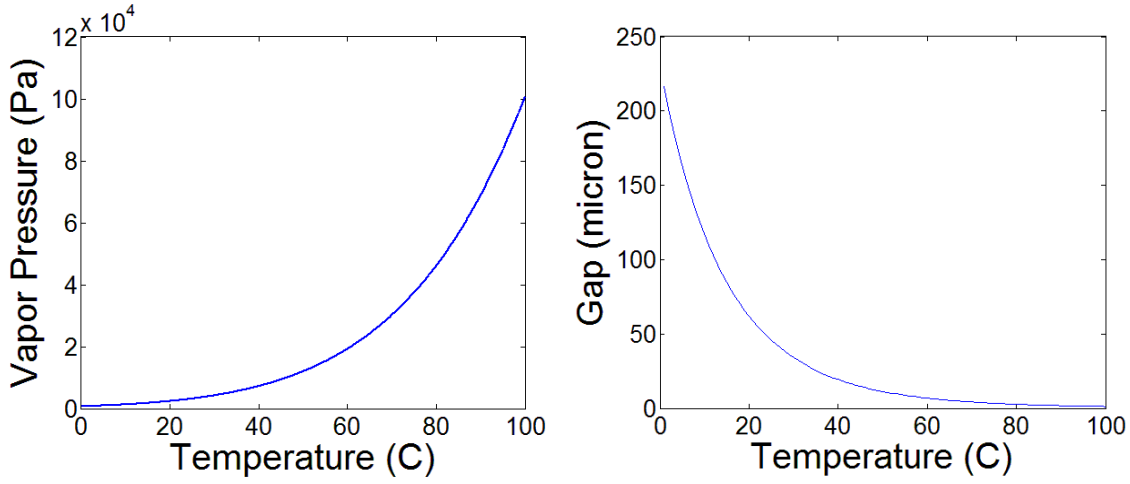

Figure 4.5.: Vapor pressure is directly and exponentially related to temperature while gap size is indirectly and exponential related to temperature. FEMTA is set to operate above 50C [74]).

FEMTA uses a nominal gap size of 10 microns, so that vacuum boiling can commence when the meniscus is heated to 50C. The evaporation of the water is directed through a nozzle to produce thrust. As will be discussed later in section 4.2, the temperature of the resistive heater is controlled by voltage. As more voltage is applied, the forces become more unbalanced, and more thrust is produced.

4.2 Thruster Design and fabrication

The fourth generation FEMTA Nozzles are fabricated in the Scifres Nanofabrication Laboratory clean room using standard microfabrication procedures. The nozzles are produced from a 300 micron thick, 100 millimeter diameter, <1 0 0> oriented silicon wafer. Standard photolithography, wet etching, deep reactive ion etching, and vapor deposition procedures are used.

The fourth generation nozzles have a 40 micron wide inlet that leads to a 10 micron wide throat. The inlet is wet etched with tetramethylammonium hydroxide which results in the sloped surface as silicon with a <1 0 0> crystalline structure etches at a 54.74 degree angle. A thin layer of platinum is deposited onto this slope as the heater. The throat is open to the exit cavity which is 1 millimeter wide. This exit cavity is not included for expansion of the gas, but does serve as a reference feature for fabrication and assists in controlling the throat length. After fabrication, the wafers are diced to create the one centimeter square nozzle.

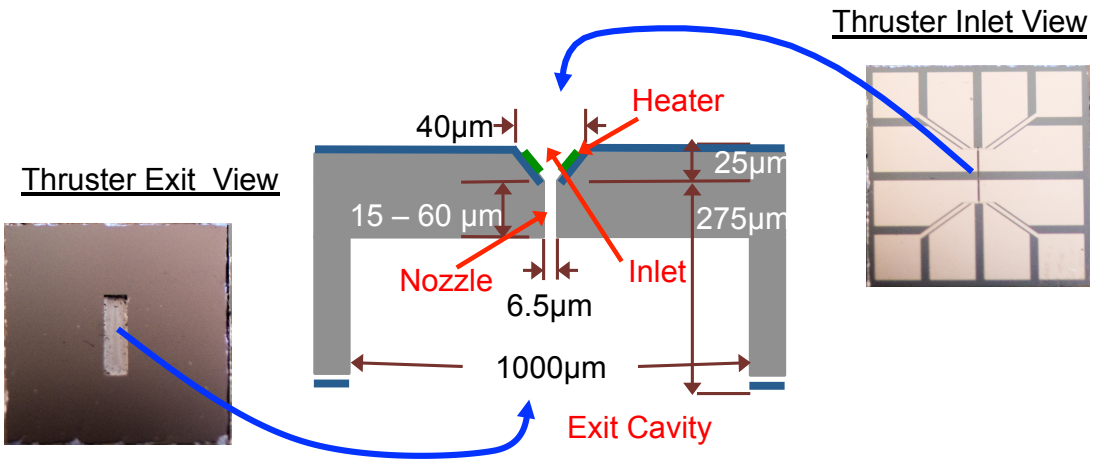

Figure 4.6.: Dimensions for fourth generation FEMTA nozzle.

Tests in previous generations have shown that throat aspect ratios[2] have been crucial to thrust production, with an aspect ratio of 4-6 being ideal for thrust production [74] [72]. Fourth generation nozzles differ from the extensively tested third generation nozzles in the silicon wafer thickness. Third Generation nozzles were fabricated from 500 micron thick wafers. Figure 4.6 shows a diagram of FEMTA dimensions.

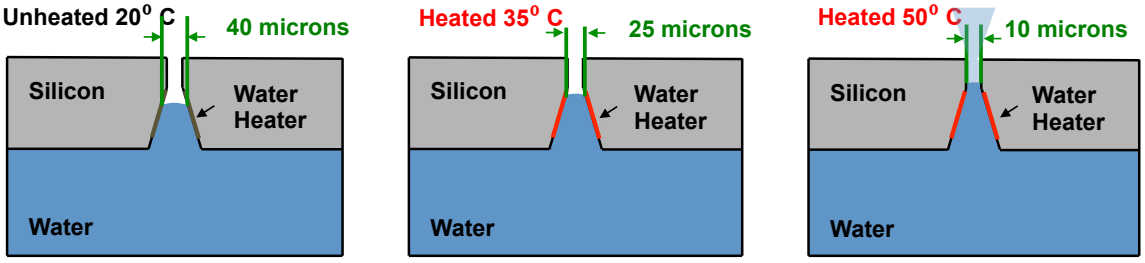

Figure 4.7.: Dimensions for fourth generation FEMTA nozzle.

As can be seen in figure 4.7, the meniscus sits inside of the inlet. When the heaters are activated, the vapor pressure rises and evaporation begins. The platinum heaters are resistive heaters. They are electrically connected to platinum contacts on the inlet side of the nozzle. The power converted to thermal energy from electric energy is equal to the voltage squared over the resistance of the heating element, in this case the platinum. Platinum is chosen, because it does not corrode when in contact with the ultra-pure deionized water.

$$P = \frac{V^2}{R} \tag{4.4}$$

FEMTA uses ultrapure deionized water as a propellant. Mineral ions, such as sodium, calcium, copper, or iron cations, and chloride or sulfate anions, are removed to form deionized water. Ultrapure water also has all organics, inorganic, volatile compounds, and dissolved gases removed. Ultrapure deionized water has a lower

[2]The aspect ratio of the throat is the width divided by the depth.

electrical conductivity than standard water, which is advantageous for using a resistive heater.

4.3 FEMTA Performance Parameters

Due to size constraints within the testing apparatus and quiescent evaporation[3], it is not possible to directly measure the mass flow rate. The mass flow rate can be approximated using ideal isentropic conditions. The following equations assume that the ejected fluid is vapor only [74], W, to the product of specific heat, c_p, the change in temperature, ΔT and the heat of vaporization, h_v.

$$\dot{m} = \frac{W}{c_p \Delta T + h_v} = 0.445\text{mg/s} \tag{4.5}$$

The nozzle is sonic[4], thus it is assumed that the exhaust velocity is Mach 1. Specific impulse is then a function of specific gas constant, R, ratio of specific heats, γ, temperature and the acceleration due to gravity, g.

$$Isp = \sqrt{\frac{2RT\,(\gamma+1)}{\gamma}}\frac{1}{g} = 73.7\text{s} \tag{4.6}$$

These are both approximate and idealized. These values give an approximate thrust of 329 microNewton for 1 Watt of power. In previous work, FEMTA has produced 230 microNewtons per Watt [74].

4.4 1U CubeSat Model Attitude Control Experiment

After successful testing of the third generation FEMTA nozzles yielded reliable and repeatable thrust [72], an experiment was designed to demonstrate single-axis control of a 1U CubeSat model in a vacuum chamber. This would provide valuable performance data and prove the viability of the technology as an attitude control

[3]The valve does not operate perfectly as, even in a micro-channel, there is still a small amount of evaporation from the meniscus. This is described in more detail in chapter 7.

[4]A sonic nozzle ends at the throat and does not include an expansion nozzle.

system. There have been two iterations of this experiment. The hardware for both iterations is discussed below.

4.4.1 First Iteration Experiment Hardware

The first iteration was developed during the January of 2017 with testing beginning in May 2017. Figure 4.8 is a labeled picture of the first iteration with all fabricated and electrical hardware integrated.

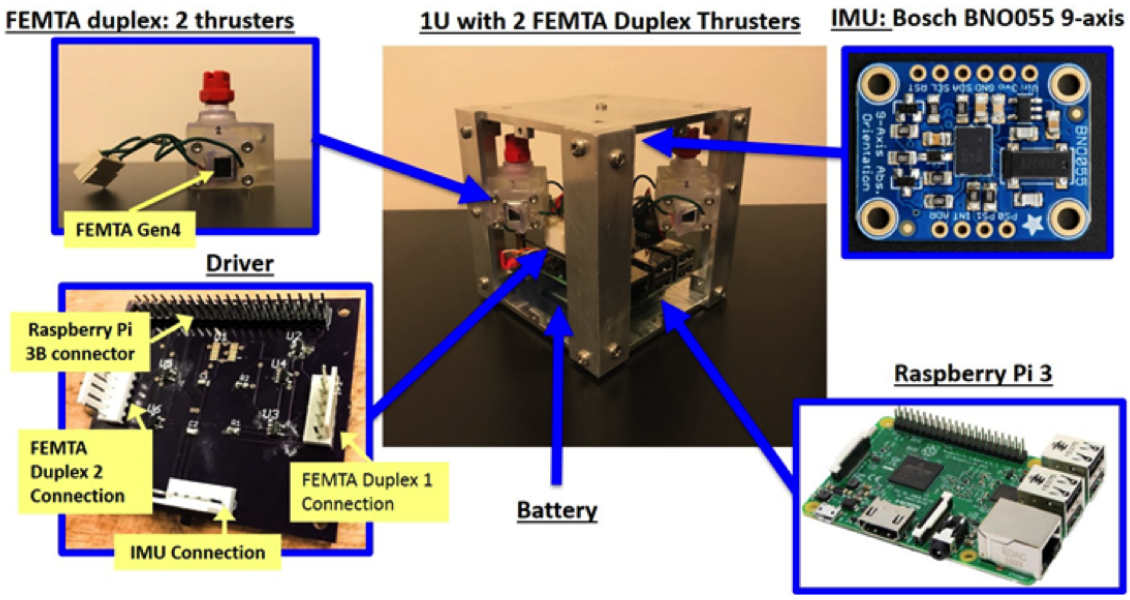

Figure 4.8.: First iteration fully assembled CubeSat

1U-Quad Thruster FEMTA CubeSat Model Frame

The frame consisted of two aluminum plates connected to four aluminum side rails. Electronics were mounted to the top and bottom plates and the duplex thrust cells were mounted to the side rails. Each plate has a tab in each corner to allow the rails and plates to be held together with machine screws.

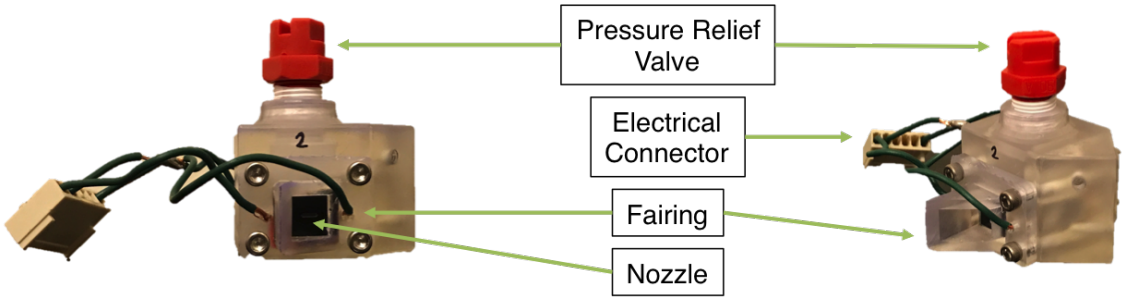

Figure 4.9.: First iteration FEMTA duplex thrust cell

FEMTA Duplex

The FEMTA duplex thrust cells were designed to hold two opposing nozzles to allow two directions of thrust and act as a propellant tank. There were two FEMTA duplex thrust cells installed on the 1U CubeSat model for a total of four FEMTA nozzles. The FEMTA duplex thrust cells mounted to the side rails and connected to the electrical power conditioning board. A first iteration FEMTA duplex thrust cell is shown and labeled in figure 4.9.

A FEMTA nozzle was loaded onto the electrical contact pins underneath the fairing. The fairing was included to prevent any of the spray from interfering with the open electronics and to show a possible way to have the thrust cell flush with the CubeSat model frame. The FEMTAs were sealed with Neoprene and Viton gaskets. The gaskets provided a watertight seal around the thruster. The Neoprene gasket sealed the plenum while the viton gasket sealed the nozzle. Figure 4.10 depicts the electrical contact, gasket, and nozzle alignment.

The thrust cell required a regulated pressure to ensure a proper vapor pressure. A 2 psid pressure relief valve was included at the fill port to provide pressure regulation. The FEMTA duplex thrust cells contained approximately 3.5 grams. The thrust cells were fabricated with a sterolighography resin printer.

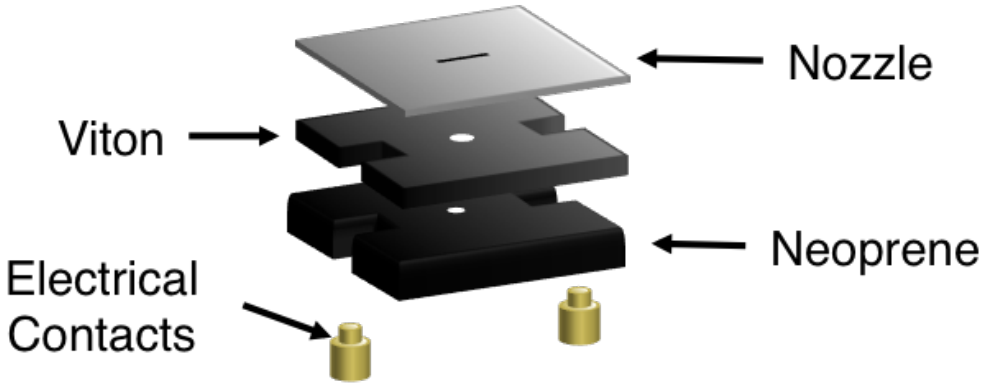

Figure 4.10.: Gasket configuration for first iteration FEMTA duplex thrust cell (modified from [75])

Angular Position Sensor

In order to properly assess the functionality of FEMTA as a control system, an angular position sensor was necessary. An inertial measurement unit (IMU) was chosen over laser or camera optical systems for simplicity, accuracy, and resolution. The IMU would also provide real time feedback and be mounted on the model.

The first iteration sensor was the Bosch BNO055 9-axis Absolute Orientation Sensor. This sensor included an accelerometer, a gyroscope, and a magnetometer for each access. It also includes a temperature sensor to monitor the local device temperature. This typical application for the BNO055 is amateur robotics. The BNO055 is shown in figure 4.8.

The BNO055 has on board calibration and data fusion algorithms that result in accurate position data with minimal steady state error and drift with data acquisition rate of 10kHz.

The IMU was secured to the top plate of the frame with a 3D printed mount. This mount was positioned in the center of the top plate so as to keep the sensor as close to the centerline of the CubeSat model as possible to avoid extraneous orientation and reference frame calculations.

Electronics Network

The electronics network for the satellite includes three computers: an on board computer, a receiving computer, and a data acquisition computer. A diagram of the network is shown in figure 4.11 The on board computer was a Raspberry Pi 3B (designated the CubeSat Pi). Raspberry Pis was chosen due to size constraints, a familiarity with the system, and cost effectiveness for experimentation. Raspberry Pis are neither space rated nor optimized for satellite bus operations.

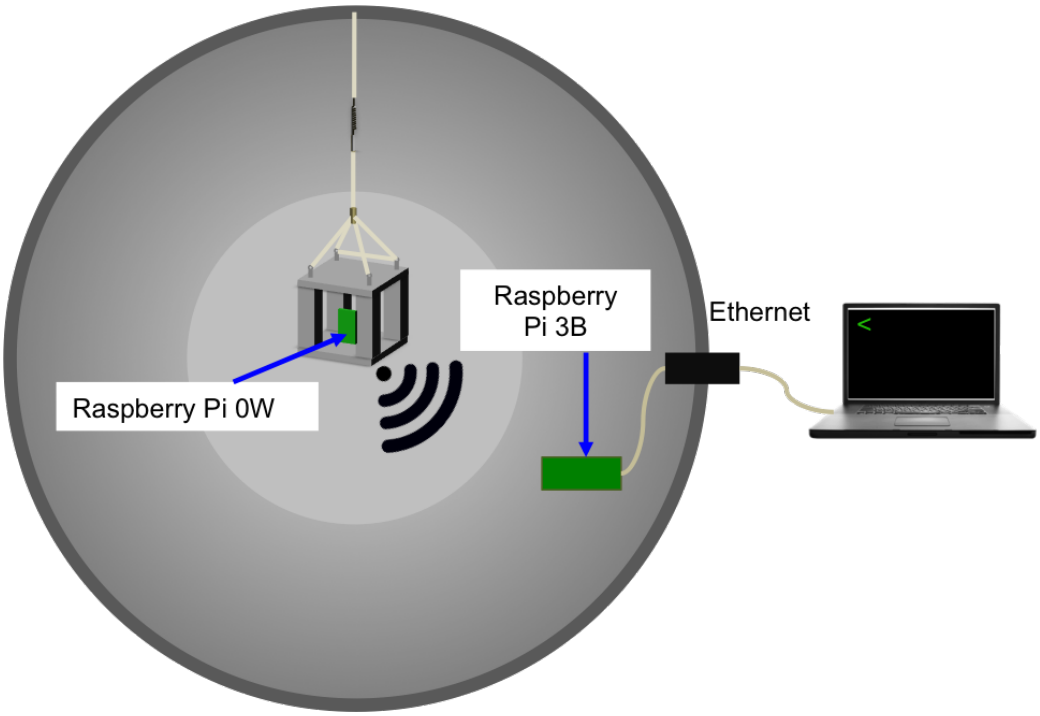

Figure 4.11.: Gasket configuration for first iteration FEMTA duplex thrust cell (modified from [75])

A second Raspberry Pi (designated the chamber Pi) communicated with the CubeSat Pi via an ad-hoc Wi-Fi network. In order for the model to replicate the rotational motion of a nanosatellite in a torque free environment, the communication system was wireless. The structure of the vacuum chamber acts as a Faraday cage, blocking any electrical signals, such as Wi-Fi in the laboratory, in or out of the chamber. The ad

hoc network allows data to be transfered from the CubeSat model to the computer and the user outside of the chamber.

A Linux computer outside of the chamber receives the data from the chamber Pi through an Ethernet connection that runs into the vacuum chamber through a data port. The user would send a command to the satellite to turn on a thruster from this computer.

Printed Circuit Board

The printed circuit board (PCB) powers all components on the satellite. The Raspberry Pi has 3.3 volts digital outputs while FEMTA required a variable signal up to 5 volts. The Circuit board is mounted to the header pins of the raspberry Pi, which relays electrical information to a digital-to-analog connector (DAC) through an I^2C bus. To reduce output impedance to the FEMTAs, the DAC outputs connected to a current driver. The FEMTA nozzles were connected to the board and to a separate voltage pin on the Raspberry Pi. Figure 4.12 illustrates the functional schematic of the PCB, and figure 4.8 includes a picture of the PCB.

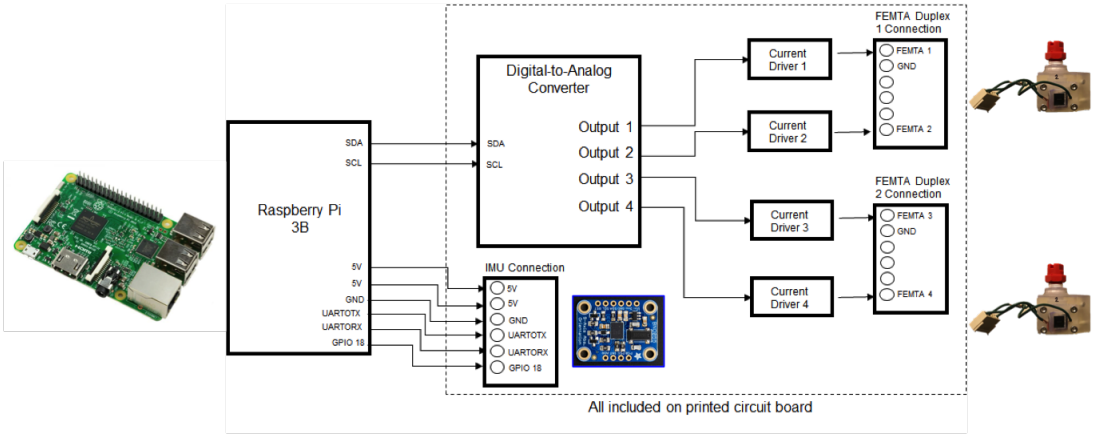

Figure 4.12.: First iteration PCB board schematic

A 2500 mAh, 5V rechargeable battery powered the system. The battery was secured to the bottom plate with a 3D printed mount. The Raspberry Pi was secured to the corner feet of the bottom plate and the PCB was attached to the top of the Raspberry Pi as shown in 4.8.

Hardware Malfunctions

Many lessons were learned while using this hardware setup[5]. While the thrust cells did perform, they had many unexpected technical difficulties. First the resin is an acrylic which is soluble in acetone. Acetone is a cleaner used to remove particulate and certain volatiles from a surface. The acrylic was only able to be cleaned with isopropyl alcohol and water. All thrust cell components were thoroughly cleaned before each experiment[6].

The resin must be exposed to ultra violet light to cure, however due to the shape of the thrust cell, it was difficult to ensure the entire inner cavity of the thrust cell was cured. There were many experiments that showed little to no thruster response, and when the FEMTA nozzles were inspected under a microscope, acrylic, which shows up as a bright white under the dark-view filter, was clogging the nozzles. An example of this clogging is visible in figure 4.13 Very fine pieces of acrylic were shedding into the nozzles causing clogs.

Another issue with the thrust cells was the loading procedure for the FEMTA nozzles. The spring loaded contacts were centered along the throat of the FEMTA. If the fairing was secured too tightly, the pressure points easily snapped the FEMTA along the mid-line with the throat. The gaskets also shedded fibers during the initial tests, with there being evidence of fibrous material in the nozzle. The FEMTAs were difficult to install as they had to balance on the wide set contact pins, and the gaskets were required to be centered so as to not block the nozzle.

[5]Numerical results will be shared in section 4.4.3.

[6]A full description of experiment setup is included in appendix F

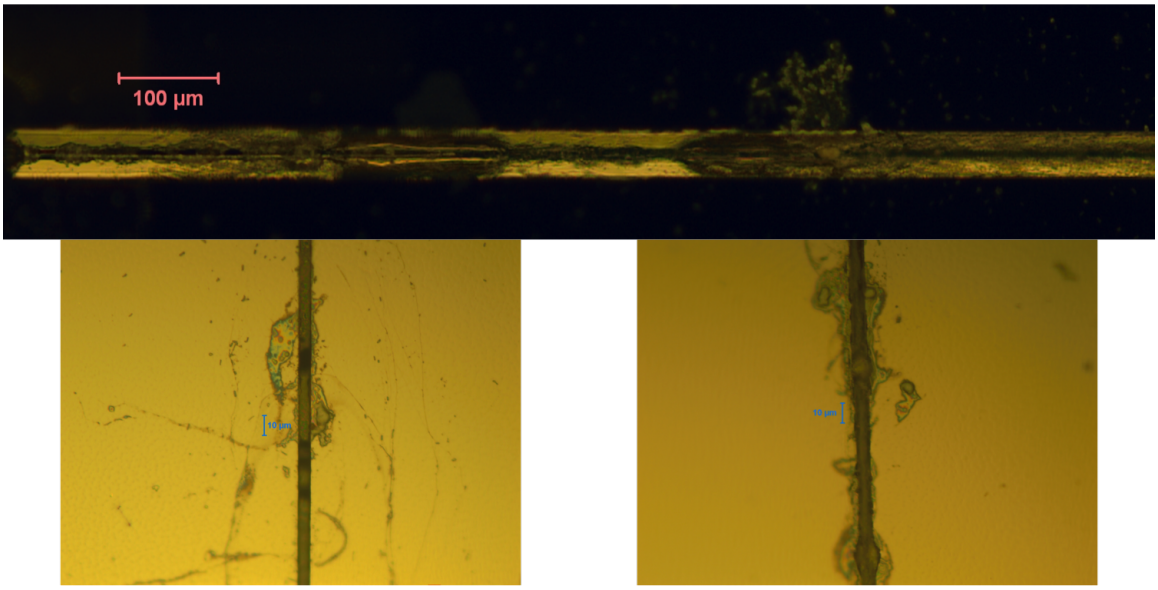

Figure 4.13.: Nozzle clogging during first iteration testing

The final issue with the thrust cell was the pressure relief valve. The valve was unreliable, causing many major leaks and failed tests after several uses.

The PCB issues were primarily in the overheating and failure of the surface mount current drivers. This issue was mitigated mid testing by using larger current drivers with more surface area to radiatively cool.

The Raspberry Pi 3B was thermally tested in the smaller low vacuum chamber before being used in the large high vacuum chamber. While the Raspberry Pi 3B performed within limits in the small vacuum chamber (10-100 milliTorr range), it neared its upper thermal limit in the large vacuum chamber (1-100 microTorr range)[7]. This caused the CubeSat Pi and the chamber Pi to lose connection via the ad-hoc Wi-Fi network.

This issue was mitigated during testing by adding a mounted aluminum heat sink in contact with the central processing unit (CPU) to the chamber Pi and a mounted copper heat sink in contact with the CPU to the CubeSat Pi. These heat

[7]Lab equipment is described in detail in appendix G

sinks transferred the heat from the CPU by conduction and had more surface area to radiate the heat into the chamber.

The IMU also experienced a failure. The BNO055 is not rated for or designed for use in a high vacuum environment. The accelerometers and gyroscopes, which worked in the small vacuum chamber did not collect data in the large Vacuum chamber. The magnetometers did still function[8].

4.4.2 Second Iteration Hardware

The second iteration 1U CubeSat model hardware was developed during Fall 2017 and Spring 2018. The problems from the first iteration were addressed. Revisions, discussed below, were made to the FEMTA duplex thrust cells, the on board computer, the PCB, batteries, and the IMU.

1U FEMTA Duplex Thrust Cells

The second iteration experiment Thrust Cells were machined from polyether ether ketone (PEEK) plastic. PEEK is a synthetic Polymer that has low out-gassing properties and sufficient thermal properties for use in high vacuum experiments. While the first iteration FEMTA Duplex Thrust Cells were 3D printed, the second iteration designed required machining on a CNC mill. The Duplex was separated into a bottom tank and a top plate as show in figure 4.14. These two pieces were sealed together with a Viton seal and secured by Nylon machine screws. The second iteration FEMTA duplex thrust cells hold approximately four grams of water.

The Neoprene and Viton gaskets were replaced with a soft-O-ring seal. A pocket was created to seat the FEMTA. The electrical contact pins were also moved to mitigate the cracking issue. The pins were placed at opposite corners of the FEMTA nozzle rather than along the nozzle slit. Instead of using wires to connect directly to the pins, tin-coated copper rods were manufactured to hold the contact in place. The

[8]A more in depth discussion of IMU analysis is given in appendix **??**.

Figure 4.14.: First iteration FEMTA duplex thrust cell compared to the second iteration

wires were then soldered to these rods, simplifying the loading procedure. The new seals and electrical contact scheme is shown in figure 4.15.

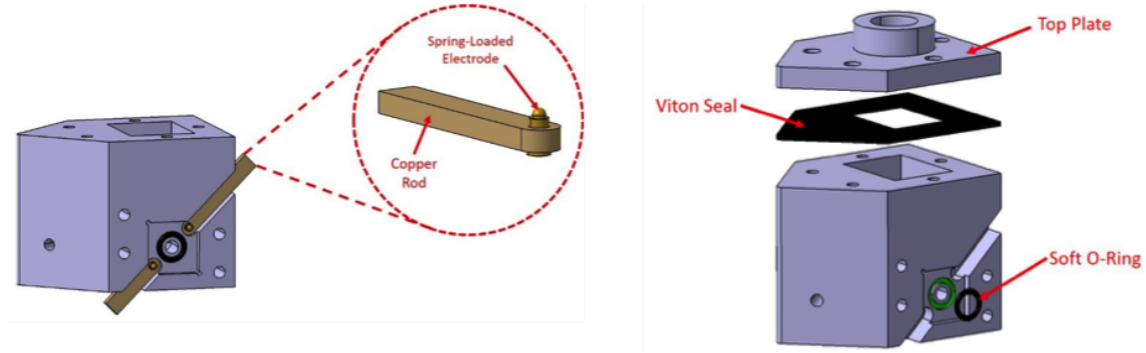

Figure 4.15.: Computer graphic showing the sealing and contact mechanisms in the second iteration FEMTA duplex thrust cells

The pressure relief valve on each FEMTA duplex thrust cell was replaced by a single, shared solenoid valve. The valve connects the two thrust cells by plastic plumbing. The solenoid valve is open during initial pump down and is closed by

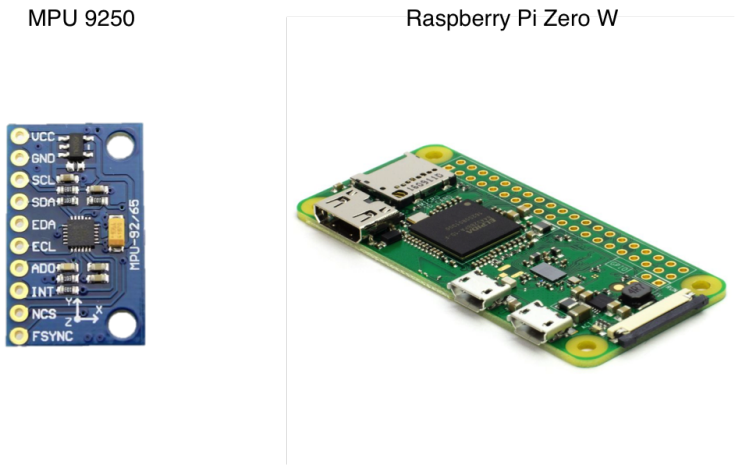

Figure 4.16.: Electronics included on the second iteration 1U CubeSat model

the user when the pressure gauges show the large vacuum chamber has reached the desired pressure for the thrust cell plenum.

Angular Position Sensor

With the failure of the accelerometers and gyroscopes on the BNO055, a new IMU was selected. The InvenSense MPU-9250 was chosen as the replacement. The MPU-9250 also has an accelerometer, gyroscope, and magnetometer on all three axes, and a temperature sensor. The BNO055 was still installed on the CubeSat model for redundancy, as the magnetometer is known to function. Both sensors shared the top plate mount used in the first iteration. The MPU-9250 is pictured in the figure 4.16

On board Raspberry Pi

The on board Raspberry Pi was changed for the second iteration. A Raspberry Pi Zero W, shown in figure 4.16 replaced the Raspberry Pi 3B. The Raspberry Pi Zero W has the same communication capabilities as the Raspberry Pi 3B but the Raspberry Pi Zero W is smaller and has a smaller footprint inside of the CubeSat model.

Printed Circuit Board

.

A major change was made to allow a greater voltage range to the FEMTA and increase time available for tests as battery life was extended. Two nine Volt batteries were added to replace the previously used five volt battery. The operational amplifiers added to the board increase the current to the FEMTA thrusters and can be set by changing the gain across the operational amplifier. This is accomplished by adding different resistors to the PCB. The PCB was primarily altered to accommodate more connections (two batteries and a second sensor). The schematic for the second iteration PCB is shown in figure 4.17.

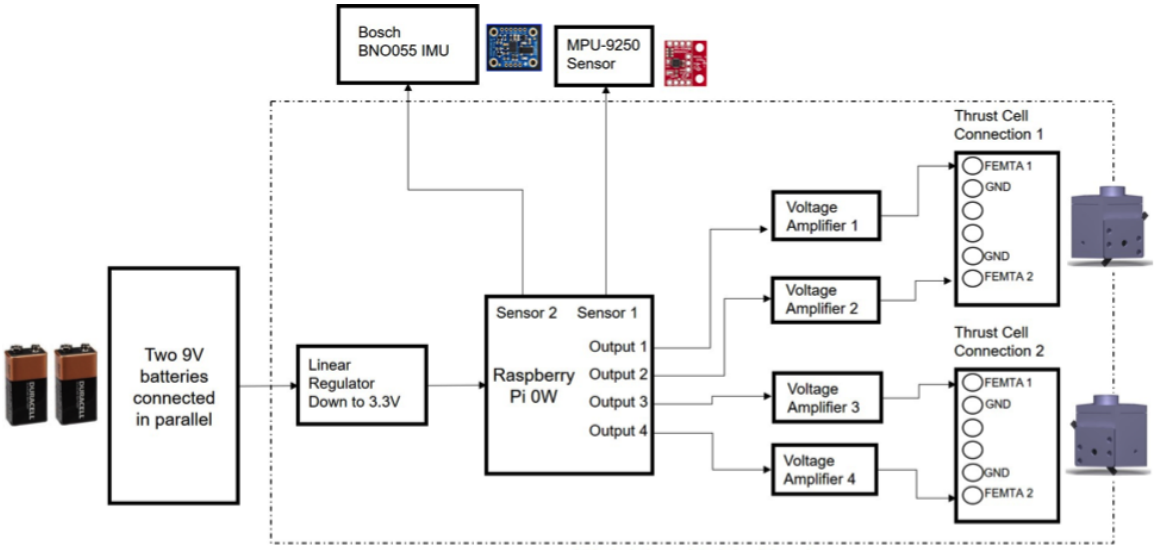

Figure 4.17.: Second iteration PCB schematic

4.4.3 First Iteration Experiment Results

The four FEMTA nozzles were labeled A through D, so that A and C would initiate counterclockwise rotation, and B and D would both initiate a clockwise rotation, as

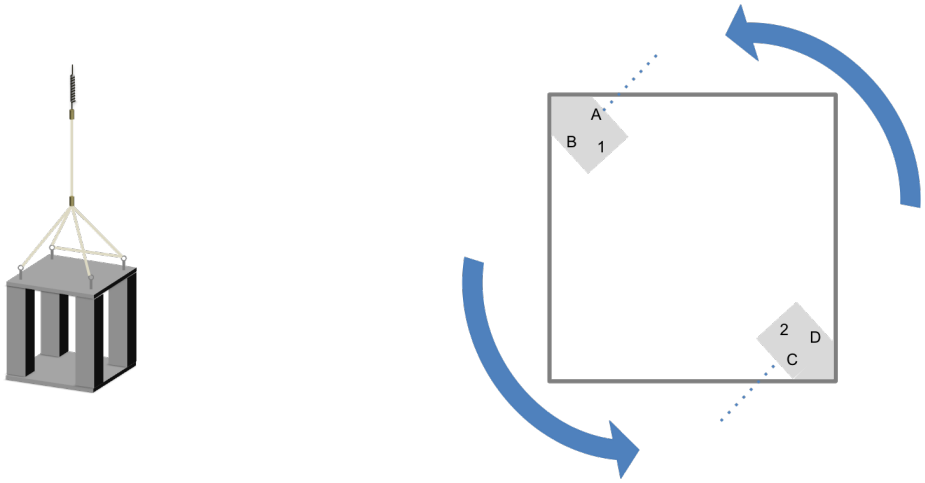

Figure 4.18.: Second iteration PCB schematic

shown in figure 4.18. Thrusters A and B were on duplex thruster 1 and thruster C and D were on duplex thruster 2.

Table 4.1 includes the measured parameters for a sample test. Table 4.2 includes the resulting test data. During this test, Thruster B and D were most effective. Thruster C did not respond. The CubeSat model was left to settle between each test. Thruster firing is determined qualitatively by monitoring the Vacuum chamber pressure. The Vacuum chamber pressure, while not recorded during the test, was approximately 30 microTorr, and the introduction of water vapor to the system is indicated by a significant increase (up to one order of magnitude larger) of pressure in the vacuum chamber. It is also important to note that the mass difference between the start and end of the test is not indicative of the mass expended during firing. While the vacuum pumps evacuate the vacuum chamber, some water is lost due to a change in vapor pressure. The nozzles also generate a small (approximately 1 microNewton) quiescent thrust when not activated.

These tests were filmed to provide qualitative data of the test. Figure 4.19 shows frames from the video of the 7th test in table 4.2. The time stamp in the frames is given to the 30th of a second. Rotation of the CubeSat Model commenced at 45

Table 4.1.: First iteration FEMTA duplex thruster parameters [75]

Thrust Cell	**1**	**2**
FEMTA Device Resistance Direction	A : 73Ω Counterclockwise	C : 71Ω Counterclockwise
	B : 72wΩ Clockwise	D : 68wΩ Clockwise
Dry Mass	33.0 g	32.8 g
Pre-Test Wet Mass	36.8 g	36.8g
Post-Test Wet Mass	34.3 g	34.7 g
Total Water	3.8 g	4.0 g
Total Water Expended	2.5 g	2.1 g

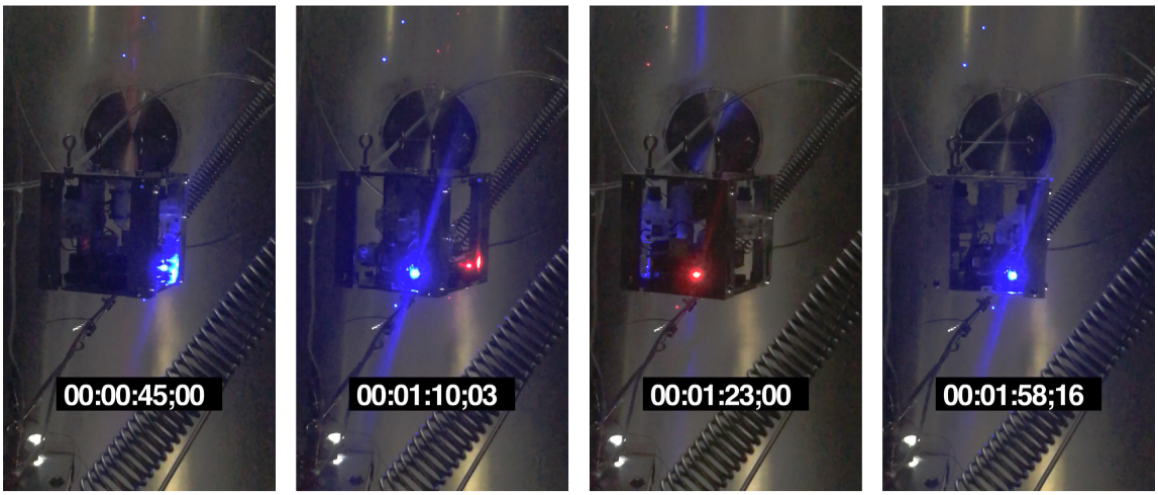

Figure 4.19.: Stills from first iteration experiment test 7. Time stamps are measured to the 30th of a second. Each frame is a quarter of a revolution (modified from [75])

seconds and an entire rotation was completed in 1 minute and 13 seconds. During the test the pressure increased to above 100 microTorr.

Table 4.2.: Test description

Test	FEMTA	Rotation	Pressure Increase
1	C	N/A	No
2	A	N/A	No
3	D	Clockwise	Yes
4	B	Clockwise	Yes
5	C	N/A	No
6	A	Counterclockwise	Yes
7	D	Clockwise	Yes

The data from the magnetometer was analyzed to produce angular position data. The magnetometer acts as an electric compass, measuring the strength of the electrical field it passes through. By setting the maximum field strength as 0 and comparing and combining the measured data, the angle that the CubeSat model has moved through can be determined. Figure 4.20 shows the angle and derived angular velocity data for the whole test. Figure 4.20 shows the angle, angular velocity, and force during the acceleration period of the test. As can be seen from the angular velocity and force plots, the derived data is not smooth, which is expected from measured data. A gyroscope is necessary for better angular velocity data.

The data shows that a maximum angular velocity of approximately 7 degrees per second was reached over 34 seconds.

4.4.4 Second Iteration Experiment Results

Thrust Testing

The first task for the second iteration experiments was to perform thrust tests with the nozzles to be used during the experiment in the second iteration FEMTA duplex thrust cells.

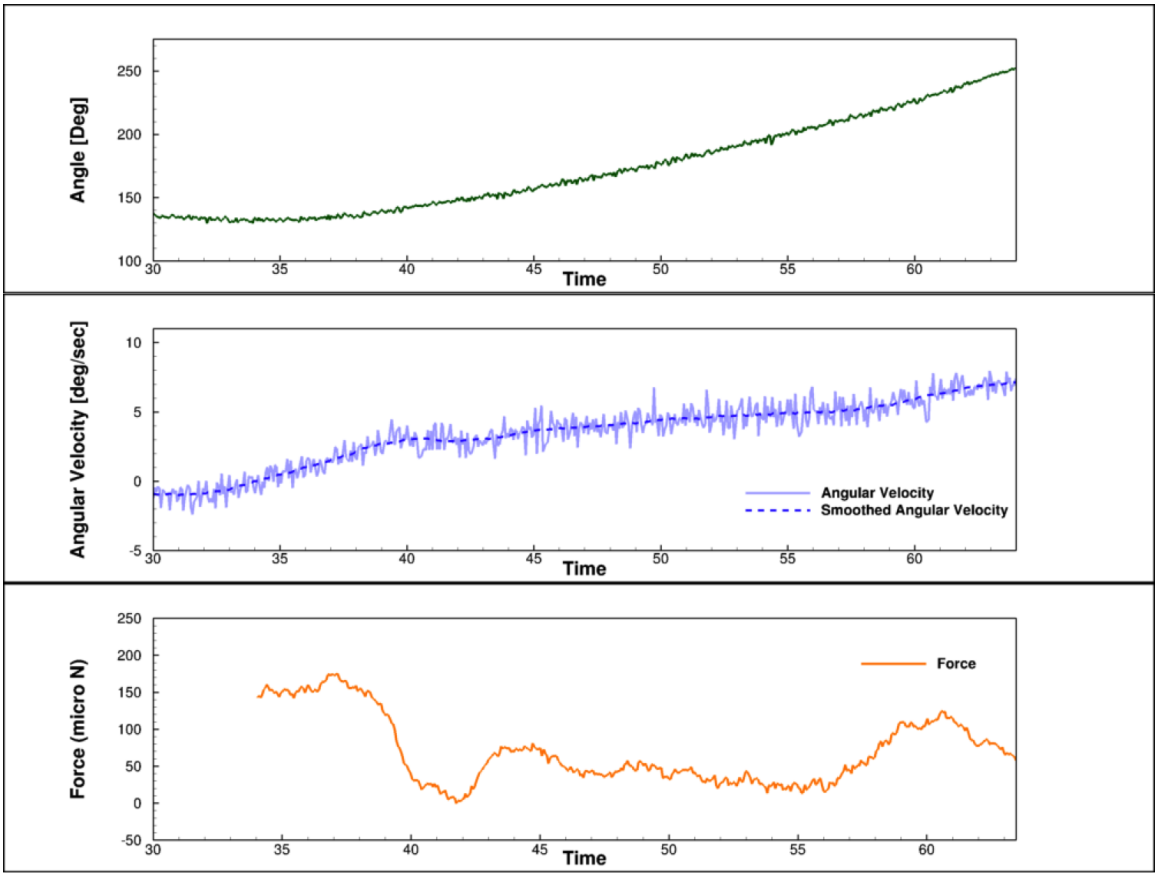

Figure 4.20.: data from first iteration experiment test 7; time is in seconds

After cleaning and activating[9] the FEMTA nozzles, cleaning a FEMTA duplex thrust cell, and filling it with water, the thrust cell is mounted onto the microNewton torsional balance. It is electrically connected to the computer outside of the vacuum chamber and pump down begins.

Figure 4.21 gives the thrust test data for FEMTAs A and and B. These tests were completed with FEMTA A and B loaded into the same duplex. All the data was collected during the same vacuum test.

[9]Activation of the nozzles is achieved by dipping the nozzle for ten seconds in buffered oxide etch during the pre-testing cleaning process. The buffered oxide etch contains hydrofluoric acid, which removes the native silicon oxide layer that grows when bare silicon is exposed to air.

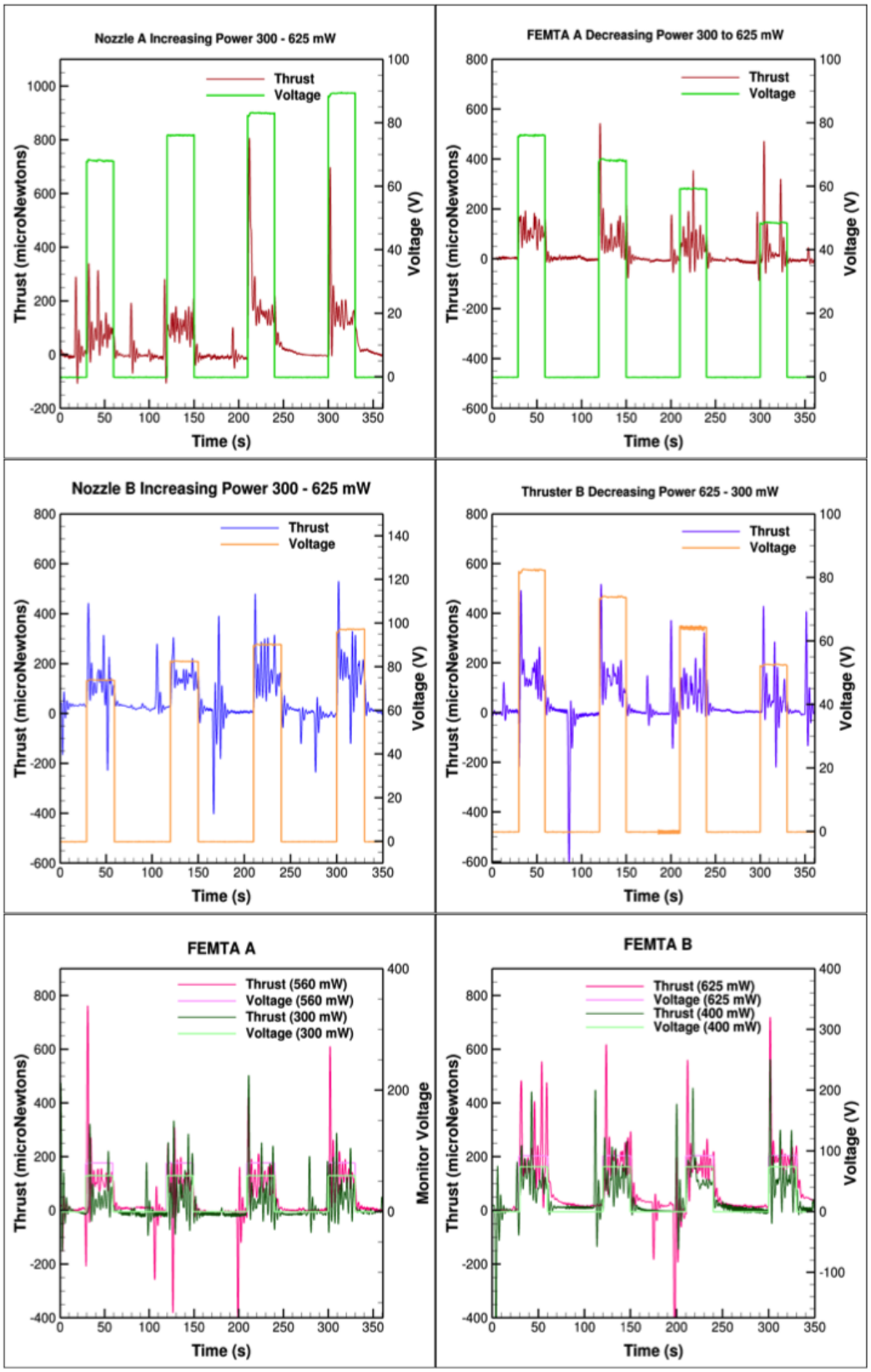

Figure 4.21.: Thrust test data for second iteration experiment FEMTA A and B; test was conducted at a thrust cell chamber pressure of 6kPa

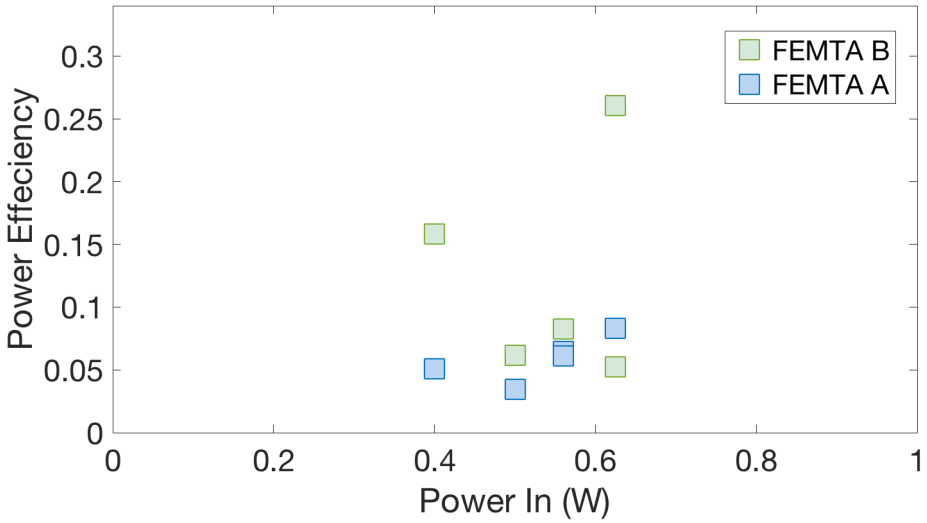

Figure 4.22.: FEMTA power efficiency versus power for FEMTA A and FEMTA B

The FEMTA duplex tests yield slightly different results than other FEMTA tests [74] due to the presence of two nozzles rather than one. When the data shows negative thrust, the opposite thruster has fired. During these tests such firings were unplanned and are undesired. In nearly every case, a negative thrust is simply a single impulse, not a long duration pulse.

Both FEMTA A and FEMTA B responded well to the application of voltage, with very little response time after firing. The large initial over shoot is due to the torsional thrust stand. The thrust stand requires substantial settling time after the initial response. FEMTA B responded better in the varied voltage tests than FEMTA A but both did show a distinct difference in the amount of thrust produced under different power settings.

Figures 4.22 and 4.23 give the power efficiency (as defined in equation **??**) for the two nozzles during thrust testing plotted against power and thrust respectively. FEMTA B did have better efficiency over all though FEMTA A did have more consistent efficiency.

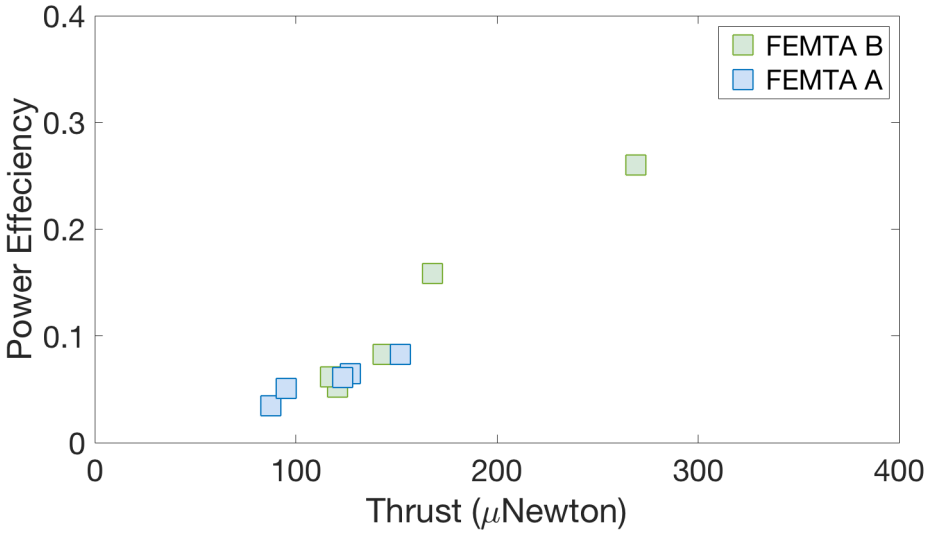

Figure 4.23.: FEMTA power efficiency versus thrust for FEMTA A and FEMTA B

$$\frac{P}{P_{in}} = \frac{Fv_e}{P_{in}} = \frac{T^2}{\dot{m}P_{in}} \tag{4.7}$$

Some ice formation was observed during these tests. The ice has been a problem observed with the fourth generation nozzles. While this issue is still being investigated[10] it is thought to be caused by a slight divergence of the nozzle. The inlet side is slightly thinner than the exit side due to the fabrication procedures. This would cause a significant cooling of the vapor and cause ice to form. When the ice is blown off of or falls off of the thrust cell it is registered by the thrust stand.

1U CubeSat Model Testing

The software and user interface for the second iteration tests were greatly improved over those for the first iteration tests. The User interface included real time plots of

[10]See section 7.1 for more description of the icing issue.

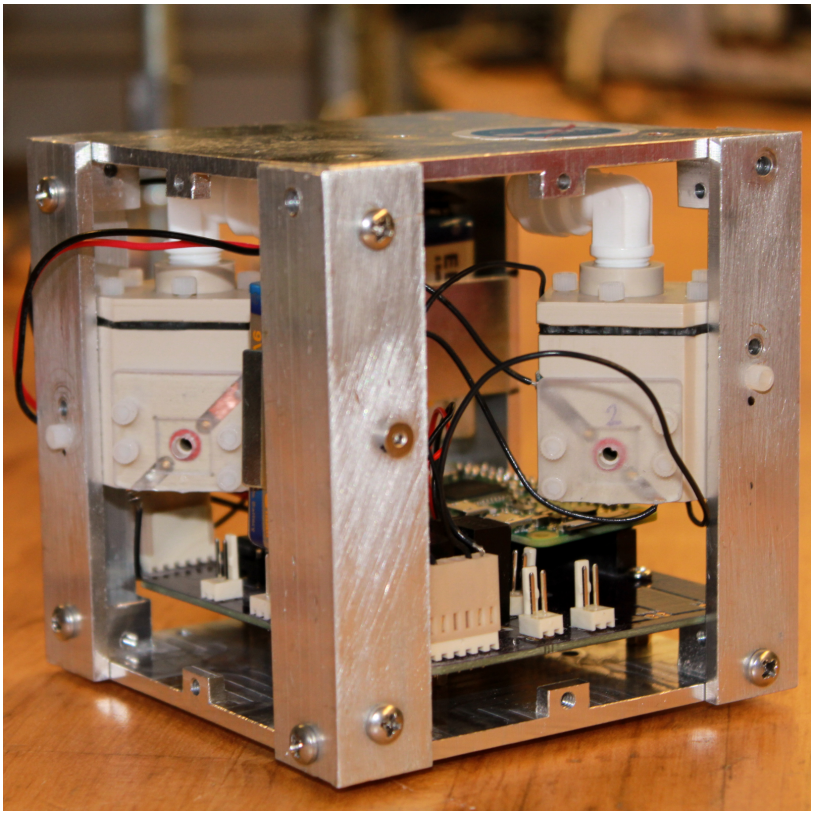

Figure 4.24.: Second iteration CubeSat assembled except for the top mounted solenoid pressure valve

gyroscope, magnetometer, and accelerometer data from both IMUs and the Raspberry Pi Zero W CPU temperature.

The tests have had limited success. While several tests demonstrated a certain amount of controllability, there were several issues related to icing. Testing has thus far been halted while icing is investigated and more nozzles are fabricated. These tests did show that the upgraded hardware resulted in significant improvements to data collection and was much easier to work with.

Figure 4.24 shows the second iteration 1U CubeSat when assembled. The only component not included is the solenoid valve.

Figures 4.27 and 4.28 show two tests with data from when the ion gauge reads that high vacuum has been reached until the system is shut off while pumping back

up to atmospheric pressure. These plots include the angular velocity and the rotation data from the gyroscope and magnetometer respectively. Figure 4.25 is zoomed into a center section of the figures.

First Test

Only one thrust cell was used during this test. The other two nozzles had been compromised during the assembly process, and for the sake of time, one thrust cell was used. FEMTAs A and B correspond to the same FEMTA A and B discussed for thrust testing.

Table 4.3.: Parameters for second iteration test 1

Dry Mass	44.7 g	
Wet Mass	48.6 g	
Final Mass	45.1 g	
Device	**Rotation**	**Resistance**
FEMTA A	Clockwise	73 Ω
FEMTA B	Counterclockwise	84 Ω

Testing parameters are listed in table 4.3. This test observed no leaks. The 1U CubeSat model was allowed to spin at its natural frequency allowing for the torsion from the fishing line to dampen the rotation rate. Both thrusters responded. During the test the only data that explains the motion of the satellite to the user is the gyroscope data, as the raw magnetometer data is relayed to the user in the graphic user interface.

By watching the the satellite angular velocity data, an attempt was made to keep the satellite as close to 0 deg per second of rotation as possible. This portion of the test can be seen in figure 4.25. Compared to the previous oscillations in both position

and angular velocity, this is a relatively still satellite. Both FEMTA nozzles were fairly responsive, jumps in pressure were noticed when the thrusters were fired.

Once again, this was a manual control demonstration. It did prove that both the pressure relief valve, the new FEMTA duplex thrust cell, and the software were able to complete a high vacuum test. Figure 4.26 indicates the predicted harmonic motion of the 1U FEMTA CubeSat Model during the first test if there were no thrusts while attempting to hold the angular velocity at 0 deg/sec. This demonstrates that the thrusters did impact the satellite rotation.

Second Test

This test was run similarly to the first test. This time, both thrust cells were loaded and had two FEMTAs. FEMTA A and B remained the same, while FEMTA D and E were new.

The thrusters were much less responsive during this test. Pressure jumps did not occur as the thrusters were fired, but sporadically afterward or when not asked to fire. Due to this lack of response, it is inconclusive as to whether or not the thruster that was powered was the thruster that caused the pressure jump. The pressure in the FEMTA duplex thrust cells may have been too low, and a breach occurred in FEMTA D at lower pressure than expected during the assembly pressure check. This lead to the decision to lower the internal pressure in the FEMTA duplex thrust cells.

A similar control test was attempted as in Test 1. Figure 4.25, shows the angular position and velocity data during this control test. It is clear that less control was achieved as the system oscillates significantly more than in test 1. However the angular velocity does have less amplitude than it does when allowed to spin freely.

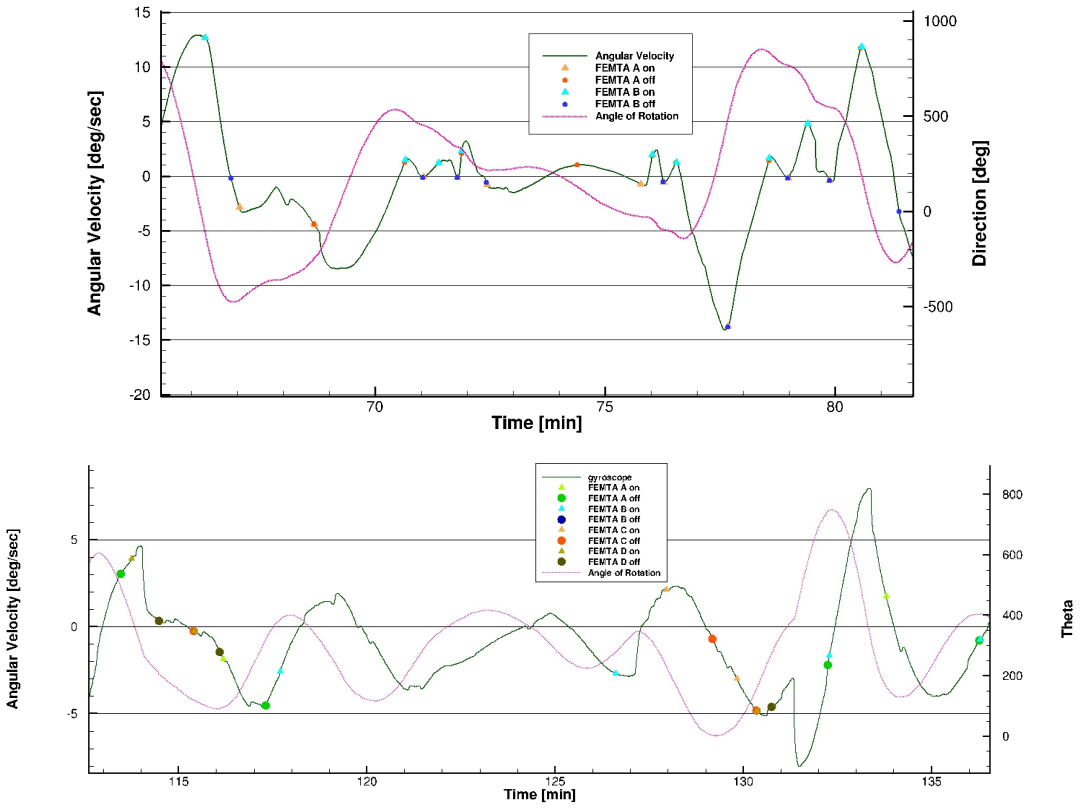

Figure 4.25.: Magnified test rotational data during manipulation phase. Upper: Test 1 data. Lower: Test 2 data from figures 4.27 and 4.28

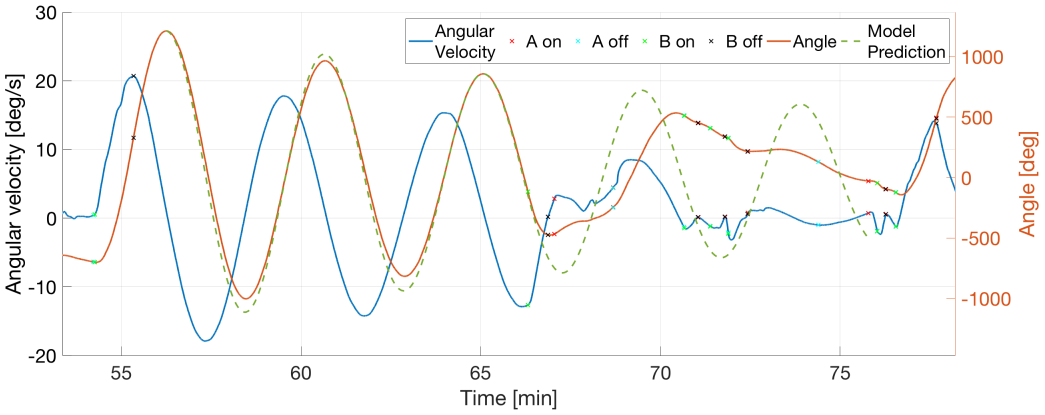

Figure 4.26.: Magnified test rotational data during manipulation phase. Upper: Test 1 data. Lower: Test 2 data from figures 4.27 and 4.28

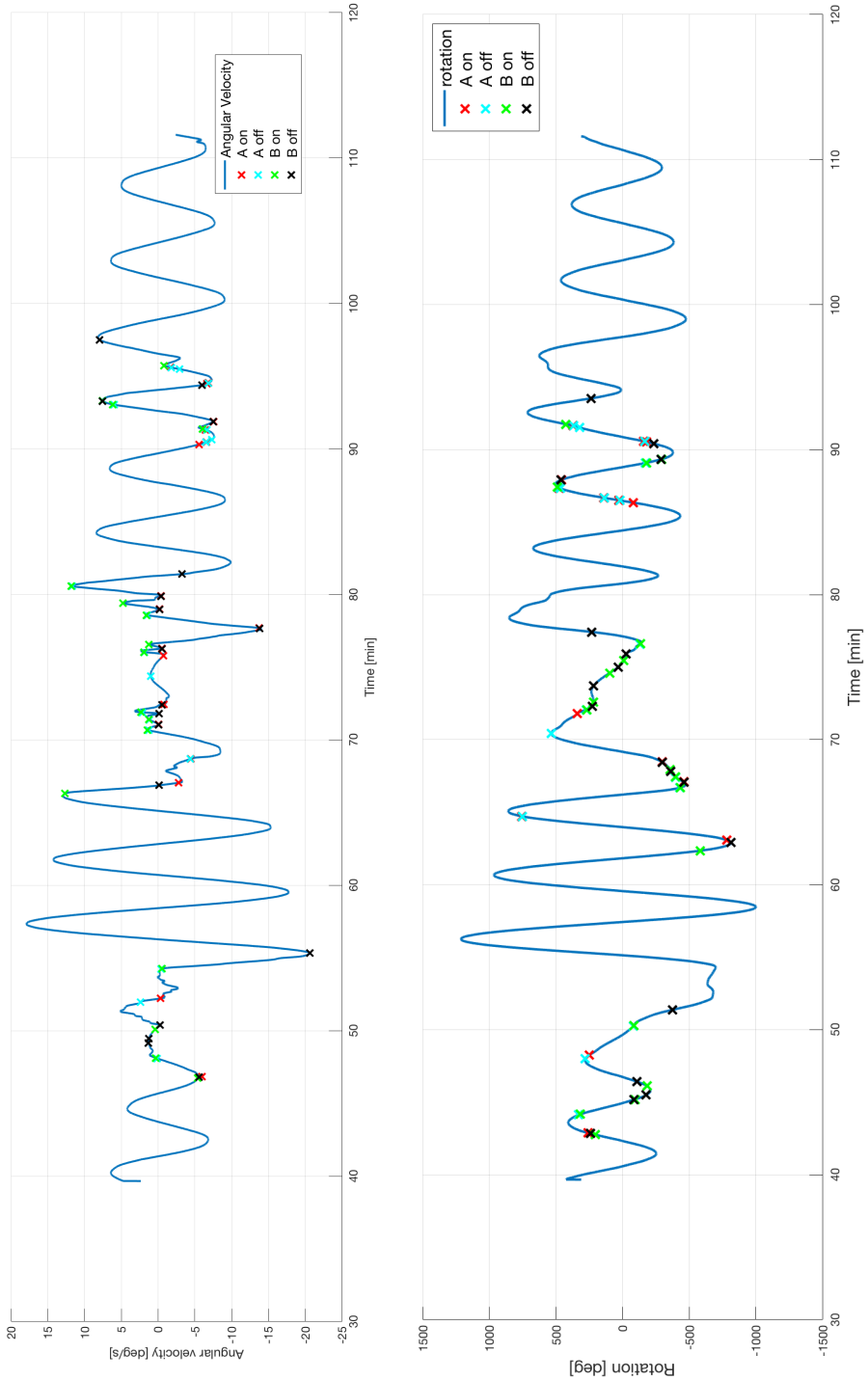

Figure 4.27.: Full test 1 gyroscope and magnetometer data with thruster on and off markers

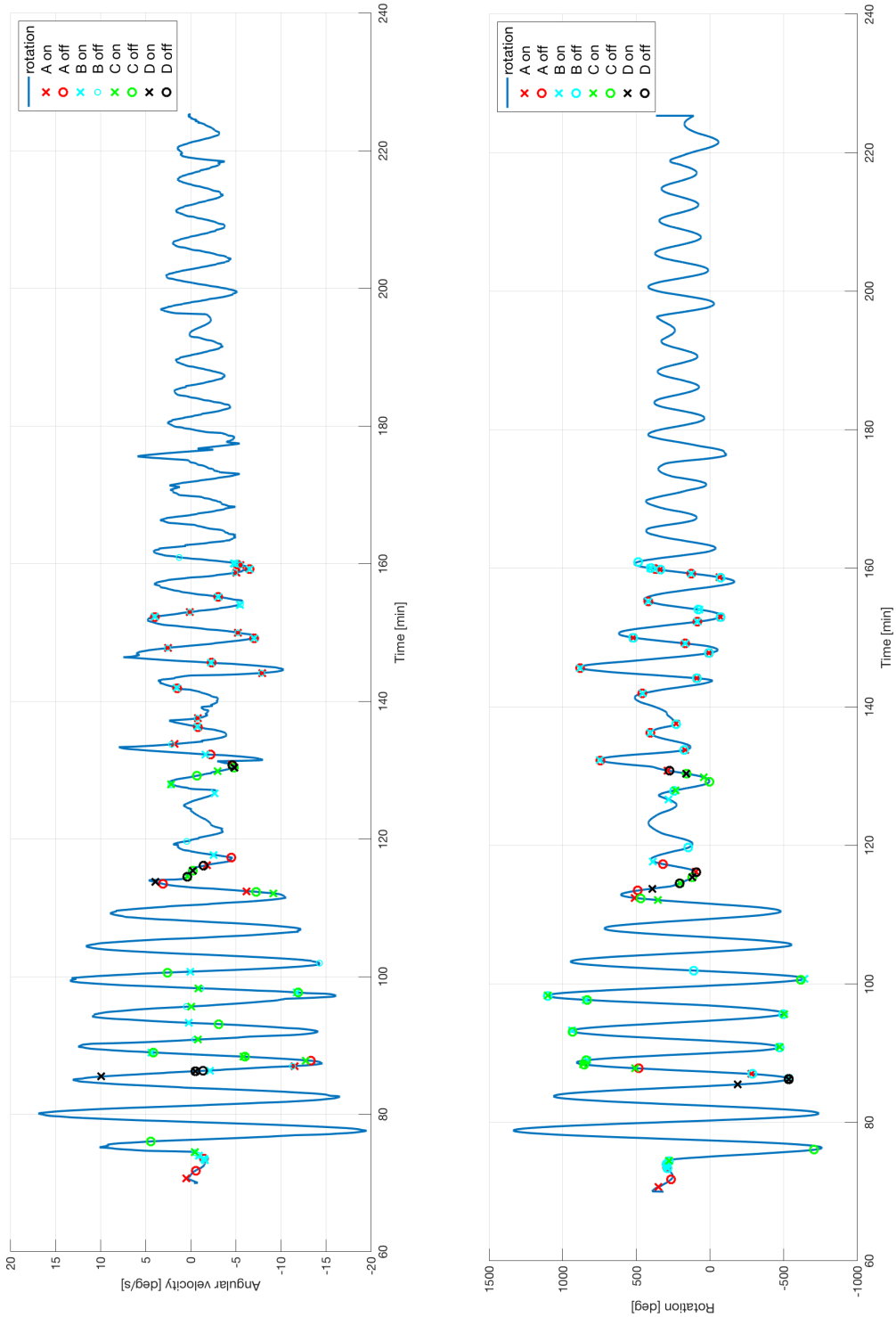

Figure 4.28.: Full test 2 gyroscope and magnetometer data with thruster on and off markers

5. SMALL SATELLITE ATTITUDE CONTROL TRADE STUDY

The previous sections have provided a detailed, but not exhaustive survey of micro propulsion solutions being developed for small satellites with specific interest in micropropulsion for CubeSats. Most studies that have performed trade studies, such as Hudson et al., for micropropulsion have done so considering the maximum velocity change that can be provided by the propulsion system. This study compared the micropropulsion devices based on orbit change maneuvers and had particular interest in possible mission architectures for electric micropropulsion [45]. This trade study aims to consider the proper range of use for micropropulsion as an attitude control system as well, paying close attention to pico and nanosatellites.

Equation 2.8, repeated below, gives the relationship between the specific impulse and the mass fraction (the mass before a propulsive maneuver divided by the mass after the propulsive maneuver).

$$\Delta V = v_e \ln\left(\frac{m_i + m_p}{m_i}\right)$$

Figure 5.1 gives this relationship with increasing mass fraction for various specific impulse. The maximum mass fraction for a CubeSat can be theorized to be 2, with half the mass being devoted to propellant. However, in many cases, the propellant mass fraction is restricted to be much less. Increased specific impulse is always going to yield better results, however Mass fraction is very important consideration for small satellites as well.

Attitude control on satellites has typically been conducted using MCS, as discussed in chapter 3. However, these systems are heavy,large, and consume considerable amounts of power. CMGs require a significant amount room to gimbal, and multiple

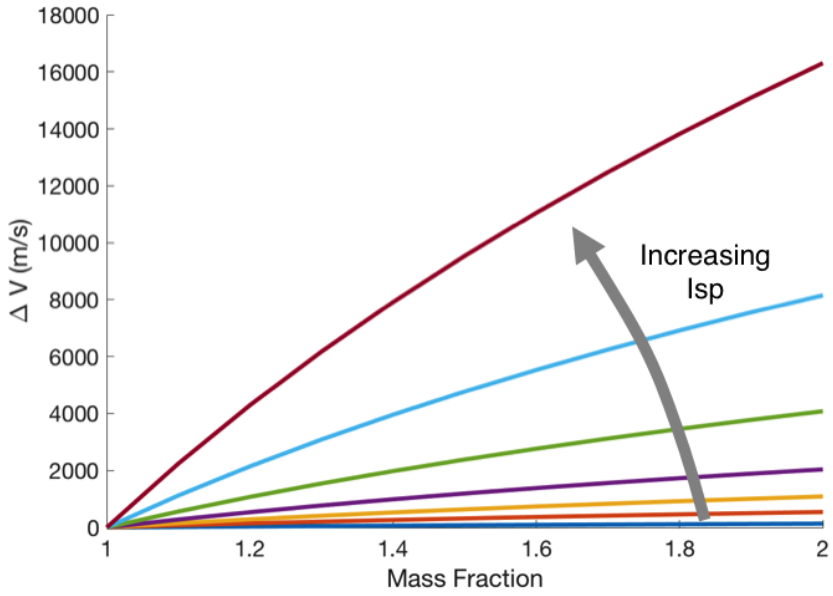

Figure 5.1.: ΔV versus mass fraction for several specific impulses calculated by equation 2.8

reaction wheels are required to complete an attitude control system (ACS). Sinclair International has the most the reaction wheels that are the most compatible with microsatellites, and Honeybee Robotics creates a CMG that is similar in size to a golf ball [71] [76]. However, CMG systems requite a secondary momentum system as the wheels can become saturated and provide no further torque to the system. Often, thrusters are employed to desaturate momentum wheels.

Due to these constraints, this study gives attention to micropropulsion as a method of ACS. Table 5.1 gives operational ranges for the surveyed micropropulsion systems. Figures 5.2, 5.3, and 5.4 show scatter plots of the surveyed technologies[1].

Figures 5.2, 5.3, and 5.4 show that the chemical thrusters tend to have higher thrust and consume less power and have a lower specific impulse than the electrical

[1]The data and sources used to generate the table and figures is in appendices B and C.

Table 5.1.: Thrust, power, specific impulse, volume, and mass ranges for the micropropulsion systems surveyed; if blank, a range was not provided in literature

Type	**Thrust (mN)**	**Power (W)**	**Isp (sec)**	**Volume**	**Mass (kg)**
Mono-prop	100-4500	10.0-72.0	131-310	1U - 3U	0.5- 1.5
Green	.25-26900	10.0-28.0	196-255	1U-3U	0.38-5.0
Bi-prop	22000	9.0 - 41.0	292-310		
cold	0.05-1200	1.0-55.0	40-100	$\frac{1}{4}$U - 3U	0.02-2.5
Resisto-jet	4.0 - 5400	5.0-20.0	209-255	$\frac{1}{4}$U - 2U	
Ion	0.22-1.5	28-80	790-3200		
Hall	0.13-325	20-10000	1300-3060	1U	1.0-25
Colloid	0.005-0.7	8.0-15	800-3744	$\frac{1}{2}$ U	0.16-1.15
FEEP	0.01-1	8-400	2000-6000	$\frac{1}{2}$ U	0.87-8.0
PPT	0.02-0.14	0.5-12.5	500-590	$\frac{1}{3}$ U	0.2-3.8
Helicon	0.2-15	30-100	500-2600	1U	0.2-3.0
FEMTA	0.006-0.100	0.1-0.5	74	$\frac{1}{4}$U - 2U	0.13

thrusters. Figure 5.4 does show that the higher the thrust, typically the lower the specific impulse.

Nanosatellites are highly constrained in mass, power, and volume in ways that are prohibitive for some methods of micropropulsion. Typically, CubeSats are only able to provide 10 Watts of power due to collection, storage, and distribution constraints [15]. The orange lines on figures 5.2 and 5.3 marks 10 Watts on the plot. To the left of this line, are micropropulsion systems that operate within the power levels for a CubeSat. In figure 5.2 this shows that the force threshold for the power

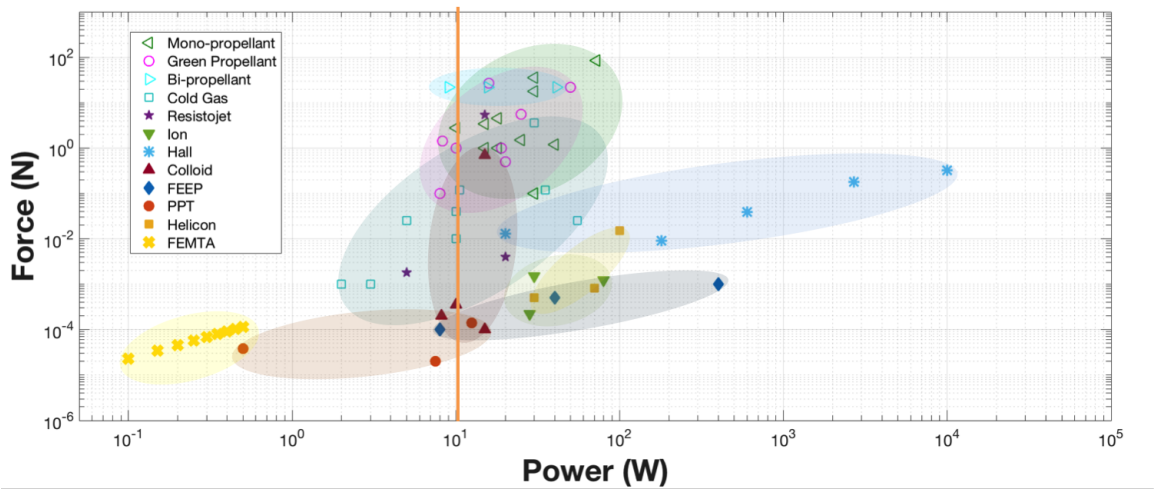

Figure 5.2.: Force versus power for surveyed micropropulsion systems.

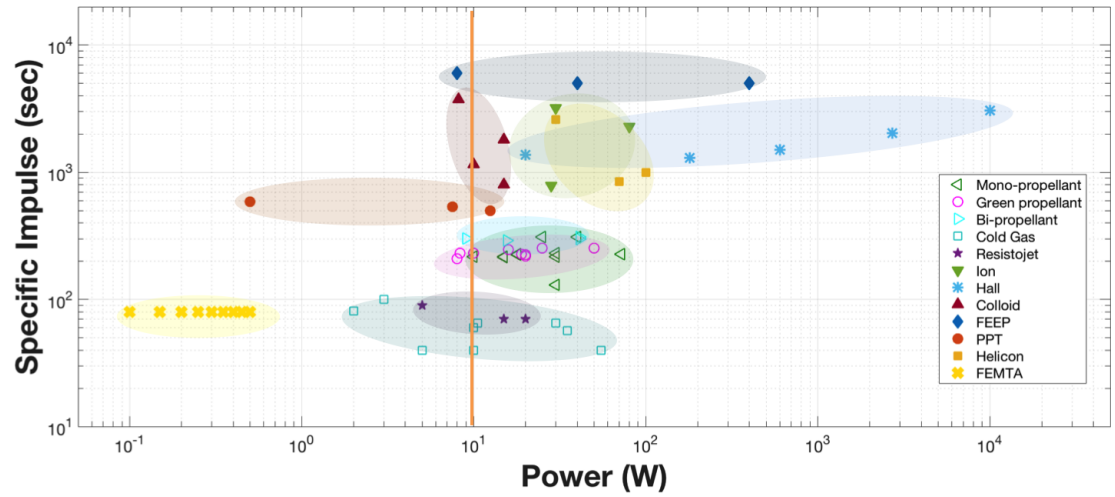

Figure 5.3.: Specific Impulse versus power for surveyed micropropulsion systems

constraint is approximately 10 Newtons. The specific impulse threshold in figure 5.3 is approximately 1000.

Systems that provide more that 10 Newtons of thrust and more than 1000 seconds of specific impulse are most likely too expensive for the power budget of a CubeSat.

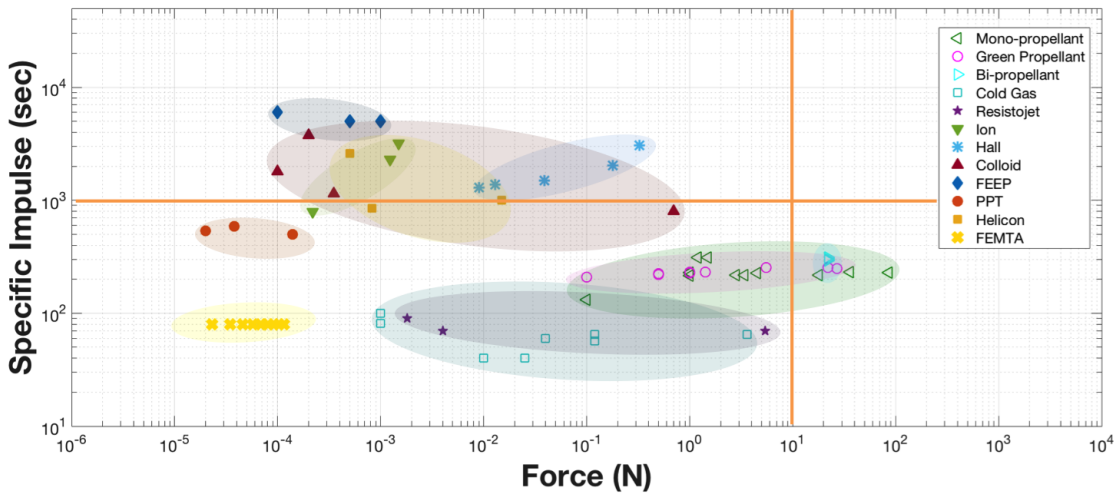

Figure 5.4.: Specific impulse versus force for surveyed micropropulsion systems

Combining these thresholds on figure 5.4 gives a good reference to which systems may operate well on a CubeSat. Figure 5.4 shows that PPT, resistojets, cold gas thrusters, and FEMTA all operate below 1000 seconds of specific impulse and 10 Newtons of force. Some colloid thrusters, helicon thrusters, green propellant, and mono-propellant thrusters operate in this range as well.

This comparison does not give a complete picture of which systems are feasible for use on nanosatellites. A basic math model was thus developed to further compare the systems.

5.1 Spacecraft Attitude Dynamics Mathematical Model

One of the most basic maneuvers in spacecraft attitude dynamics is a slew through an angle to point the spacecraft in a new direction. This is achieved by providing a specific torque to the spacecraft. Micropropulsion systems provide torques based on their distance from the center of mass and the center of gravity and the magnitude and direction of the thrust. Figure 5.5 defines these vector quantities.

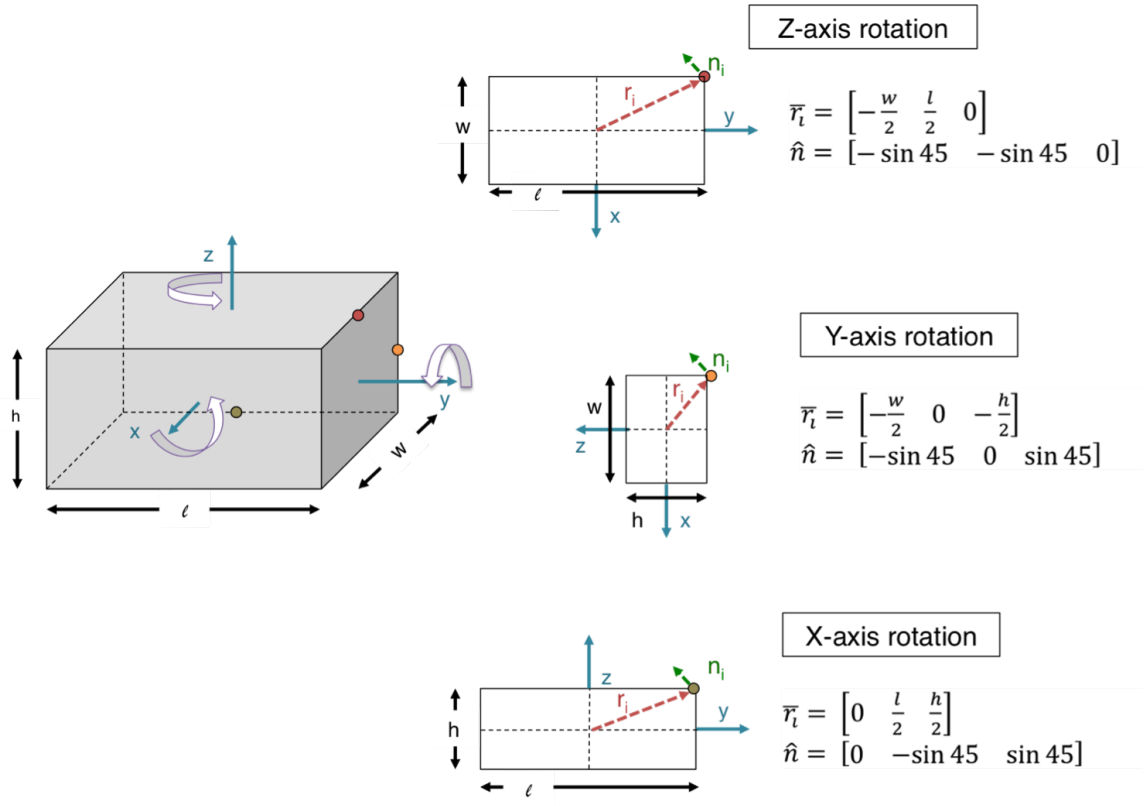

Figure 5.5.: Definition of the physical vector quantities for the mathematical model for rotation about each axis

This model assumes that the satellite being analyzed has an even mass distribution, allowing the center of mass and center of gravity to be located in the geometrical center of the satellite. The width of the satellite is aligned with the x axis, the length is aligned with the y axis, and the height of the satellite is aligned with the z axis. The rotation about the z axis is the precession, the rotation about the y axis is the nutation, and the rotation about the x axis is the spin. The thrusters are place so that they have the longest moment arm, $\bar{r}_i$, from the center of mass. This allows the thruster to provide maximum torque.

The torque, τ due to force is calculated by multiplying the thrust, F, by the cross product of the moment arm and the normal vector, $\hat{n}$, in the direction of the thrust.

$$\bar{\tau} = F\left(\bar{r_i} \times \hat{n}\right) \tag{5.1}$$

The moment of inertia (also reffered to as the inertial matrix) for a rectangular prism with an even mass distribution is a factor of the mass, m, and dimensions of the satellite.

$$\mathbf{I} = \frac{m}{12}\begin{bmatrix} l^2+h^2 & 0 & 0 \\ 0 & w^2+h^2 & 0 \\ 0 & 0 & l^2+w^2 \end{bmatrix} \tag{5.2}$$

The definitions of the width, w, length, l, and height, h, for equation 5.2 are given in figure 5.5. This model assumes the moment of inertia does not change. In a real system, the moment of inertia would not be ideal as the mass would not be evenly distributed and the mass would change with time, and thus the inertia would change with time. However, for the sake of this comparison, assuming a constant moment of inertia is sufficient.

The time rate of change of the change of the angular velocity at a given time is a function of moment of inertia, and the torque provided by the thruster. Equation can be solved for the angular acceleration using Euler angles.

$$\mathbf{I}\frac{d\bar{\omega}}{dt}\left(t\right) = \bar{\tau} - \left(\bar{\omega}\left(t\right) \times \mathbf{I}\bar{\omega}\left(t\right)\right) \tag{5.3}$$

Table 5.2 gives the average values for thrust, power and specific impulse for each thruster type considered. As can be seen, the chemical thrusters generate an average thrust that is up to several orders of magnitude greater than the electric propulsion thrusters. For this reason, the chemical propulsion thrusters were not used for this model.

The model simulates a very rudimentary control system for achieving a slew on of a satellite. A single thruster is fired for 5 seconds, left off for 5 seconds, and then fired in the opposite direction for 5 seconds.

Figure 5.6 illustrates the four satellite configurations used in the math model. 1U, 3U, 6U and 12U microsatellites are common CubeSat configurations. Each 1U is a standard 10 cubic centimeters and 1.33kg.

Table 5.2.: Average values for the types of micropropulsion surveyed. The weighted average removes the outliers from the data set

Type	**Weighted Mean Thrust (mN)**	**Mean Power (W)**	**Mean Isp (sec)**
Mono-prop	2200	30	230
Green	1650	20	230
Bi-prop	22000	30	300
cold	250	20	70
Resistojet	2.9	15	80
Ion	1	45	2000
Hall	26	270	1400
Colloid	0.34	10	1900
FEEP	0.533	150	5300
PPT	0.06	7	540
Helicon	0.66	70	1490
FEMTA	0.006-.1	0.25	74

The model simulated rotation about each axis as described in figures 5.5 and 5.6. The 1U CubeSat rotates the same amount about each axis as all sides of the cube are the same length. The 3U and the 12U CubeSats rotate the same amount about the y and x axis as these axes had the same dimensions for the inertia matrix computation. Tables 5.3 through 5.6 include the total angle change the satellite underwent in the 15 second slew maneuver. Only the systems that would fit inside of the CubeSat volume were used, and if a system imparted too much (>>1 revolution) or too little thrust (<< 1 deg), it was not reported.

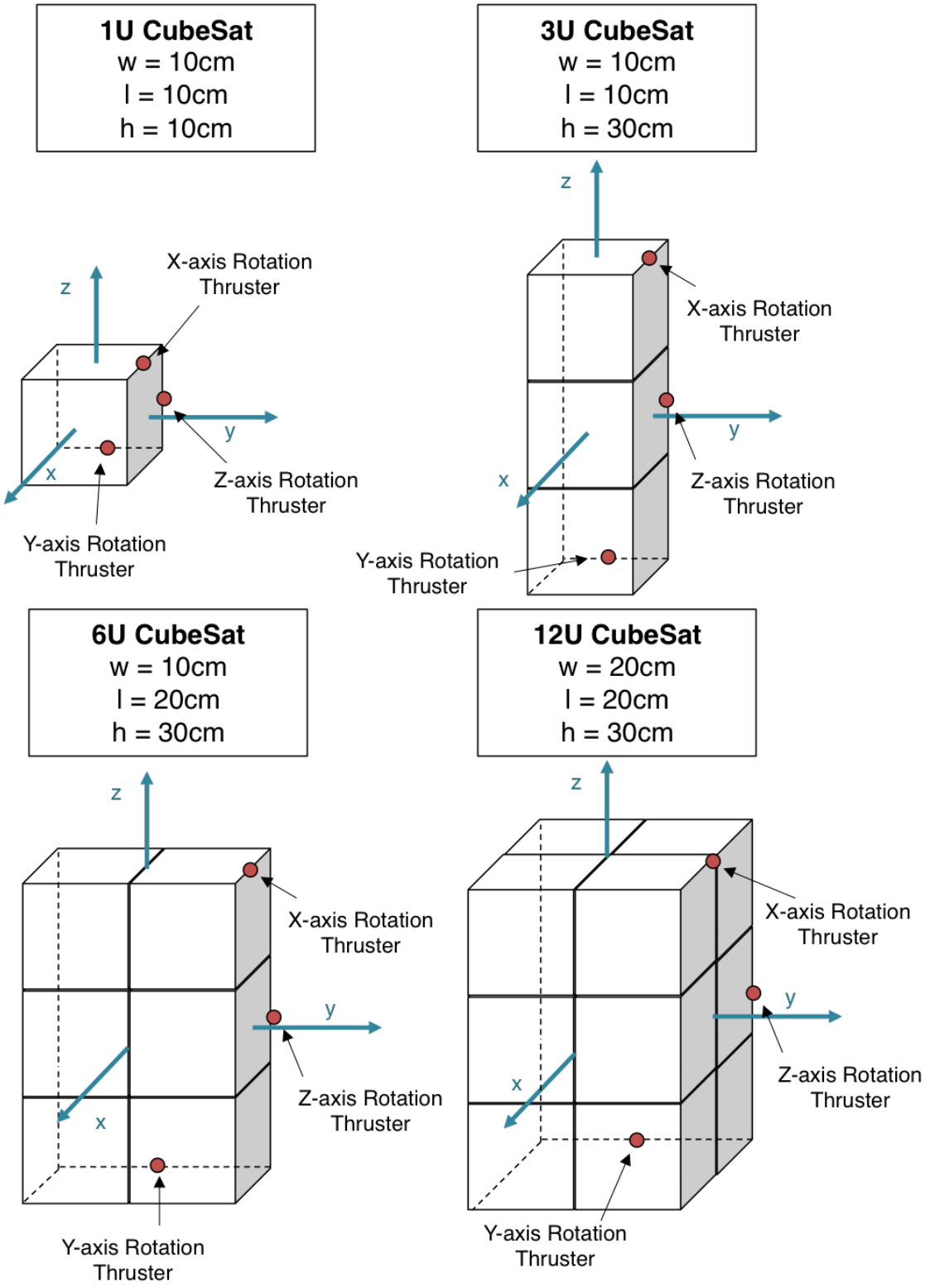

Figure 5.6.: Configurations for the four satellites used in the mathematical model

Table 5.3.: 1U rotation due to micropropulsion, 15 second slew maneuver

Type	**Weighted Mean Thrust (mN)**	**Volume**	**Mass (kg)**	**1U**		
Axis of Revolution				z	y	x
				deg	deg	deg
Colloid	0.34	$\frac{1}{2}$ U	0.16-1.15	31.0	31.0	31.0
FEEP	0.533	$\frac{1}{2}$ U	0.87-8.0	48.6	48.6	48.6
PPT	0.06	$\frac{1}{3}$ U	0.2-3.8	5.47	5.47	5.47
FEMTA	0.006	$\frac{1}{4}$ U	0.13	0.55	0.55	0.55
	0.1			9.12	9.12	9.12

Table 5.4.: 3U rotation due to micropropulsion, 15 second slew maneuver.

Type	**Weighted Mean Thrust (mN)**	**Volume**	**Mass (kg)**	**3U**		
Axis of Rotation				z	y	x
				deg	deg	deg
Resistojet	2.9	$\frac{1}{4}$U - 2U		88.1	35.2	35.2
Ion	1			30.4	12.2	12.2
Hall	26	1U	1.0-25	790	316	316
Colloid	0.34	$\frac{1}{2}$ U	0.16-1.15	10.3	4.13	4.13
FEEP	0.533	$\frac{1}{2}$ U	0.87-8.0	16.2	6.48	6.48
PPT	0.06	$\frac{1}{3}$ U	0.2-3.8	1.82	0.73	0.73
FEMTA	0.006	$\frac{1}{4}$U	0.13	0.182	0.07	0.07
	0.1			3.04	1.22	1.22

Table 5.5.: 6U rotation due to micropropulsion, 15 second slew maneuver

Type	**Weighted Mean Thrust (mN)**	**Volume**	**Mass (kg)**	**6U**		
Axis of Rotation				z	y	x
				deg	deg	deg
Resistojet	2.9	$\frac{1}{4}$U - 2U		26.4	17.6	16.9
Ion	1			9.12	6.08	5.84
Hall	26	1U	1.0-25	237	158	152
Colloid	0.34	$\frac{1}{2}$ U	0.16-1.15	3.1	2.07	1.99
FEEP	0.533	$\frac{1}{2}$ U	0.87-8.0	4.86	3.24	3.11
PPT	0.06	$\frac{1}{3}$ U	0.2-3.8	0.55	0.36	0.35
Helicon	0.66	1U	0.2-3.0	6.02	4.01	3.86
FEMTA	0.1	$\frac{1}{4}$U	0.13	0.91	0.61	0.58

Table 5.6.: 12U rotation due to micropropulsion, 15 second slew maneuver

Type	**Weighted Mean Thrust (mN)**	**Volume**	**Mass (kg)**	**12U**		
Axis of Rotation				z	y	x
				deg	deg	deg
Resistojet	2.9	$\frac{1}{4}$ U-2U		11.0	8.47	8.47
Ion	1			3.80	2.92	2.92
Hall	26	1U	1.0-25	98.8	76	76
Colloid	0.34	$\frac{1}{2}$ U	0.16-1.15	1.29	0.99	0.99
FEEP	0.533	$\frac{1}{2}$ U	0.87-8.0	2.02	1.56	1.56

Appendix H includes the angle trajectories that helped verify that the slew angles calculated were correct. This data confirms that the smaller thrust devices are able to rotate a satellite slower than a large thrust device. While all of these devices have a lowest and a highest thrust, the weighted average was used as a representative of all the devices. As part of the demonstration of ability for FEMTA, the minimum and maximum values for reported thrust were used.

The desirable change in angle for this maneuver is less than 25 degrees, as the maneuver is only 15 seconds and this would confirm that the angular acceleration is not destabilizing.

For the 1U satellite the PPT and FEMTA provide the smallest slew angle. This results in less angular acceleration on the satellite. Both of these operate in a viable power range for small satellites. Depending on the mission the third or quarter U volume may be reasonable on a 1U CubeSat.

It may be more reasonable to have propulsion on a 3U CubeSat. There is more volume available for a payload and the size expands the mission capability of the satellite. For a 3U CubeSat the FEMTA, PPR, FEEP, and colloid thrusters provide sufficient torque for the maneuver. However FEEP engines require significant operational power.

For a 6U CubeSat, significantly more volume and mass can be dedicated to a micropropulsion system, but this is also the form factor where reaction wheels begin to be more feasible. Helicon thrusters, PPT, FEEP, Colloid, Ion thrusters, and resistojets are all able to provide a desirable range of torque to turn the model satellite a reasonable amount in 15 seconds. FEEP, ion Thrusters, and resistojets are also satisfactory for 12U satellites. It is still important to note that ion thrusters and FEEP due require large amounts of operational power, possibly making them impractical for CubeSat use.

6. CONCLUSIONS

The trade study has shown that there exists a gap in low thrust and low power devices for nanosatellites such as CubeSats. CubeSats are only able to provide approximately 10 Watts of power for 6U (8 kilograms) or less. The only propulsion systems that operate in that restricted power range are FEMTA, PPT, some colloid thrusters, some cold gas thrusters, and some resistojets. However, for 3U (4 kilograms) systems and smaller, the only two micropropulsion systems that are reasonable are PPT and FEMTA. FEMTA is able to reach a lower thrust range (0.006-0.1 milliNewtons) than PPT (average 0.06 milliNewtons) and requires an order of magnitude less power (up to 1 Watt versus 10 Watts).

For 3U to 6U CubeSat range FEMTA and PPT would be able to make small adjustments for attitude control ($<$ 5 degrees of rotation), however colloid thrusters also become feasible options with a slightly larger thrust available (0.34 milliNewtons).

At 12U (16 kilograms), more power is likely available due to better power generation (larger solar arrays) and storage (larger batteries and power processors). Colloid thrusters can preform small adjustments while Resistojets become better suited for larger slew maneuvers. Above this form factor, it is also advantageous to consider micropropulsion to be coupled as an attitude control mechanism and a orbit change system, making the higher Efficiency electric propulsion devices more suitable. Additionally, above a 12U CubeSat, the volume and mass limits are less constrained, making MCS another attractive solution for attitude control.

7. FUTURE WORK

7.1 Icing

FEMTA is a maturing technology. Though microcapillary action has been used in a similar method for inkjet printers[1] [77], the technology as a thrust device is still quite novel. The exact mechanism and operation within the micronozzle are not well understood. The flow is difficult to model with DSMC and heat transfer analysis as the flow occupies a transitional mode of gas dynamics.

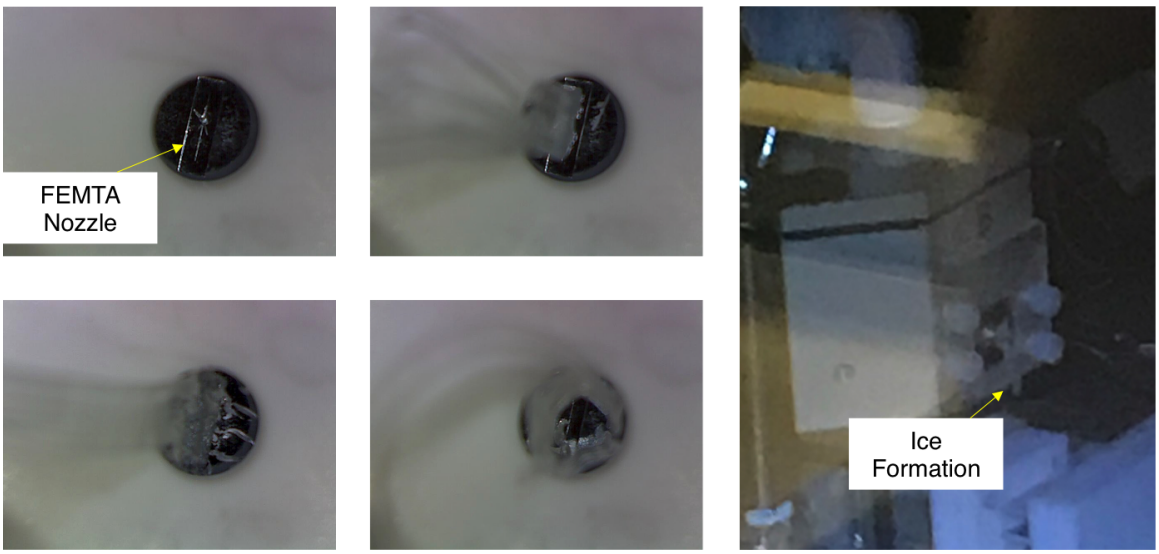

Figure 7.1.: Left: Ice ribbons formed during firing in vacuum chamber; Right: An icicle formation on the acrylic faceplate of the second iteration FEMTA duplex thrust cell during thrust testing

[1]Inkjet printers also exploit the capillary effect by heating a fluid in a micro-capillary channel, however, inkjet printers form precise drops on paper, while FEMTA generates a plume of water vapor.

One of the major developments in the fourth generation was the observation of ice near the exit of the nozzle. The first evidence of this was seen during the first iteration 1U CubeSat model testing, where the ejection of ice was seen and captured during a recording. Subsequently, during thrust testing for the second iteration FEMTA

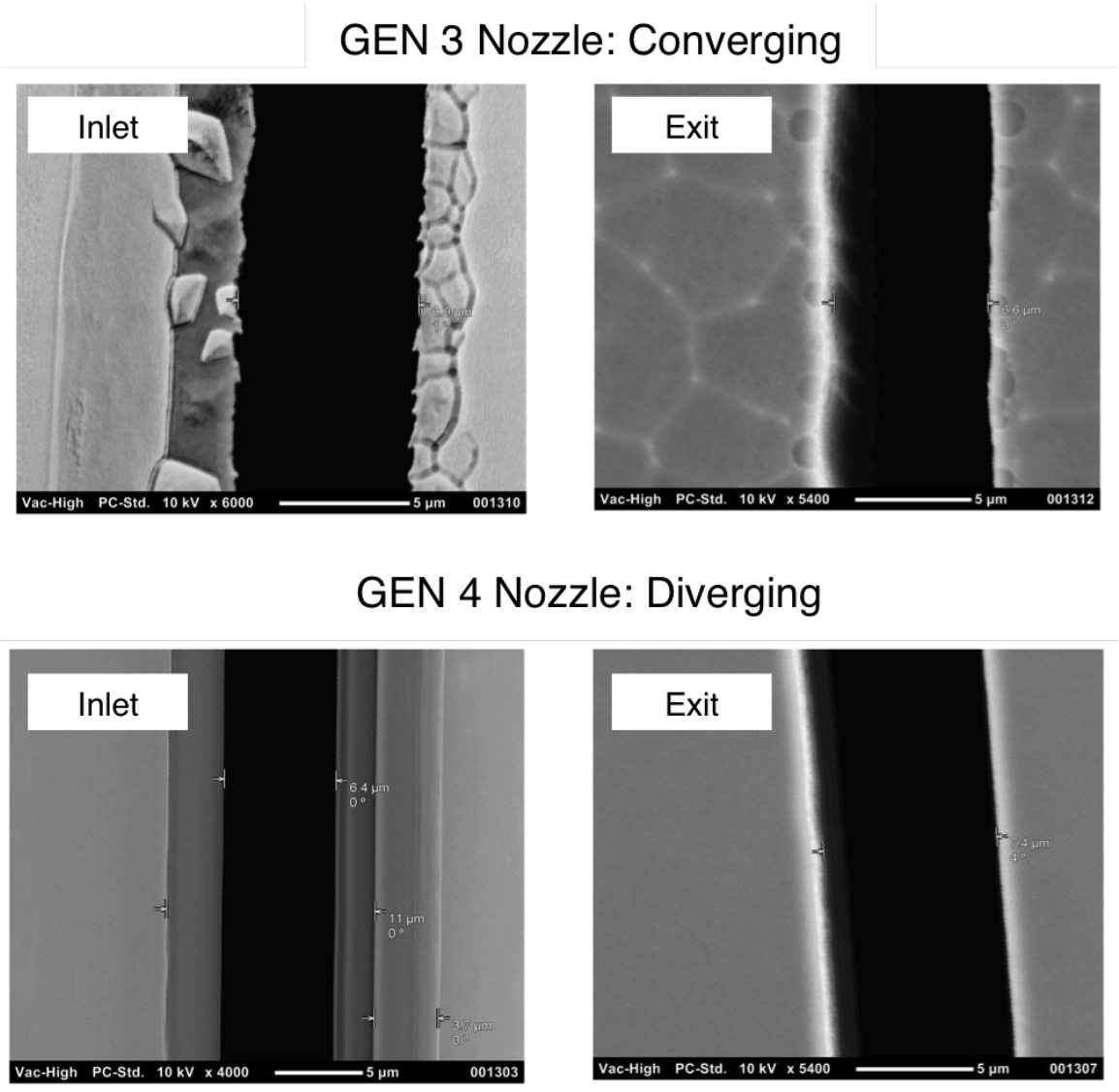

Figure 7.2.: Top: SEM image for third generation FEMTA. Bottom SEM image for fourth generation FEMTA

duplex thrust cell, ice was viewed forming on the acrylic faceplate of the thrust cell (pictured in figure 7.1).

Ice formation had not been viewed on previous thrust cell iterations from third generation FEMTA testing. The cover plates for these test vessels were made from Teflon or ceramic, leading to a hypothesis that the ice may be forming on the acrylic do to physical properties. However, as also seen in figure 7.1, a video from a digital microscope inside of the chamber showed ice ribbons being ejected from the FEMTA nozzle. While the acrylic may be responsible for the collection of ice, the ice is being formed at the nozzle.

Figure 7.2 shows scanning electron microscope (SEM) images of the inlet and exit on a third generation nozzle and a fourth generation nozzle. By taking measurements of the nozzle inlet and exit widths, it was determined that the third generation nozzles, which did not experience icing, were convergent (inlet width > exit width) and the fourth generation nozzles were divergent (inlet width < exit width). The widths are given in table 7.1.

Table 7.1.: Third and fourth generation nozzle inlet and exit widths

	Inlet Width (microns)	**Exit Width (microns)**
Third Generation	6.9	6.6
Fourth Generation	6.4	7.4

A diverging nozzle would cause expansion and cooling of the water vapor, which would explain the formation of ice. The difference between the third generation nozzle fabrication and fourth generation nozzle fabrication is in the silicon etching machine used. The previous machine did not work properly, which is perhaps responsible for the slight convergence to the nozzle. A new etch recipe is being generated that will vary the etching and passivization step lengths to avoid divergence in the nozzle.

7.2 Shutters

Shutters are being developed to avoid propellant loss through quiescent evaporation. A previous design was a MEMS bi-morph shutters that would open when voltage was supplied to FEMTA. The current design was developed to reduce cost and hopefully as a method to ease fabrication. The current shutter design being tested is a COTS micro-aperture shutter from a camera that covers the exit of FEMTA and is opened immediately before the FEMTA is fired.

7.3 Zero G Propellant Tank

The current thrust cell designs are gravity fed fuel systems. In order to provide the necessary back pressure when in orbit or deep space, a micro gravity propellant feed system is necessary. Preliminary testing has begun on such a propellant tank, pictured in figure 7.3. This tank uses the vapor pressure of an alcohol mix to apply a pressure to a membrane bladder separating the alcohol mixture from the water propellant. As water is removed from the system by firing, the volume of gaseous alcohol changes and the bladder is deformed to retain the constant back pressure for the water.

Concept testing has been accomplished with ethylene glycol in the small vacuum chamber. Further design apparatuses are being designed.

7.4 1U CubeSat Model Testing

The 1U CubeSat model single axis of rotation tests were done in conjunction with an undergraduate research class. Further testing and development of a 1U system is scheduled. Proof of controllability will require the development of a control algorithm and a frictionless and low torsional harnessing system to hang the satellite. A control system is currently being tested while new, non-diverging fourth generation nozzles are fabricated with quad-coptor rotors at atmospheric pressure. The goal is to have

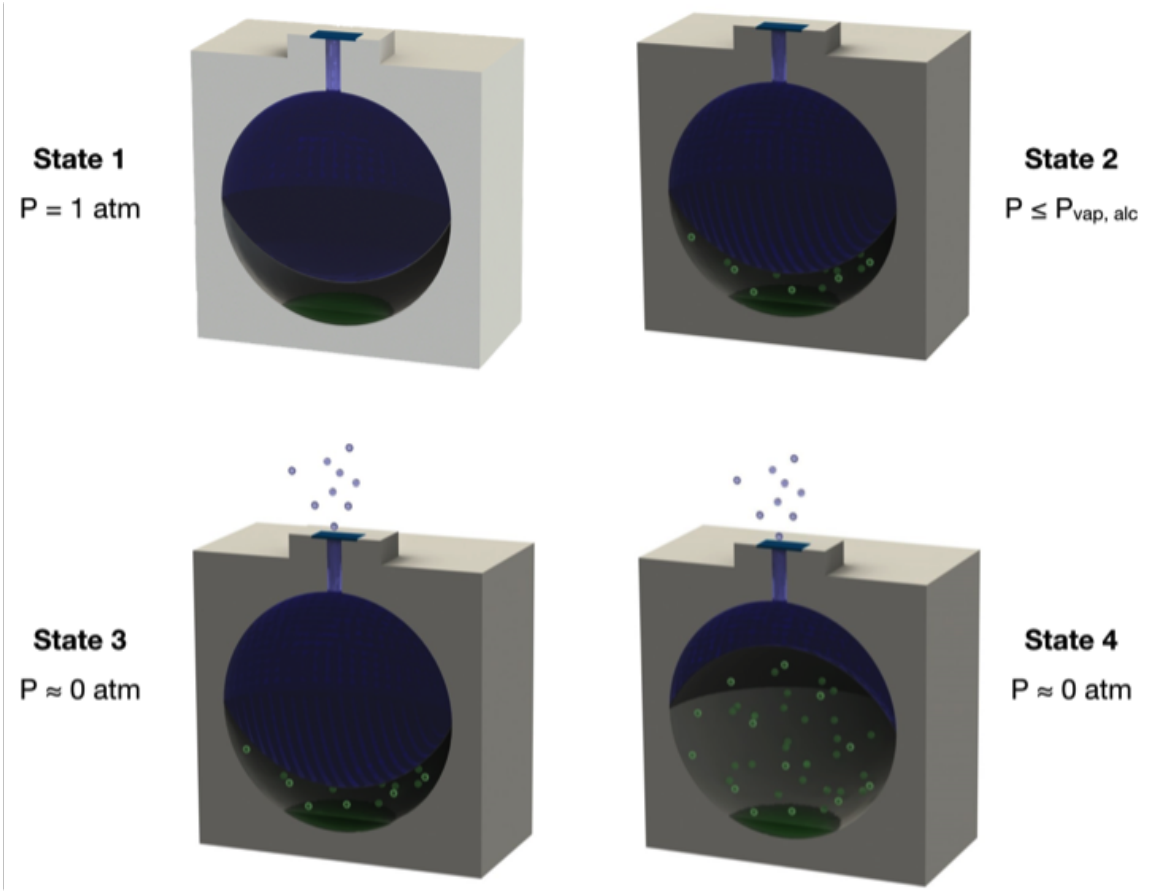

Figure 7.3.: Schematic of the zero G pressure tank

an operational attitude controller ready for implementation after new nozzles are available.

7.5 Flight Testing

The long term goal of this research is to perform a technology demonstration of FEMTA on a CubeSat flight. A proposal has been submitted for a sub-orbital flight test of the zero G propellant feed system as a preliminary test.

REFERENCES

REFERENCES

[1] Roger D. Launius. Sphere of Influence: The Sputnik Crisis and the Master Narrative. *Quest: The History of spaceflight Quarterly*, 14(4):6–19, 2007.

[2] Asif A. Siddiqi. *Deep Space Chronical: A Chronology of Deep Space and Planetary Probes 1958-2000*. Number 24. NASA, Washington, D.C., nasa/sp-20 edition, 2002.

[3] Armen Poghosyan and Alessandro Golkar. CubeSat evolution: Analyzing CubeSat capabilities for conducting science missions. *Progress in Aerospace Sciences*, 88(November 2016):59–83, 2017.

[4] J. Bouwmeester and J. Guo. Survey of worldwide pico- and nanosatellite missions, distributions and subsystem technology. *Acta Astronautica*, 67:854–862, 2010.

[5] Daniel N. Baker and S. Pete Worden. The large benefits of small-satellite missions. *Eos, Transactions, American Geophysical Union*, 89(33):301–302, aug 2008.

[6] C. Brennan Bok, Amy Comeau, Anton Dolgopolov, Tara Halt, Caroline Juang, and Phil Smith. Smallsats by the Numbers 2018. Technical report, Bryce Space and Technology, Alexandria, Virginia, 2018.

[7] Ihor Y. Gawdiak. *Astronautics and Aeronautics, 1991-1995: A Chronology*. NASA, Washington, D.C., 2000.

[8] Hank Heidt, Jordi Puig-Suari, Augustus S Moore, Shinichi Nakasuka, and Robert J Twiggs. CubeSat: A new Generation of Picosatellite for Education and Industry Low-Cost Space Experimentation. In *The 14th AIAA/USU Conference on Small Satellites*, Logan, Utah, 2000.

[9] Arash Mehrpavar, David Pignatelli, Justin Carnahan, Riki Munakata, Wenschel Lan, Armen Toorian, Amy Hutputanasin, and Simon Lee. Cubesat design specification. Technical report, California Polytechnic State University, 13.

[10] Armen Toorian, Emily Blundell, Jordi Puig-Suari, and Robert Twiggs. CubeSats as Responsive Satellites. *Space 2005*, (September):1–14, 2005.

[11] Caleb Williams, Bill Doncaster, and Jordan Shulman. 2018 Nano/Microsatellite Market Forecast. Technical report, SpaceWorks Enerprises, Inc., Atlanta, Georgia, 2018.

[12] Jim Cockrell. CubeQuest Challenge: Advanced CubeSat Techonologies for Affordable Deep Space Science and Exploration Missions, Ground Tournaments, the Moon, and Beyond. In *iCubeSat*, 2017.

[13] Kirk Woellert, Pascale Ehrenfreund, Antonio J. Ricco, and Henry Hertzfeld. Cubesats: Cost-effective science and technology platforms for emerging and developing nations. *Advances in Space Research*, 47(4):663–684, 2011.

[14] Liran Sahar, Eviatar Edlerman, Hovhannes Agalarian, Vladimir Balabanov, and Pini Gurfil. Hard Disk Drive Based Reaction Wheels for CubeSat Attitude Control. *Journal of Spacecraft and Rockets*, 55(1):1–6, 2017.

[15] Sara Spangelo and Benjamin Longmier. Optimization of CubeSat System-Level Design and Propulsion Systems for Earth-Escape Missions. *Journal of Spacecraft and Rockets*, 52(4):1009–1020, 2015.

[16] Saptarshi Bandyopadhyay, Rebecca Foust, Giri P. Subramanian, Soon-Jo Chung, and Fred Y. Hadaegh. Review of Formation Flying and Constellation Missions Using Nanosatellites. *Journal of Spacecraft and Rockets*, 53(3):567–578, 2016.

[17] Jun Asakawa, Hiroyuki Koizumi, Keita Nishii, Naoki Takeda, and Ryu Funase. Development of the Water Resistojet Propulsion System for Deep Space Exploration by the CubeSat: EQUULEUS. In *The 31st Annual AIAA/USU Conference on Small Satellites*, pages SSC17–VII–04, Logan, Utah, 2017.

[18] J B Plescia, O Barnouin, D Lawrence, B Denevi, C Ernst, and H Y Yu. The Asteroid Probe Experiment (APEX) Mission. In *The 31st AIAA/USU Conference on Small Satellites*, Logan, Utah, 2017.

[19] A Klesh and J Krajewski. MarCO: Mars Cube One – Lessons Learned from Readying the First Interplanetary Cubesats for Flight. In *49th Lunar and Planetary Science Conference 2018*, 2018.

[20] NASA. Mars InSight Launch Kit. Technical report, NASA, 2018.

[21] William H Swartz, Philip M Huang, Edward L Reynolds, Steven R Lorentz, Allan W Smith, James Briscoe, John Carvo, Blue Canyon Technologies, and Dong L Wu. RAVAN CubeSat Results: Technologies and Science Demonstrated on Orbit. In *31st AIAA/USU Conference on Small Satellites*, Logan, Utah, 2017.

[22] Mcclain Goggin, Sebastian Tamrazian, Ross Carlson, Andrew Tidwell, and Devon Parkos. CubeSat Sensor Platform for Reentry Aerothermodynamics. In *The 31st Annual AIAA/USU Conference on Small Satellites*, Logan, Utah, 2017.

[23] V Lapeyrere, S Lacour, L David, M Nowak, A Crouzier, G Schworer, P Perrot, and S Rayane. PicSat : a Cubesat mission for exoplanetary transit detection in 2017. In *The 31st AIAA/USU Conference on Small Satellites*, Logan, Utah, 2017.

[24] Brock J Lameres, Colin Delaney, Matt Johnson, Connor Julien, Kevin Zack, Ben Cunningham, Todd Kaiser, Larry Springer, and David Klumpar. Next on the Pad: RadSat – A Radiation Tolerant Computer System. In *The 31st AIAA/USU Conference on Small Satellites*, Logan, Utah, 2017.

[25] C. Clagett, L. Santos, B. Azimi, A. Cudmore, J. Marshall, S. Starin, S. Sheikh, E. Zesta, M. Paschalidis, N., Johnson, and L. Kepko. Dellingr: NASA Goddard Space Flight Center's First 6U Spacecraft. In *31st Annual AIAA/USU Conference on Small Satellites*, Logan, Utah, 2017.

[26] Isaac Netwon, A. Motte, and N. W. Chittenden. *Newton's Principia: The Mathematical Principles of Natural Philosophy: by Sir Isaac Newton; Translated into English by Andrew Motte. To Which Is Added, Newton's System of the World / with a Life of the Author by N. W. Chittenden.* Geo. P. Putnam, New York, 1850.

[27] Andrew Ketsdever, Alina Alexeenko, Michael Clabough, and Sergey Gimelshein. Experimental and Numerical Determination of Micropropulsion Device Efficiencies at Low Reynolds Numbers. *AIAA Journal*, 43(3):633–641, 2005.

[28] P. Lozano. *MEMS thrusters for nano- and pico-satellites.* Woodhead Publishing Limited, 2013.

[29] Simon Tardivel, Andrew T. Klesh, and Stefano Campagnola. Technology Enabling Interplanetary Trajectories for Nanospacecraft. *Journal of Spacecraft and Rockets*, 55(1):1–11, 2017.

[30] W. P. Wright and P. Ferrer. Electric micropropulsion systems. *Progress in Aerospace Sciences*, 74:48–61, 2015.

[31] Akshay Reddy Tummala. An Overview of Cube-Satellite Propulsion Technologies and Trends. *Aerospace*, 4(4):58, 2017.

[32] Vincent Tarantini, Ben Risi, Robert Spina, Nathan G Orr, and Robert E Zee. DEVELOPMENT OF A NITROUS OXIDE-BASED MONOPROPELLANT THRUSTER FOR SMALL SPACECRAFT. In *Small Satellites Systems and Services (4S) Symposium*, Valletta, Malta, 2016.

[33] MPS-120: Low Power, High Delta V Propulsion for CubeSats. Technical report, Aerojet Rocketdyne, 2017.

[34] MRE-0.1 Monopropellant Thruster. Technical report, Northrop Grumman Corporation.

[35] Monopropellant Thrusters. Technical report, MOOG ISP, Niagara Falls, New York, 2013.

[36] Ronald A Spores, Robert Masse, Scott Kimbrel, and Chris McLean. GPIM AF-M315E Propulsion System. *The 49th AIAA/ASME/SAE/ASEE Joint Propulsion Conference*, (July 2013):3849, 2013.

[37] BGT-X5 Green Monopropellant Thruster. Technical report, Busek Co. Inc., 2016.

[38] ArgoMoon Propulsion System. Technical report, VACCO Industries, South El Monte, California, 2017.

[39] Michael Tsay, Charlie Feng, Lenny Paritsky, Jurg Zwahlen, Derek Lafko, and Mike Robin. Complete EM System Development for Busek's 1U CubeSat Green Propulsion Module. *52nd AIAA/SAE/ASEE Joint Propulsion Conference*, pages AIAA 2016–4905, 2016.

[40] HPGP Thrusters. Technical report, ECAPS by Bradford, Solna, Sweden, 2017.

[41] Bipropellant Attitude Control System (ACS) Thrusters. Technical report, MOOG Space and Defense Group, East Aurora, New York, 2018.

[42] Kyle P Doyle and Mason A Peck. Spinning CubeSats with Liquid Propellant. In *AIAA SciTech Forum, AIAA Guidance, Navigation. and Control Conference*, number January, pages 1–17, San Diego, California, 2016. American Institute of Aeronautics and Astronautics.

[43] HYDROS -M & HYDROS -C. Technical report, Tethers Unlimited, Inc., Bothell WA, 2017.

[44] Marsil A.C. Silva, Daduí C. Guerrieri, Angelo Cervone, and Eberhard Gill. A review of MEMS micropropulsion technologies for CubeSats and PocketQubes. *Acta Astronautica*, 143(November 2017):234–243, 2018.

[45] Jennifer Hudson. Mission Analysis for CubeSats with Micropropulsion. *Journal of Spacecraft and Rockets*, 53(5):836–846, 2016.

[46] Reaction Control Propulsion Module, X13003000-01. Technical report, VACCO Industries, South El Monte, California, 2014.

[47] Grant Bonin, Niels H. Roth, Ben Risi, C. Cordell Grant, and Robert E. Zee. Flight Results from the CanX-4 and CanX-5 Formation Flying Mission. In *29th AIAA/USU Conference on Small Satellites*, Logan, Utah, 2015.

[48] Gas Gas Cold Thrusters. Technical report, MOOG Space and Defense Group, 2017.

[49] Pelle Rangsten, Håkan Johansson, Maria Bendixen, Kerstin Jonsson, Johan Bejhed, and Tor-arne Grönland. MEMS Micropropulsion Components for Small Spacecraft. *25th Annual AIAA/USU Conference on small satellites*, pages 1–12, 2011.

[50] M.S. Ivanov, G.N Markelov, and A.D. Ketsdever. Numerical Study of Cold Gas Micronozzle Flows. In *37th Aerospace Sciences Meeting & Exhibit*, Reno, Nevada, 1999. American Institue of Aeronautics and Astronautics.

[51] G. Markelov and M. Ivanov. A comparative analysis of 2D/3D micronozzle flows by the DSMC method. In *39th Aerospace Sciences Meeting and Exhibit*, Reno, NV, 2001.

[52] Sara Spangelo, Damon Landau, Shawn Johnson, Nitin Arora, and Thomas Randolph. Defining the requirements for the Micro Electric Propulsion systems for small spacecraft missions. *IEEE Aerospace Conference Proceedings*, 2015-June, 2015.

[53] Jerry A. Orr. *Powered Flight*, volume 6. 1958.

[54] Elaine M. Petro and Raymond J. Sedwick. Survey of Moderate-Power Electric Propulsion Systems. *Journal of Spacecraft and Rockets*, 54(3):529–541, 2017.

[55] John Slough and J.J Ewin. Microarcjet Microthruster for Nanosat Applications. In *43rd AIAA/ASME/ASEE Joint Propulsion Conference and Exhibit*, Cincinnati, Ohio, 2007.

[56] Ryan W. Conversano and Richard E. Wirz. Mission Capability Assessment of CubeSats Using a Miniature Ion Thruster. *Journal of Spacecraft and Rockets*, 50(5):1035–1046, 2013.

[57] Richard Wirz, Juergen Mueller, Michael Gale, and Colleen Marrese. Miniature Ion Thruster for Precision Formation Flying. In *40th AIAA/ASME/SAE/ASEE Joint Propulsion Conference and Exhibit*, Fort Lauderdale, Florida, 2004.

[58] BHT-200 Hall Thruster. Technical report, Busek Co. Inc., Natick, Massachusetts, 2015.

[59] BET-100 Busek Electrospray Thruster. Technical report, Busek Co. Inc., Natick, Massachusetts, 2016.

[60] IFM Nano Thruster Product Overview. Technical report, Enpulsion, 2018.

[61] Phase Four Radio Frequency Thruster. Technical report, Phase Four, Inc., 2017.

[62] Enric Grustan-Gutierrez and Manuel Gamero-Castaño. Microfabricated Electrospray Thruster Array with High Hydraulic Resistance Channels. *Journal of Propulsion and Power*, 33(4):984–991, 2017.

[63] Matthew S Glascock, Joshua L Rovey, Shae Williams, and Jason Thrasher. Plasma Plume Characterization of Electric Solid Propellant Pulsed Microthrusters. *The 51st AIAA/ASME/SAE/ASEE Joint Propulsion Conference & Exhibit*, 33(4):870–880, 2015.

[64] Kristina Lemmer. Propulsion for CubeSats. *Acta Astronautica*, 134(September 2016):231–243, 2017.

[65] Michael Keidar, Taisen Zhuang, Alexey Shashurin, George Teel, Dereck Chiu, Joseph Lukas, Samudra Haque, and Lubos Brieda. Electric propulsion for small satellites. *Plasma Physics and Controlled Fusion*, 57, 2015.

[66] C. Scharlemann, N. Buldrini, R. Killinger, M. Jentsch, A. Polli, L. Ceruti, L. Serafini, D. DiCara, and D. Nicolini. Qualifciation test series of the indium needle FEEP micro-propulsion system for LISA Pathfinder. *Acta Astronautica*, 69(9-10):822–832, 2011.

[67] F Trezzolani, M Manente, E Toson, A Selmo, M Magarotto, D Moretto, P De Carlo, D Melazzi, and D Pavarin. Development and Testing of a Miniature Helicon Plasma Thruster. 2017.

[68] Frederick A. Leve, Brian J. Hamilton, and Mason A. Peck. *Spacecraft momentum control systems*. Springer International Publishing and Microcosm Press., Switzerland, 2015.

[69] High Performance Attitude Control. Technical report, Blue Canyon Technologies, Boulder, Colorado.

[70] Constellation Series Reaction Wheels. Technical report, Honeywell, Phoenix, Arizona, 2017.

[71] Picosatellite Reaction Wheels (RW-0.003). Technical report, Sinclair Interplanetary, 2018.

[72] Anthony Cofer, William O ' Neill, Stephen Heister, and Alina Alexeenko. Ultracompact Microthruster for Pico/Nanosat Attitude and Thermal Control based on Film-Evaporation Effect. In *30th AIAA/USU Conference on Small Satellites*, Logan, Utah, 2016.

[73] Hans-Jurgen Butt, Karlheinz Graf, and Michael Kappl. *Physics and Chemistry of Interfaces*. WILEY-VCH Verlag GMbH&Co. KGaA, Weinheim, Germany, 2003.

[74] Anthony Cofer. *Thesis / Dissertation Acceptance FILM EVAPORATION MEMS THRUSTER ARRAY FOR MICROPROPULSION A Dissertation Submitted to the Faculty of Purdue University by Anthony G . Cofer In Partial Fulfillment of the Requirements for the Degree of Doctor of Philosophy D*. Doctorate of philosophy, Purdue University, 2015.

[75] Katherine Fowee, Steven Pugia, Ryan Clay, Matthew Fuehne, Margaret Linker, Anthony Cofer, and Alina Alexeenko. SSC17-WK-48 Quad-Thruster FEMTA Micropropulsion System for CubeSat 1-Axis Control. In *31st AIAA/USU Conference on Small Satellites*, Logan, Utah, 2017.

[76] Microsat CMG Attitude Control Array. Technical report, Honeybee Robotics.

[77] Kyriakos Christou. Droplet Generator for an Ink Jet Printer, 1978.

[78] Bette R. Janson. *Astronautics and Aeronautics, 1985: A Chronology*. NASA, Washington, D.C., 1988.

[79] Bette R. Janson and Eleanor H. Ritchie. *Astronautics and Aeronautics. 1979-1984: A Chronology*. NASA, Washington, D.C., 1989.

[80] Ihor Y. Gawdiak, Ramon J. Miro, and Sam Stueland. *Astronautics and Aeornautics, 1986-1990: A Chronology*. NASA, Washington, D.C., 1997.

[81] Michael Keidar, Samudra Haque, Taisen Zhuang, Alexey Shashurin, Dereck Chiu, George Teel, Elwood Agasid, Oriol Tintore, and Eddie Uribe. Micro-Cathode Arc Thruster for PhoneSat Propulsion. In *the 27th AIAA/USU Conference on Small Satellites*, Logan, Utah, 2013.

[82] Andres Dono, Oriol Tintore, George Teel, Nghia Mai, Joseph Lukas, Samudra Haque, Eddie Uribe, Michael Keidar, and Elwood Agasid. Modular Pulsed Plasma Electric Propulsion System for Cubesats Design & Applications. Technical report, NASA Ames Research center, 2014.

[83] MRE-1.0 Monopropellant Thruster. Technical report, Northrop Grumman Corporation.

[84] MRE-4.0 Monopropellant Thruster. Technical report, Northrop Grumman Corporation.

[85] VACCO. Lunar Flashlight Propulsion System. Technical report, VACCO Industries, South El Monte, California, 2017.

[86] NEA Scout Propulsion System. Technical report, VACCO Industries, South El Monte, California, 2017.

[87] The Vacco and Cusp Mips. CuSP Propulsion System. Technical report, VACCO Industries, South El Monte, California, 2017.

[88] Vacco ChEMS Micro Prouplsion Systems. Technical report, VACCO Industries.

[89] U Kvell, M Puusepp, F Kaminski, J-E Past, K Palmer, T-A Grönland, and M Noorma. Nanosatellite orbit control using MEMS cold gas thrusters. *Proceedings of the Estonian Academy of Sciences*, 63(2S):279, 2014.

[90] Mirko Leomanni, Andrea Garulli, Antonio Giannitrapani, and Fabrizio Scortecci. Propulsion options for very low Earth orbit microsatellites. *Acta Astronautica*, 133(November 2016):444–454, 2017.

[91] Dan Lev and Jacob Herscovitz. Carbon Dioxide Based Heated Gas Propulsion System for Nano-Satellites. 2017.

[92] Propulsion Unit for CubeSats: 11044000-01. Technical report, VACCO Industries, South El Monte, California, 2014.

[93] John Ziemer, Colleen Marrese-reading, Charley Dunn, Andrew Romero-wolf, Curt Cutler, Shahram Javidnia, Thanh Le, Irena Li, Garth Franklin, and Phil Barela. Colloid Microthruster Flight Performance Results from Space Technology 7 Disturbance Reduction System. In *International Electric Propulsion Conference*, Atlanta, Georgia, 2017.

[94] BET-1mN Busek Electrospray Thruster. Technical report, Busek Co. Inc, Natick, Massachusetts, 2016.

[95] Ciara McGrath, Malcolm Macdonald, Paulo Lozano, and David Miller. Applications of Responsive Small Satellites with MIT TILE Electrospray Propulsion. In *15th Reinventing Space Conference*, University of Strathclyde, 2017.

[96] David Krejci and Paulo Lozano. Scalable ionic liquid electrospray thrusters for nanosatellites. In *39th Annual AAS GNC Conference*, Breckenridge, Colorado, 2016.

[97] Busek Micro Resistojet. Technical report, Busek Co. Inc., Natick, Massachusetts, 2013.

[98] IFM Micro Thruster Product Overview. Technical report, Enpulsion, 2018.

[99] BHT-600 Busek Hall Effect Thruster. Technical report, Busek Co. Inc., Natick, Massachusetts, 2016.

[100] James J. Szabo, Bruce Pote, Rachel Tedrake, Surjeet Paintal, Lawrence Byrne, Vlad J. Hruby, Hani Kamhawi, and Tim Smith. High Throughput 600 Watt Hall Effect Thruster for Space Exploration. In *52nd AIAA/SAE/ASEE Joint Propulsion Conference*, Salt Lake City, Utah, 2016.

[101] BHT-1500 Busek Hall Effect Thruster. Technical report, Busek Co. Inc., Natick, Massachusetts, 2016.

[102] BHT-8000 Busek Hall Effect Thruster. Technical report, Busek Co. Inc., Natick, Massachusetts, 2016.

[103] Stephane Mazouffre and Lou Grimaud. Characteristics and Performances of a 100-W Hall Thruster for Microspacecraft. *IEEE Transactions on Plasma Science*, 46(2):330–337, 2018.

[104] R Wirz, J Polk, C Marrese, and J Mueller. Experimental and computational investigation of the performance of a micro-ion thruster. *38th AIAA Joint Propulsion Conference*, (AIAA-2002-3835), 2002.

[105] Hiroyuki Koizumi, Kimiya Komurasaki, Junichi Aoyama, and Koji Yamaguchi. Development and Flight Operation of a Miniature Ion Propulsion System. *Journal of Propulsion and Power*, 2017.

[106] J. E. Polk, R. Y. Kakuda, J. R. Anderson, J. R. Brophy, V. K. Rawlin, M. J. Patterson, J. Sovey, and J. Hamley. Validation of the NSTAR ion propulsion system on the Deep Space One mission - Overview and initial results. In *35th Joint Propulsion Conference and Exhibit*, Pasadena, California, 1999.

[107] BmP-220 Micro-Pulsed Plasma Thruster. Technical report, Busek Co. Inc., Natick, Massachusetts, 2016.

[108] M Umair Siddiqui. Updated Performance Measurements of the Phase Four RF Thruster. *34th Space Symposium*, (April):1–7, 2018.

[109] BIT-3: RF Ion Thruster. Technical report, Busek Co. Inc., Natick, Massachusetts, 2018.

[110] Hans Leiter, Benjamin Lotz, Davar Feili, Michaeil Tartz, Horst Neumann, and Davina Maria Di Cara. Design Development and Test of the RIT-μX Mini Ion Engine System. In *31st International Electric Propulsion Conference*, Anne Arbor, Michigan, 2009.

[111] Microsatellite Reaction Wheels (RW3-1.0). Technical report, Sinclair Interplanetary, 2017.

[112] Microsatellite Reaction Wheels (-0.060-). Technical report, Sinclair Interplanetary, 2016.

[113] Nanosatellite Reaction Wheels (RW-0.03-4). Technical report, Sinclair Interplanetary, 2016.

[114] Picosatellite Reaction Wheels (RW-0.01). Technical report, Sinclair Interplanetary, 2016.

[115] Control Momentum Gyroscope solution for small satellites. Technical report, Airbus Defense and Space, 2014.

[116] A compact , cost-effective , high performance Control Momentum Gyroscope solution for the mini satellites widens the CMG family proposed by AIRBUS DS. Technical report, Airbus Defense and Space, 2014.

APPENDICES

A. Chronology of Deep Space Exploration Mission and Major Scientific Satellites Launched: 1957-2000

This table was used to outline the historical trend of increasing satellite size to create catch all missions that met man objectives. Data is taken from NASA records [2] [7] [78] [79] [80].

Table A.1.: Deep Space Probes and Scientific Satellites launched, with recorded mass: 1957-2000

Name	**Mass**	**Year**
Sputnik	83.6	1957
Pioneer 1	38.3	1958
Pioneer 2	39.6	1958
Pioneer 3	5.87	1958
Cosmic Rocket	361.3	1959
Pioneer 4	6.1	1959
Luna 2	390.2	1959
Luna 3	278.5	1959
Pioneer 5	43.2	1960
venera	643.5	1961
Ranger 3	330	1962
Mariner 2	203.6	1962
Mars 1	893.5	1962
Luna 4	1422	1963
ranger 6	364.69	1964

Name	Mass	Year
Zond 1	948	1964
Ranger 7	365.5	1964
Mariner 4	260.8	1964
Zond 2	996	1964
Ranger 8	366.87	1965
Ranger 9	366.87	1965
Luna 5	1476	1965
Zond 3	950	1965
Luna 7	1506	1965
Venera 2	963	1965
Luna 8	1552	1965
Pioneer 6	62.14	1965
Luna 9	1538	1966
Luna 10	1582	1966
Surveyor 1	995.2	1966
Explorer 33	93.4	1966
Lunar Orbiter 1	385.6	1966
Pioneer 7	62.75	1966
Luna 11	1640	1966
Surveyor 2	995.2	1966
Lunar Orbiter 2	385.6	1966
Luna 13	1620	1966
Lunar Orbiter 3	385.6	1967
Surveyor 3	997.9	1967
Lunar Orbiter 4	385.6	1967
venera 4	1106	1967
Mariner 5	244.9	1967
Surveyor 4	1037.4	1967

Name	Mass	Year
Explorer 35	104.3	1967
Lunar Orbiter 5	385.6	1967
Surveyor 5	1006	1967
Surveryor 6	1008.3	1967
Pioneer 8	65.36	1967
Surveryor 7	1040.1	1968
Pioneer 9	65.36	1968
Venera 5	1130	1969
Venera 6	1130	1969
Mariner 6	381	1969
Mariner 7	381	1969
Zond 7	5375	1969
Venera 7	1180	1970
Luna 16	5727	1970
Zond 8	5375	1970
Luna 17	5700	1970
Mars 2	4650	1971
Mars 3	4650	1971
Mariner 9	997.9	1971
Apollo 15 Particle and Fields Subsatellite	35.6	1971
Luna 18	5750	1971
Luna 19	5700	1971
Luna 20	5750	1972
Pioneer 10	258	1972
Venera 8	1184	1972
Apollo 16 Particle and Fields Subsatellite	42	1972

Name	Mass	Year
Luna 21	5950	1973
Pioneer 11	258.5	1973
Explorer 49	330.2	1973
Mars 4	3440	1973
Mars 5	3440	1973
Mars 6	3260	1973
Mars 7	3260	1973
Mariner 10	502.9	1973
Luna 22	5700	1974
Luna 23	5800	1974
Helios 1	370	1974
Venera 9	4936	1975
Venera 10	5033	1975
Viking 1	3527	1975
Viking 2	3527	1975
Helios 2	370	1976
Luna 24	5800	1976
Voyager 2	2080	1977
Voyager 1	2080	1977
Pioneer Venus 1	582	1978
Pioneer Venus 2	904	1978
ISEE-3	479	1978
Venera 11	4450	1978
Venera 12	4461	1978
SCATHA	360	1979
SAGE	147	1979
Ariel 6	154	1979
NOAA6	723	1979

Name	Mass	Year
HEAO	3150	1979
Magsat	181	1979
SMM	2315	1980
Venera 13	4363	1981
Venera 14	4363.5	1981
GOES 5	400	1981
Rohini	40	1981
NOAA 7	723	1981
Dyanmics Explorer 1	403	1981
Dynamics Explorer 2	415	1981
Solar Mesosphere Explorer	437	1981
UOSAT	50	1981
Landsat 4	2000	1982
Venera 15	5250	1983
Venera 16	5300	1983
IRAS	1000	1983
NOAA8	2000	1983
Vega 1	4920	1984
Vega 2	4920	1984
Landsat	2000	1984
LDEF	9707	1984
Ampte 1	242	1984
Ampte 2	605	1984
Ampte 3	77	1984
NOAA 9	1700	1984
Sakigake	138.1	1985
Suisei	139.5	1985
GEOSAT	635	1985

Name	Mass	Year
Spartan 1	1008	1985
Giotto	960	1985
Plasma Diagnostics Package	160	1985
NOAA 10	1712	1986
NOAA11	1038	1987
Fobos 1	6220	1988
Fobos 2	6220	1988
COBE	2206	1989
Magellan	3445	1989
Hubble Space Telescope	11355.4	1990
ROSAT	2424	1990
CRRES	3842	1990
Galileo	2561	1989
Hiten/ Hagomoro	197.4	1990
Ulysses	371	1990
Gamma Ray Observatory	15876	1991
NOAA12	735	1991
Radiation Experiment	85.3	1991
Microsat-1	22.2	1991
Microsat-2	22.2	1991
Microsat-3	22.2	1991
Microsat-4	22.2	1991
Microsat-5	22.2	1991
Microsat-6	22.2	1991
Microsat-7	22.2	1991
Eureka -1	4491	1992
Mars Observer	2573	1992

Name	**Mass**	**Year**
SEDS I	38.5	1993
Clementine	424	1994
Wind	1250	1994
BREMAST	63	1994
SEDS II	23	1994
ARPASAT	181	1994
SOHO	1864	1995
NEAR	805	1996
Mars Global Surveyor	1062.1	1996
Mars 8	6200	1996
Mars Pathfinder	870	1996
ACE	752	1997
Cassini/ Huygens	5655	1997
Asiasat 3	3465	1997
Lunar Prospector	300	1998
Nozomi	536	1998
Deep Space 1	489	1998
Mars Climate Orbiter	629	1998
Mars Polar Lander/ Deep Space 2	583	1999
Stardust	385	1999

B. Micropropulsion Survey: Operational Specifications I

The micropropulsion technologies were listed if they had gone through experimental testing in relevant environments. This is not meant to be an exhaustive list but rather a detailed survey of available technologies being studied.

This table includes

- Device name
- Company or university
- Device type
- Propellant
- Reported thrust
- Reported power
- Reported specific impulse

Table B.1.: Micropropulsion Operational Specifications I

Thruster	**Entity**	**Type**	**Propellant**	**Thrust**	**Power (W)**	**Isp (sec)**	**Source**
Micro Arcjet	University of Washington	Arcjet	Argon	1.1-1.8mN	5	90	[55]
μCAT	George Washington University	Cathode Arc Thruster	Titanium	50μN	5	3000	[81] [82]
MPS-120	Aerojet Rocketdyne	Chemical	Hydrazine	0.25-2.8 N	10	217	[33]
Hydros-M	Tethers Unlimited	Chemical	Water	1.2 N	40	310	[43]
Hdros-C	Tethers Unlimited	Chemical	Water	1.5N	25	310	[43]
MRE-0.1	Northrop Grumman	Chemical	Hydrazine	0.8-1.0N	15	216	[83]
MRE-1.0	Northrop Grumman	Chemical	Hydrazine	5.0-3.4N	15	218	[34]

Thruster	Entity	Type	Propellant	Thrust	Power (W)	Isp (sec)	Source
MRE-4.0	Northrop Grumman	Chemical	Hydrazine	9.8-18N	30	217	[84]
Nitrous Oxide Monopropellant Thruster	University of Toronto Institute for Aerospace Studies	Chemical	Nitrous Oxide	100mN	30	131	[32]
MONARC-1	Moog	Chemical	Hydrazine	1N	18	228	[35]
MONARC-5	Moog	Chemical	Hydrazine	4.5N	18	226	[35]
DST-11H	Moog	Chemical	Hydrazine/ MON	22N	41	310	[41]
DST-12	Moog	Chemical	MMH/MON	22N	9	302	[41]
DST-13	Moog	Chemical	MMH/MON	22N	41	298	[41]
5lbf	Moog	Chemical	MMH/MON	22N	15.6	292	[41]
BGT-X5	Busek Co. Inc.	Green	AF-M315E	500 mN	20	220-225	[37]

Thruster	Entity	Type	Propellant	Thrust	Power (W)	Isp (sec)	Source
MiPS (X16029000-01)	VACCO	Green	LMP-103S/ AF-M315E	100mN	15	169.4	[85]
GR-1 (GPIM)	Aerojet Rocketdyne	Green	AF-M315E	0.26-1.42N	8.3	231	[36]
AMAC	Busek	Green	AF-M315E	0.1-0.5N	20	220	[39]
100 mN HPGP	ECAPS	Green	LMP-103S	30-100mN	8	196-209	[40]
1N HPGP	ECAPS	Green	LMP-103S	0.25-1.0N	10	204-231	[40]
1N GP	ECAPS	Green	LMP-103S/LT	0.25-1mN	19	194-227	[40]
5N HPGP	ECAPS	Green	LMP-103S	1.5-5.5N	25	239-253	[40]
22N HPGP	ECAPS	Green	LMP-103S	5.5-22N	50	243-255	[40]
0.5N HPGP	ECAPS	Green	LMP-103S	0.25-0.5N	10	178-219	[40]
NEA Scout (X16056000)	VACCO	Cold Gas	R236fa	25mN	55		[86]

Thruster	Entity	Type	Propellant	Thrust	Power (W)	Isp (sec)	Source
CuSp (X16038000-01)	VACCO	Cold Gas	R-134a/ R-236fa	25mN			[87]
Reaction Control (X13003000-01)	VACOO	Cold Gas	R134a	25mN	5	40	[46]
End-Mounted Standard (X14029003-1X)	VACCO	Cold Gas	R134a	10mN	10W	40	[88]
CNAPS	University of Toronto Institute for Aerospace Studies	Cold Gas	Sulfur Hexafluoride	12.5-50mN		45	[47]
POPSAT-HIP1	μspace Rapid	Cold Gas	Argon	1mN			[31]
MEMS Cold Gas	GOMSpace	Cold Gas	Methane	1mN			[31]
MEMS Cold Gas Thruster	Tartu Observatory	Cold Gas	Butane	1mN	2		[89]

Thruster	Entity	Type	Propellant	Thrust	Power (W)	Isp (sec)	Source
Moog 240mN	Moog	Cold Gas	Nitrogen	10-40 mN	10	60	[48]
Moog 360mN	Moog	Cold Gas	Nitrogen	120mN	35	57	[48]
Moog 3.6N	Moog	Cold Gas	Nitrogen	3.6N	30	65	[48]
Micro Thruster	Marotta	Cold Gas	Nitrogen	50-2360	1	65	[90]
SAMSON Thruster	Israel Institute of Technology	Cold Gas	Carbon Dioxide	80mN		67	[91]
MEMS Cold Gas Thruster	NanoSpace	Cold Gas	Nitorgen	0.01mN-1mN	3	50-100	[49]
SNAP 1	SSTL	Cold Gas	Butane	50mN		43	[31]
Moog 360mN	Moog	Cold Gas	Nitrogen	120mN	10.5	65	[48]
ArgoMoon (X17025000)	VACCO	green	LMP-103S	100mN	20		[38]
		Cold Gas	R134a	25mN			

Thruster	**Entity**	**Type**	**Propellant**	**Thrust**	**Power (W)**	**Isp (sec)**	**Source**
PUC (11044000-01)	VACCO	warm gas	Sulfur Dioxide	5.4N	15 15 15	70	[92] [88]
CMTA	Busek	Colloid		5-30 μN			[93]
BET-1mN	Busek	Electrospray	Ionic Liquid	0.7 mN	15	800	[94]
BET-100	Busek	Electrospray	Ionic Liquid	5-100 μN	15	1000-1800	[59]
TILE	Busek	Electrospray	EMI-BF4	350μN	10	1150	[95] [96]
MEP	Jet Propulsion Laboratory	Electrospray	Indium	0.2mN	8.16	3744	[45]
Micro Resistojet	Busek	Electrothermal	Ammonia	0.5 mN	15	80	[97]
IFM Nano Thruster	Enpulsion	FEEP	Indium	10-500 μN	40	2000-5000	[60]

Thruster	**Entity**	**Type**	**Propellant**	**Thrust**	**Power (W)**	**Isp (sec)**	**Source**
IFM Micro Thruster	Enpulsion	FEEP	Indium	300-1000 μN	400	2000-5000	[98]
FEEP System	University of Applied Science Wiener Neustadt	FEEP	Indium	0.03mN-0.1mN	8	3000-6000	[66]
BHT-200	Busek	Hall	Xenon Iodine Krypton	13mN	20	1375	[58]
BHT-600	Busek	Hall	Xenon Iodine Krypton	39mN	600	1500	[99] [100]
BHT-1500	Busek	Hall	Xenon Iodine Krypton	58-179mN	2700	1615-2035	[101]

Thruster	**Entity**	**Type**	**Propellant**	**Thrust**	**Power (W)**	**Isp (sec)**	**Source**
BHT-8000	Busek	Hall	Xenon Iodine Krypton	449-325mN	10000	2210-3060	[102]
ISCT100	ICARE, CNES	Hall	Xenon	9mN	180	1300	[103]
MHT	CISAS, T4i	Helicon	Xenon	0.82mN	70	850	[67]
Hybrid MiPS	VACCO	Hybrid	Butane	0.1N	13.6	200	[88]
MiXI	California Technical Institute	Ion	Xenon	1.5mN	30	1700-3200	[56] [57] [104]

Thruster	**Entity**	**Type**	**Propellant**	**Thrust**	**Power (W)**	**Isp (sec)**	**Source**
MIPS	University of Tokyo	Ion	Xenon	220μN	28.1	790	[105]
				260μN	29.8	700	
				288μN	34	1030	
				361μN	36.5	1120	
NSTAR	Jet Propulsion Laboratory	Ion	Xenon	20.7 mN	492		[106]
				24.2mN	626		
				27.0mN	737		
				31.5mN	860		
				36.6mN	984		
CubeSat Pulsed Plasma Thruster	Clyde Space	Pulsed Plasma	Teflon	0.038mN	0.5	590	[45]
μ-PPT	Dawgstar	Pulsed Plasma	Teflon	0.14mN	12.5	500	[45]

Thruster	**Entity**	**Type**	**Propellant**	**Thrust**	**Power (W)**	**Isp (sec)**	**Source**
BmP-220	Busek	pulsed plasma	PTFE		7.5	536	[107]
AQUARIUS	University of Tokyo	Resistojet	Water	4mN	20	70	[17]
RFT	Phase Four	RF	Xenon	1-15 mN	100	500-1000	[61] [108]
BIT-3 RF	Busek	RF	Iodine	0.66-1.24mN	80	2300	[109]
RIT-μX	Giessen University	RF	Xenon	200-500μN	30	2609	[30] [110]

C. Micropropulsion Survey: Operational Specifications II

The micropropulsion technologies were listed if they had gone through experimental testing in relevant environments. This is not meant to be an exhaustive list but rather a detailed survey of available technologies being studied.

This table includes

- Device name
- Device type
- Reported impulse bit
- Reported total impulse
- Reported voltage
- Reported mass
- Reported dimensions

Table C.1.: Micropropulsion Operational Specifications II

Thruster	**Type**	**Impulse Bit**	**Total Impulse (Ns)**	**Voltage (V)**	**Mass (kg)**	**Size**	**Source**
Micro Arcjet	Arcjet			280			[55]
μCAT	Cathode Arc Thruster				0.2	200cm^3	[81] [82]
MPS-120	Chemical	0.4 mNs	775	8	1.48	1U	[33]
Hydros-M	Chemical		18023		12.6	381 mm x 191 mm	[43]
Hdros-C	Chemical	1.75Ns	2151		1.76	1U	[43]
MRE-0.1	Chemical			28	0.5	11.4cm x 17.5cm	[83]
MRE-1.0	Chemical			28	0.5	11.4cm x 18.8cm	[34]
MRE-4.0	Chemical			28	0.5	6.1cm x 20.6cm	[84]

Thruster	Type	Impulse Bit	Total Impulse (Ns)	Voltage (V)	Mass (kg)	Size	Source
Nitrous Oxide Monopropellant Thruster	Chemical			28			[32]
MONARC-1	Chemical	2.6mN	111250		0.38		[35]
MONARC-5	Chemical	3.1mNs	613852		0.49		[35]
DST-11H	Chemical				0.77		[41]
DST-12	Chemical				0.64		[41]
DST-13	Chemical				0.68		[41]
5lbf	Chemical				0.91		[41]
BGT-X5	Green	0.05Ns	565	16	1.5	1U	[37]
MiPS (X16029000-01)	Green		3320		5	3U	[85]
GR-1 (GPIM)	Green	50 mNs		28			[36]
GR-22	Green			28			[36]

Thruster	Type	Impulse Bit	Total Impulse (Ns)	Voltage (V)	Mass (kg)	Size	Source
MiPS (X16029000-01)	Green		3320		5	3U	[85]
AMAC	Green	50mNs	565		1.5		[39]
100 mN HPGP Thruster	Green	5mNs		10	0.04	5.5cm	[40]
1N HPGP Thruster	Green	70mNs		28	0.38	17.8cm	[40]
1N GP Thruster	Green	70mNs		28	0.38	17.8cm	[40]
5N HPGP Thruster	Green	0.1Ns		28	0.48	22.1cm	[40]
22N HPGP Thruster	Green	0.44Ns		28	1.1	26cm	[40]
0.5N HPGP Thruster	Green	35mNs		28	0.18	15.5cm	[40]

Thruster	Type	Impulse Bit	Total Impulse (Ns)	Voltage (V)	Mass (kg)	Size	Source
MiPS (X16029000-01)	Green		3320		5	3U	[85]
NEA Scout (X16056000)	Cold Gas		500		2.54	2U	[86]
CuSp (X16038000-01)	Cold Gas		69		0.69	0.3U	[87]
Reaction Control (X13003000-01)	Cold Gas		186		1.244	1U	[46]
End-Mpunted Standard (X14029003-1X)	Cold Gas		93	9V	0.676	0.25U	[88]
CNAPS	Cold Gas	7.5 mNs					[47]
POPSAT-HIP1	Cold Gas				3.3	3U	[31]
MEMS Cold Gas	Cold Gas					3U	[31]

Thruster	Type	Impulse Bit	Total Impulse (Ns)	Voltage (V)	Mass (kg)	Size	Source
Moog 240mN	Cold Gas			28	0.04	1.4cm x 5.7cm	[48]
Moog 360mN	Cold Gas			29	0.04	1.4cm x 2.3cm	[48]
Moog 3.6N	Cold Gas			29	0.023	0.06cm x 2.5cm	[48]
Micro Thruster	Cold Gas	44mNs			0.07		[90]
SAMSON Thruster	Cold Gas				1.78	20.75cm	[91]
MEMS Cold Gas Thruster	Cold Gas				0.115	4.4cm x 5.1cm	[49]
Moog 360mN	Cold Gas			34		1.9cm x 4.1cm	[48]

Thruster	Type	Impulse Bit	Total Impulse (Ns)	Voltage (V)	Mass (kg)	Size	Source
ArgoMoon (X17025000)	Green Cold Gas		783 72		2.065	1.3U	[38]
PUC (11044000-01)	warm gas		183 320 595		434 568 835	0.25U 0.5U 1U	[92] [88]
CMTA	Colloid		245				[93]
BET-1mN	Electrospray		605	12.6	1.15	1U - 8.5 x 8.5 x 6 cm	[94]
BET-100	Electrospray		175	11.5	0.550	1/2 U	[59]
TILE	Electrospray		400	5.5	0.450	0.5U	[95] [96]
MEP	Electrospray				0.16	140cm^3	[45]
Micro Resistojet	Electrothermal			5	1.25	9cm x 9cm x 10cm	[97]

Thruster	**Type**	**Impulse Bit**	**Total Impulse (Ns)**	**Voltage (V)**	**Mass (kg)**	**Size**	**Source**
IFM Nano Thruster	FEEP		5000	12	0.870	9.4cm x 9.0cm x 7.8cm	[60]
IFM Micro Thruster	FEEP		150000	28	8	20.0 cm x 20.0 cmx 8.0 cm	[98]
FEEP System	FEEP		1260	8000		700cm^3	[66]
BHT-200	Hall			250	1	10cm dia. 11 cm height	[58]
BHT-600	Hall			400	2.6	13 cm x 13 cm x 10cm	[99] [100]
BHT-1500	Hall				6.8		[101]
BHT-8000	Hall			800	25		[102]
ISCT100	Hall			300			[103]

Thruster	**Type**	**Impulse Bit**	**Total Impulse (Ns)**	**Voltage (V)**	**Mass (kg)**	**Size**	**Source**
MHT	Helicon				0.4	12.0cm x 15.7cm	[67]
Hybrid AND MiPS	Hybrid		1036		1.62	1U	[88]
MiXI	Ion			1126			[56] [57] [104]
MIPS	Ion				8.10	34cm x 26cm x 6cm	[105]
CubeSat Pulsed Plasma Thruster	Pulsed Plasma	38μNs	42		0.2	1/3 U	[45]

Thruster	**Type**	**Impulse Bit**	**Total Impulse (Ns)**	**Voltage (V)**	**Mass (kg)**	**Size**	**Source**
μ-PPT	Pulsed Plasma				3.8	5300cm^3	[45]
BmP-220	pulsed plasma	0.02 mNs	220	16	0.5	310cm^3	[107]
AQUARIUS	Resistojet				1.8	2U	[17]
RFT	RF				2	1U	[61], [108]
BIT-3 RF	RF			28	3	18.0 cm x 8.8 x 10.2 cm	[109]
RIT-μX	RF				0.210	2.5cm	[30] [110]

D. Reaction Wheel Survey: Operational Specifications

This table lists commercially available reaction wheels. This is not meant to be an exhaustive list but rather a detailed survey of commercially available devices.

This table includes

- Device name
- Company
- Reported momentum
- Reported maximum torque
- Reported power
- Reported voltage
- Reported mass
- Reported dimensions

Table D.1.: Reaction Wheel Operational Specifications

Name	**Company**	**Momentum (Nms)**	**Max Torque (Nm)**	**Power (W)**	**Voltage (V)**	**Mass (kg)**	**Volume (cm)**	**Source**
MicroWheel	Blue Canyon	0.015	0.004	5.5	12	0.13	4.3x4.3x1.8	[69]
RWP050	Blue Canyon	0.05	0.007	9	12	0.24	5.8x5.8x2.5	[69]
RWP100	Blue Canyon	0.1	0.007	9	12	0.35	7.0x7.0x2.5	[69]
RSP500	Blue Canyon	0.5	0.025	23	28	0.75	10.8x10.8x3.8	[69]
RW1	Blue Canyon	1.5	0.04	48	28	1.6	15x15x6.5	[69]
RW4	Blue Canyon	4	0.1	75	28	2.5	17x17x7	[69]
RW8	Blue Canyon	8	0.1	75	28	3.6	19x19x9	[69]
HR10	Honeywell	12	0.15	135	70	5.36	13.5x26.9	[70]
HR12	Honeywell	50	0.3	135	70	9.5	15.9x31.6	[70]
HR14	Honeywell	75	0.3	135	70	10.6	16.6x42.0	[70]
HR16	Honeywell	100	0.3	135	70	12	16.6x42.0	[70]
HR18	Honeywell	250	0.3	135	70	20	18.3x49.0	[70]
RW3-1.0	Sinclair	1	1	50	34	0.97	15x14x4.2	[111]

Name	Company	Momentum (Nms)	Max Torque (Nm)	Power (W)	Voltage (V)	Mass (kg)	Volume (cm)	Source
RW3-0.60	Sinclair	0.18	0.12	23.4	50	0.226	7.7x6.5x3.8	[112]
RW-0.03	Sinclair	0.04	0.02	1.8	8	0.185	5.0x5.0x4.0	[113]
RW-0.01	Sinclair	0.018	0.01	1.05	8	0.12	5.0x5.0x3.0	[114]
RW-0.003	Sinclair	0.005	0.001		9	.05	3.35x3.35x1.7	[71]

E. Control Momentum Gyroscope Survey: Operational Specifications

This table lists commercially available reaction wheels. This is not meant to be an exhaustive list but rather a detailed survey of commercially available devices.

This table includes

- Device name
- Company
- Reported momentum
- Reported maximum torque
- Reported power
- Reported angle range
- Reported angle resolution
- Reported mass
- Reported dimensions

Table E.1.: Control Momentum Gyroscope Operational Specifications

Name	**Company**	**Momentum (Nms)**	**Torque (Nm)**	**Power (W)**	**Angle Range**	**Angle Resolution (mrad)**	**Mass**	**Volume (cm^3)**	**source**
15-45S	Airbus	15	45	25	unlimited	10	18.4	33989	[115]
4-6S	Airbus	4	6	64	unlimited	10	13	22927	[116]
Microsat CMG	Honeybee Robotics	0.056	0.112	2			0.6	827.8	[76]

F. FEMTA 1U Model Experiment Set-Up and Methods

1. Prepare Thrust Cells
   (a) Thrust cell clean
      i. Disassemble the Thrust cells. Place tanks in a large beaker. Place the screws, cover plates, o-rings, and valves in a beaker. Separate and organize nozzles.
      ii. At a solvent hood, rinse the inside of the thrust cell and the outside with acetone taking care to avoid the wires.
      iii. Follow this with an identical process using isopropyl alcohol.
      iv. Rinse thoroughly with water.
      v. Rough dry the tanks with nitrogen gun and dry with clean room wipes. Place back in clean beaker.
   (b) Nozzle clean
      i. Check the nozzles for clogs/debris. Cleaning is needed if there are visible blockages
      ii. Place a nozzle and acetone into a small beaker, place in the ultrasonic cleaner for 30 seconds. Do not run for longer than 30 seconds.
      iii. Clean with Methanol, IPA and water. Dry with Nitrogen gun.
      iv. Check for clogs/debris. If still clogged use nanostrip for 10 minutes. Rinse with water and dry with nitrogen gun.
      v. Activate the nozzles (make hydrophobic) with a quick 10 second dip in BOE. Rinse with water and dry with nitrogen gun.
      vi. Check for clogs/debris

(c) Assembly

i. Check that everything is dry.

ii. Place the o-ring in the socket first. Ensure the pins move freely.

iii. Place the FEMTA nozzle on the pins and ensure contact.

iv. Move the fairing into position above the socket and tighten the screw and its diagonal screw just until contact is made.

v. Check that there is good contact with a DMM.

vi. If there is not good contact, continue to adjust the nozzle until good contact is made.

vii. If there is good contact, tighten down the other two screws. Do not force the screws all the way down. Tighten until there is resistance.

viii. Repeat on other sockets and tanks.

ix. Attach the pressure relief valves.

x. Once completed, wrap in foil to protect from contamination.

2. CubeSat preparation

(a) Pi-0 set up

i. Ensure the cubesat is plugged into a powersource.

ii. Connect to the CubeSat Pi and run gitpull in the FEMTA folder if there are any new changes from git hub

iii. Reboot the pi

iv. Connect to the pi

v. Type sudo nano /etc/network/interfaces. Uncomment the section for the internet connection. Close and save, then shutdown the pi. Remove from power source.

vi. Make sure batteries are not plugged into the driver board. Plug the pi into the board. Connect the batteries to the board.

vii. Connect to the pi from the chamber pi on the lab computer.

viii. Run ./rerun.sh on the satellite pi. Open the valve. Check that the valve opens and allows air to pass. Close the valve. Test that there are no leaks in the plumbing system.

ix. Shutdown the pi. Unplug the batteries.

(b) Thrust cell test prep

i. In the clean box, boil the ultra pure water to de-gas the water.

ii. Let cool

iii. Check and record the resistance of all four nozzles and record

iv. Record the dry mass of both thrust cells

v. Fill the tanks with water using the bovine syringe.

vi. Insert the valve (with PTFE thread seal tape).

vii. Record the wet mass of the thrust cells.

viii. Remove the thrust cells from the clean box. Label the nozzles.

ix. Remove the Check for leaks with the manometer. Water should only pass through the nozzles.

x. Run ./rerun.sh on the satellite pi. Open the valve. Check that the valve opens and allows air to pass. Close the valve. Test that there are no leaks in the plumbing system.

(c) CubeSat integration

i. Attach the thrust cells to the side rails with screws.

ii. Plug in the 6 pin connectors for the thrust cells to the connections on the circuit board.

iii. Reattach the side rails with thrusters. Not all screws insert properly, ensure there is a screw on the top and bottom plate for each rail.

iv. Insert batteries into their side rails. Reattach the battery siderails.

v. Reconnect batteries to the board.

vi. Connect to the pi -0 from the chamber pi with the lab computer

vii. Attach the harness and the spring.

viii. Hang the cubesat from the hook in the vacuum chamber with the harness. Check that the cubesat is level.

ix. Begin tmux session

x. Begin ./rerun.sh

xi. Pump down can begin

3. Post test procedure

(a) Before pump up is complete

i. Stop ./rerun.sh

ii. Change the file sudo nano /etc/network/interfaces by commenting out the section about wifi connection.

iii. Exit and save.

iv. Shutdown the pi

(b) Data retrieval

i. Disconnect batteries from the board. Remove the thrust cells and the batteries. Leave two rails connected.

ii. Remove the Pi from the board.

iii. Plug the pi into the monitor and power and keyboard.

iv. Run ifconfig to find the ip address of the pi

v. DO NOT connect to the pi from laptop. Run scp kate@10.186.126.183: ∼/FEMTA/spacebound/satellite-control/logs/* ∼/Downloads/ but with the new ip address

vi. Shutdown the pi. Remove from power, monitor, and keyboard. Place back on the board.

(c) CubeSat disassembly

i. Weigh the thrust cells. Record final mass.

ii. Plug the satellite in if requested, otherwise place back in the box.

iii. Recharge the batteries.

iv. Write up the experiment for the log.

v. Post process data

G. High Vacuum Laboratory Equipment

The High Vacuum Facility is located within the Aeroscpace Sciences Laboratories at Purdue University. The Faculty advisor for the High Vacuum Facility is Prof. Alina Alexeenko and the laboratory manager is Dr. Tony Cofer.

G.1 Small Vacuum Chamber

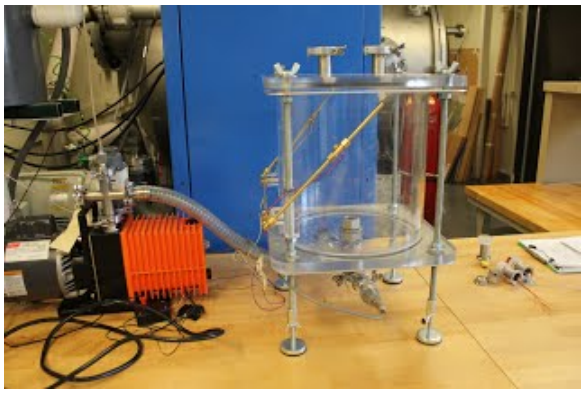

Figure G.1.: Small chamber with the Alcatel 2008A rotary vane pump.

The small vacuum chamber (figure G.1) is a 1 foot diameter and 1 foot tall cylindrical vacuum chamber made of acrylic and serviced by an Alcatel 2008A two-stage rotary vane pump. The small vacuum chamber can attain a minimum pressure of 5 milliTorr. The small chamber is primarily used to test equipment prior to large vacuum experiments, as the pump achieves the desired pressure drop in less than a minute.

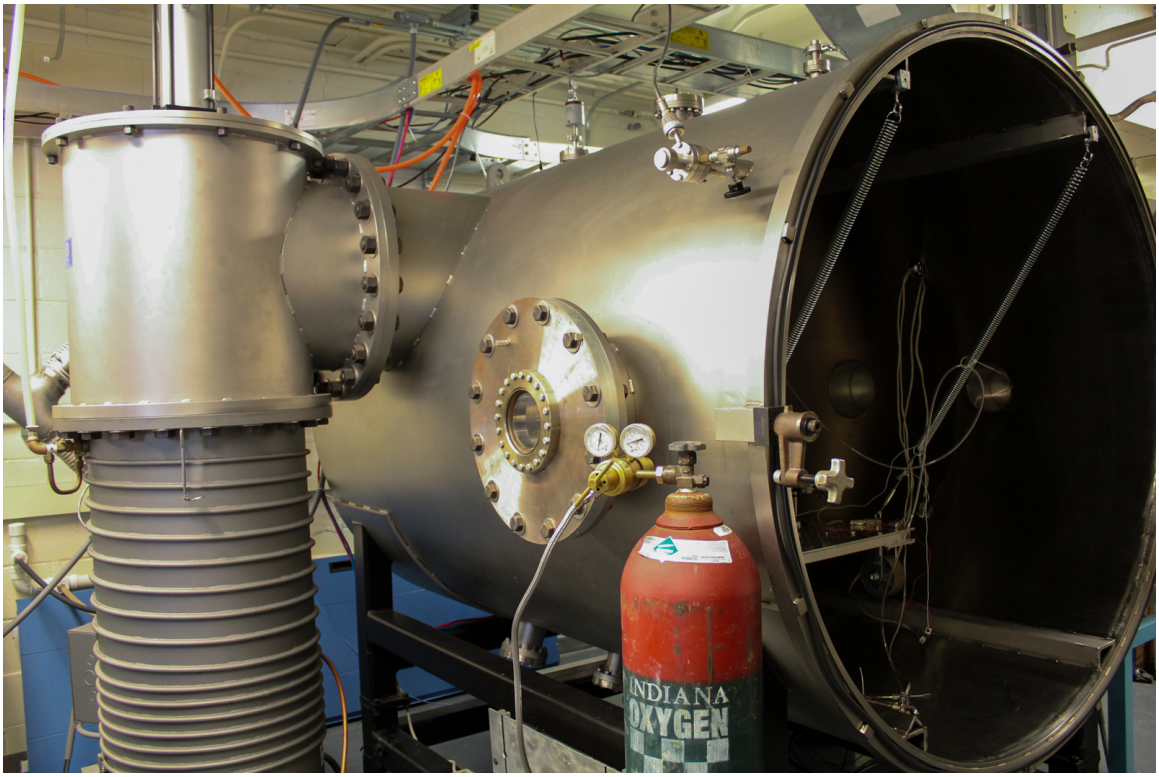

Figure G.2.: Large Vacuum chamber and diffusion pump.

G.2 Large Vacuum Chamber

The large vacuum chamber is a 5 foot diameter, 7 foot long cylinder of cast aluminum (shown in figure G.2). The 4.2 cubic meter volume is evacuated by a a two-stage positive displacement pump and a blower to reach approximately 1 millitorr. A Varian HS-20 diffusion pump further evacuates the chamber to high vacuum (1 microTorr). The pumps, blower, and plumbing are shown in figure G.3.

G.3 MicroNewton Torsional Balance

The microNetwon torsional balance (figure G.4) is a torsional pendulum type thrust stand with pivot bearings for motion control based on a design by Dr. Andrew

Figure G.3.: Blower, pump, and diffusion pump for the large vacuum chamber.

Ketsdever. Thrust measurements are made by calculating the force required to cause the deflection measured by the electrical signal from the linear variable differential transformer. The thrust stand is mounted on a platform that is suspended by springs inside of the thrust chamber to dampen vibrations from the pumps, building infrastructure, and airport and train noise. Calibration is conducted by electrostatic fins at atmospheric pressure. The thrust stand data is exported to a computer outside of the chamber via ethernet cables. The thrust stand was constructed in 2011 by Dr. Tony Cofer.

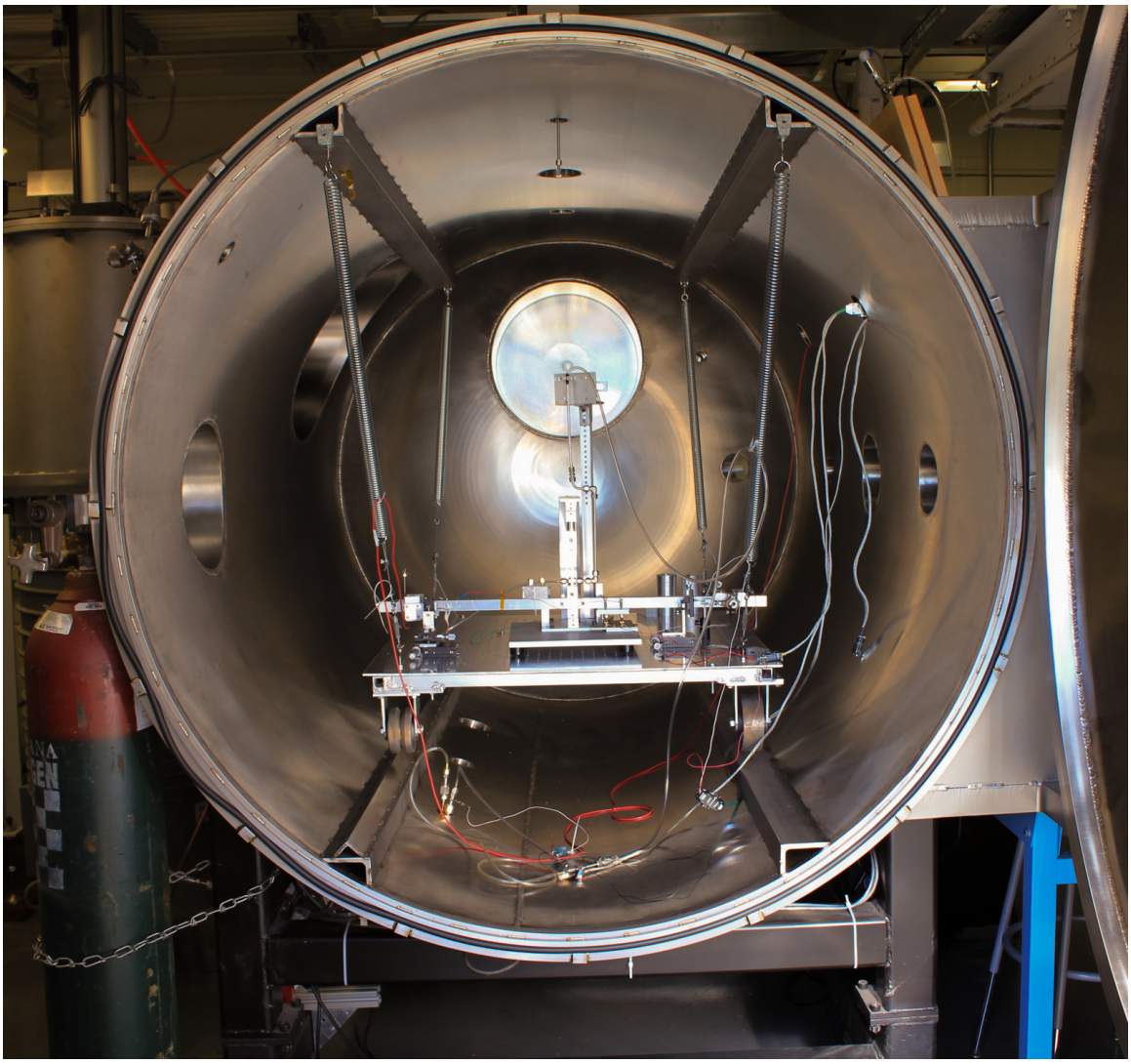

Figure G.4.: Inside of the large chamber with a view of the microNewton torsional balance.

H. Mathematical Model Graphical Outputs

The plots in this appendix were generated using the mathematical model used for the trade study. The mathematical model used a rudimentary bang bang style controller that would thrust in one direction for 5 seconds, remain idle for 5 seconds, and thrust in the opposite direction for 5 seconds. These plots were used to verify that the angle trajectories were correct in the model. The final angle is the critical information gained from this model.

The model was used for 1U, 3U, 6U, and 12U CubeSats. Each figure describes a different axes of rotation. For the 1U Cubesat, the symmetry of the body results in every axis passing through the same angle due to the torque from the thruster. Similarly, the 3U and 6U CubeSats have the same angle of rotation through the x and y axis due to the geometry of the body.

The model assumed

- Even Mass distribution
- Constant moment of inertia
- No environmental torques

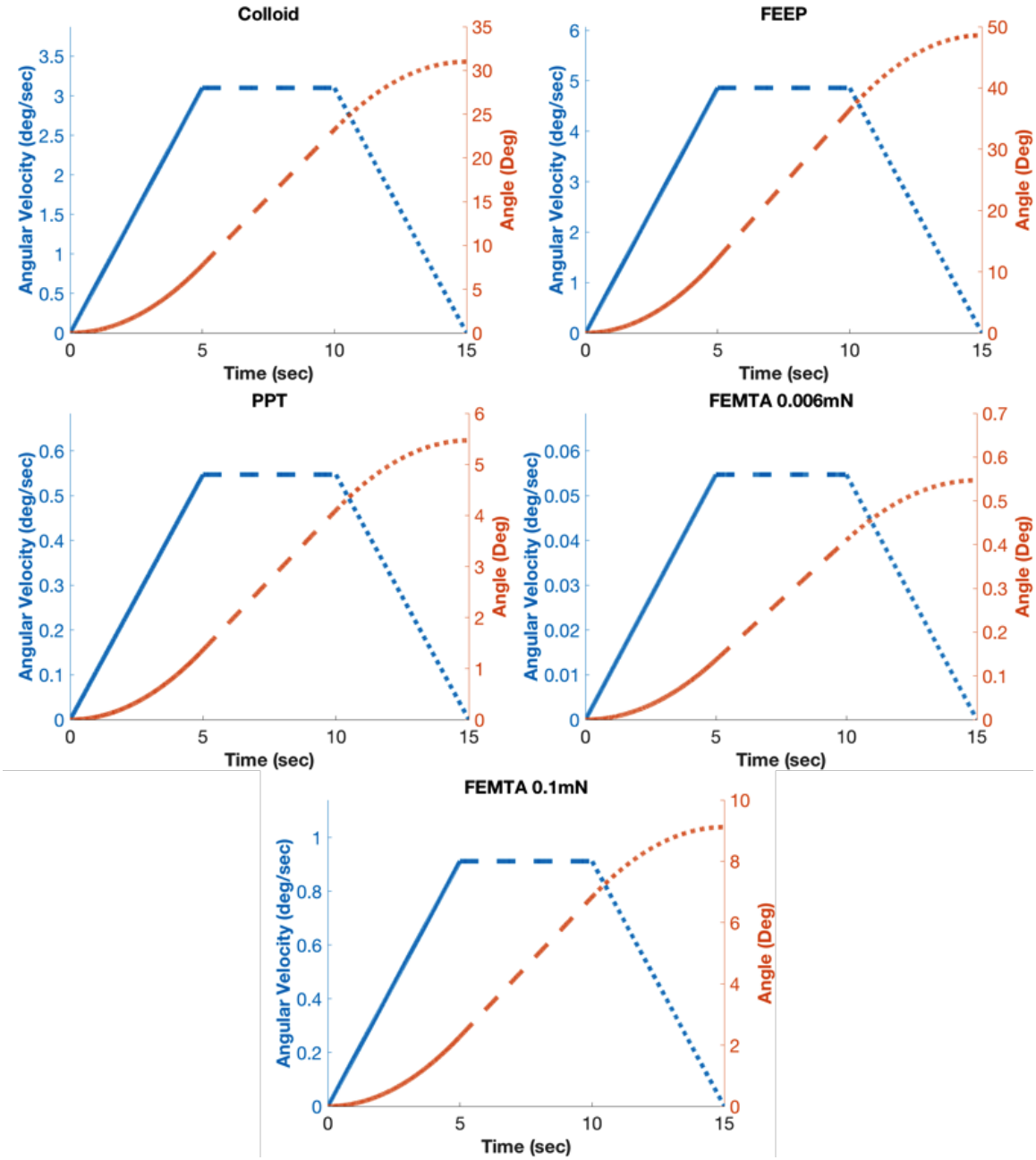

Figure H.1.: 1U rotation for x, y, and z axes

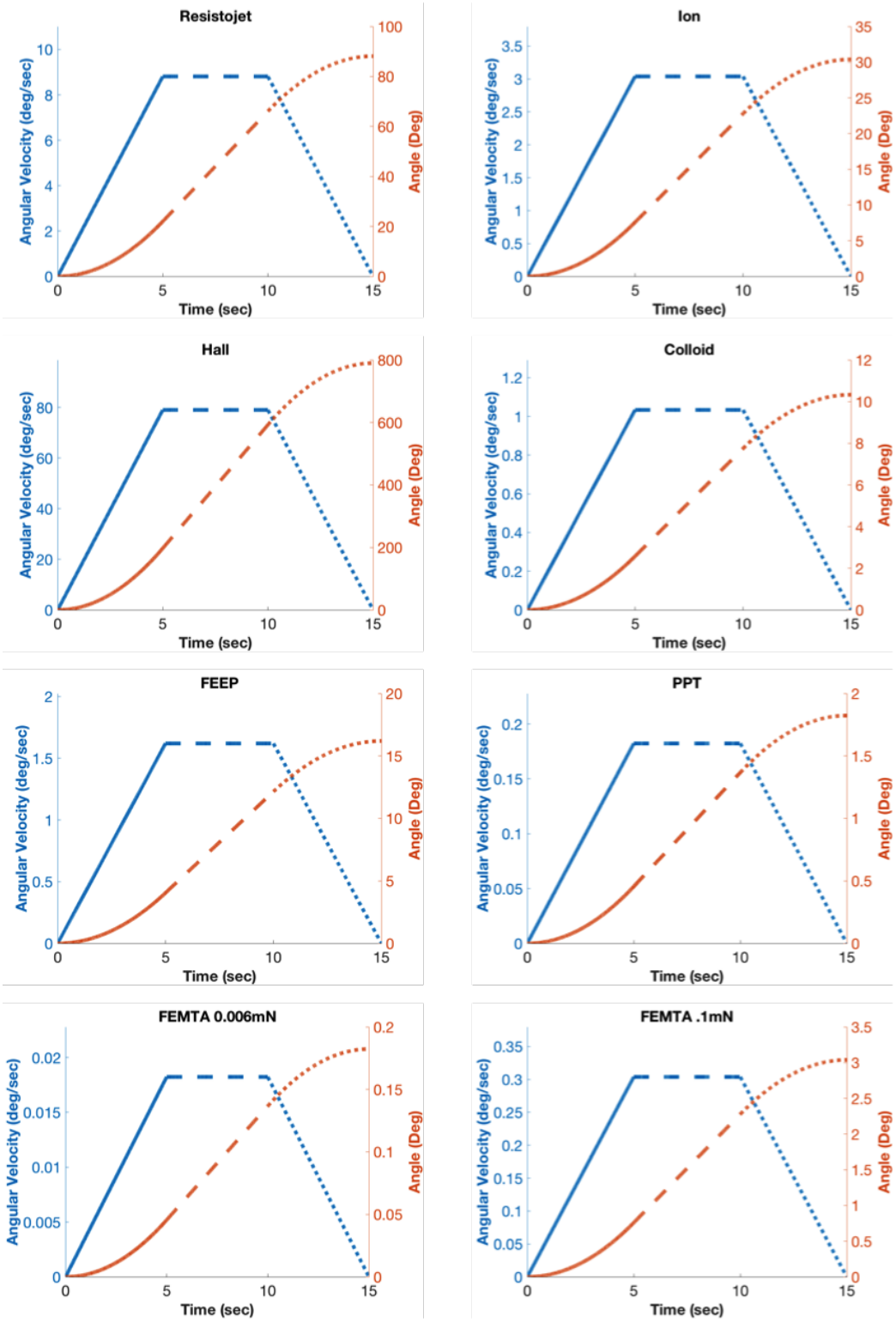

Figure H.2.: 3 U rotation for z axis

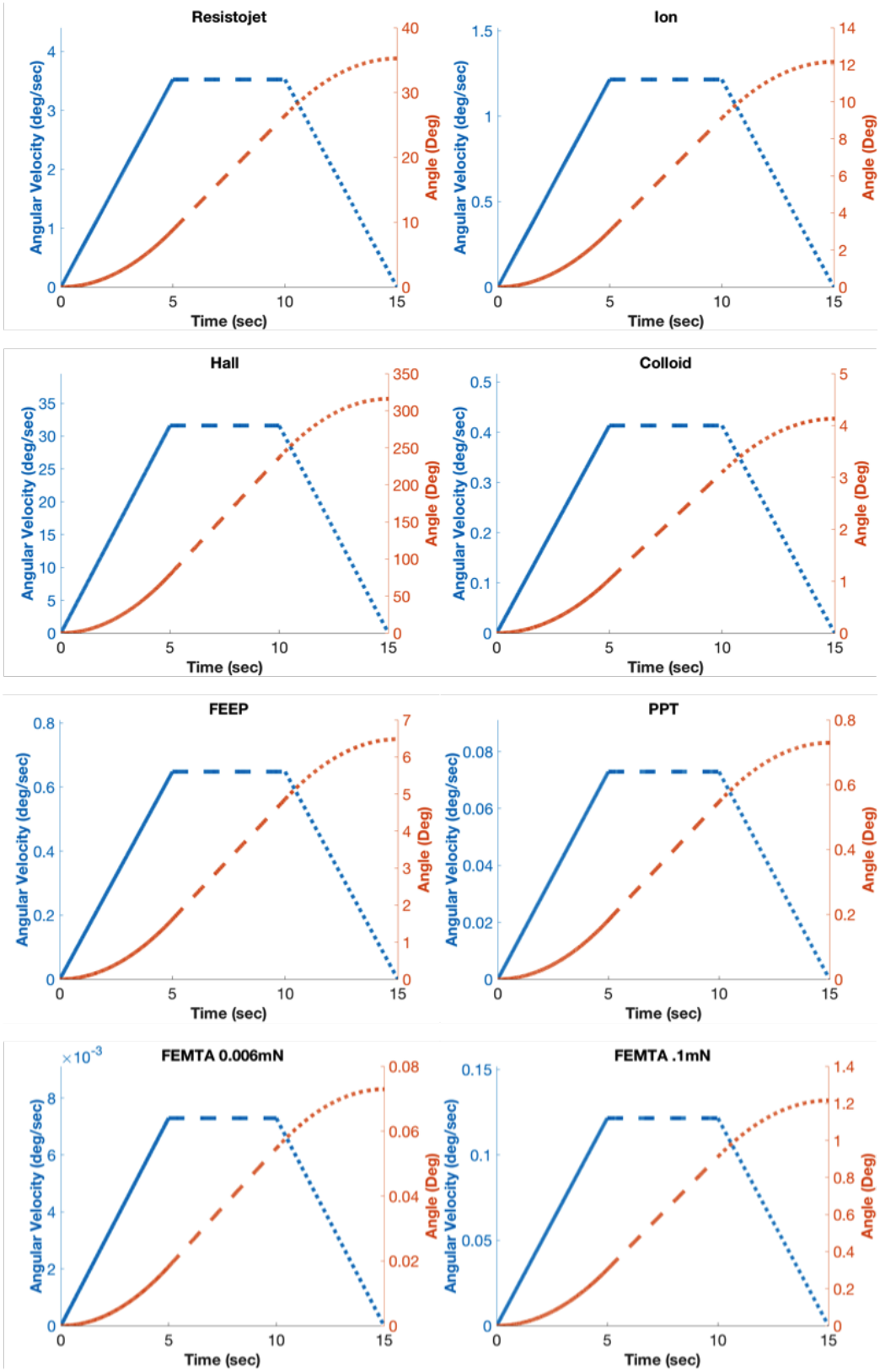

Figure H.3.: 3U rotation for x and y axes

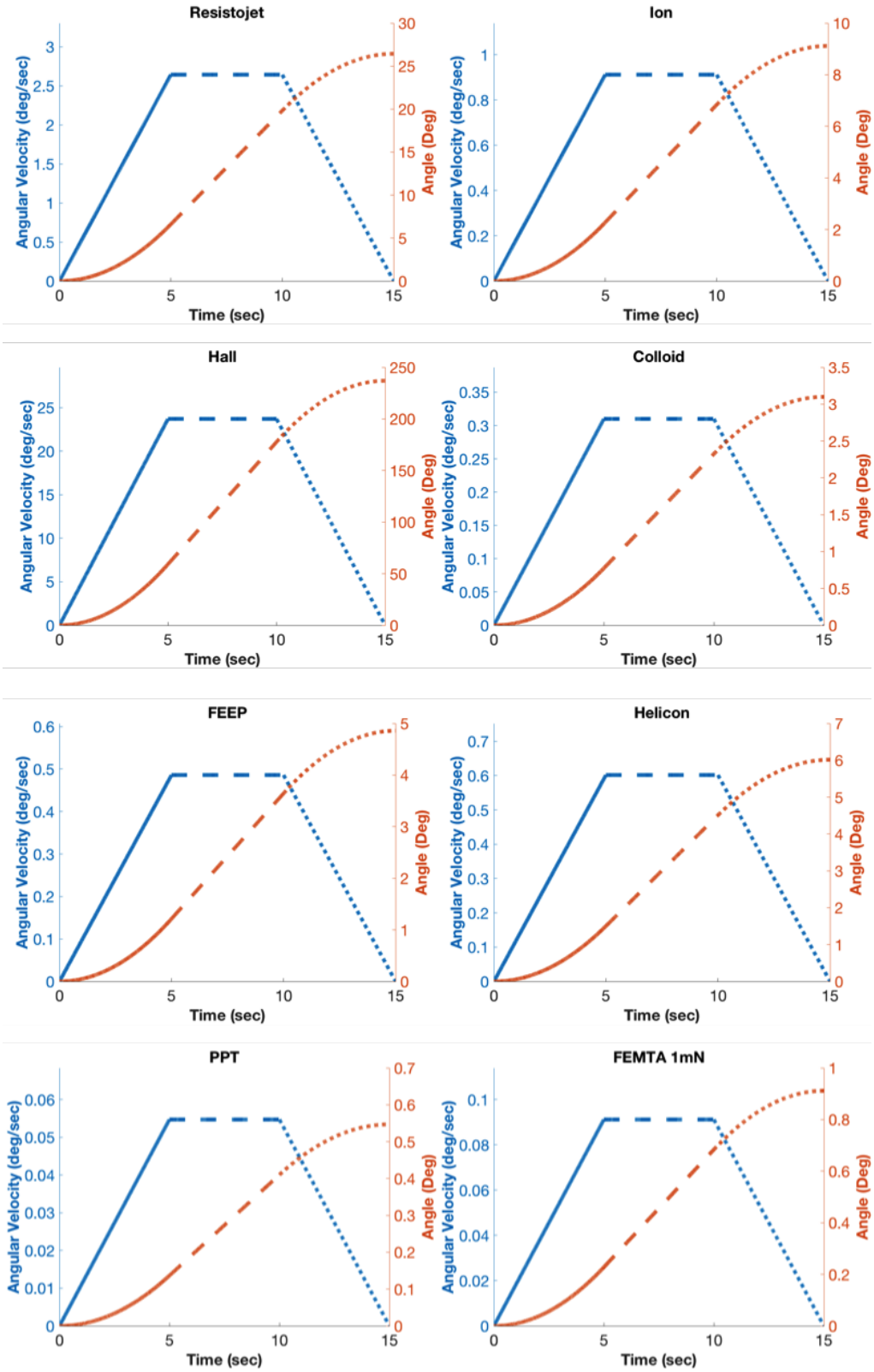

Figure H.4.: 6U rotation for z axis

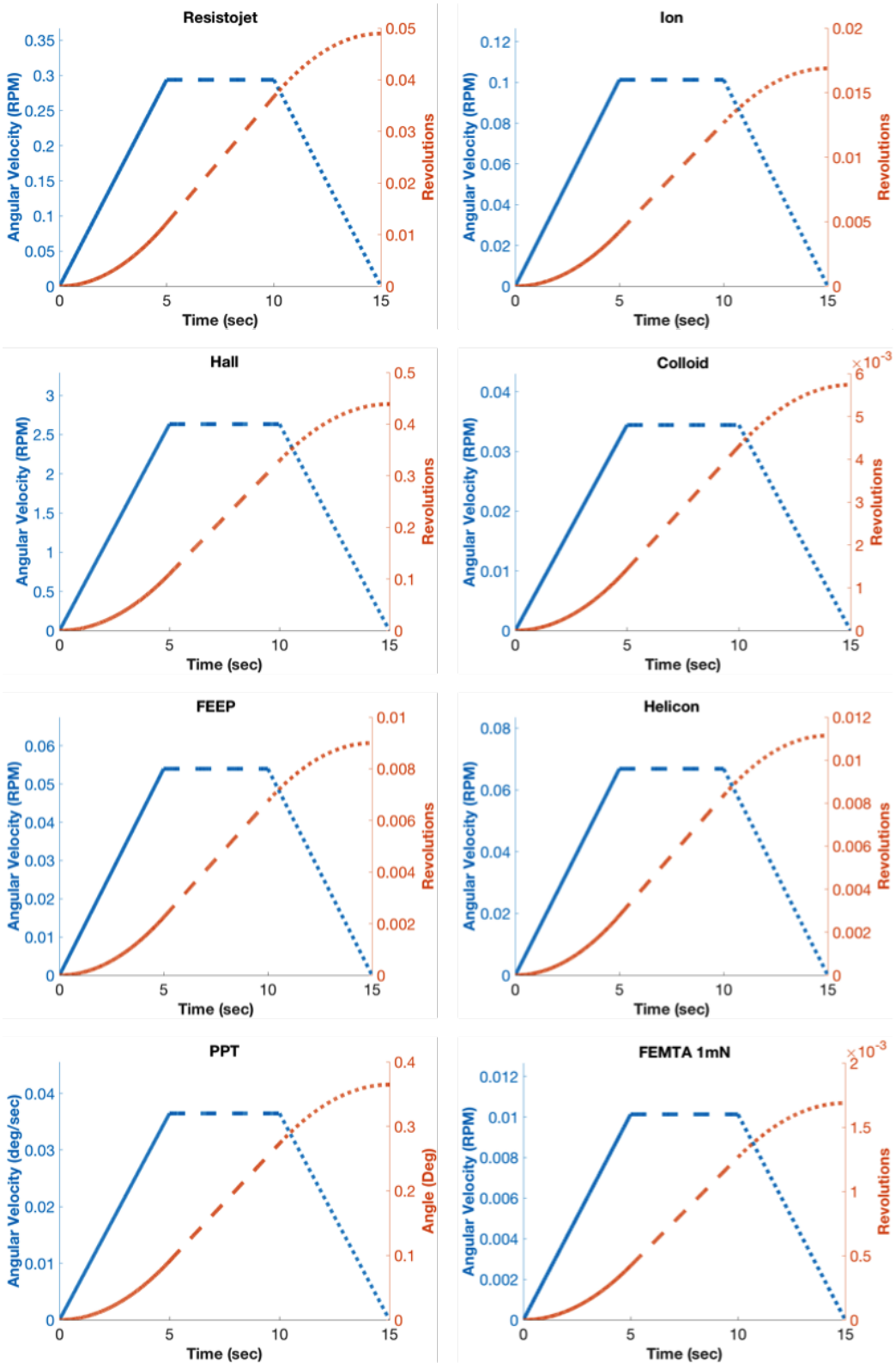

Figure H.5.: 6U rotation for y axis

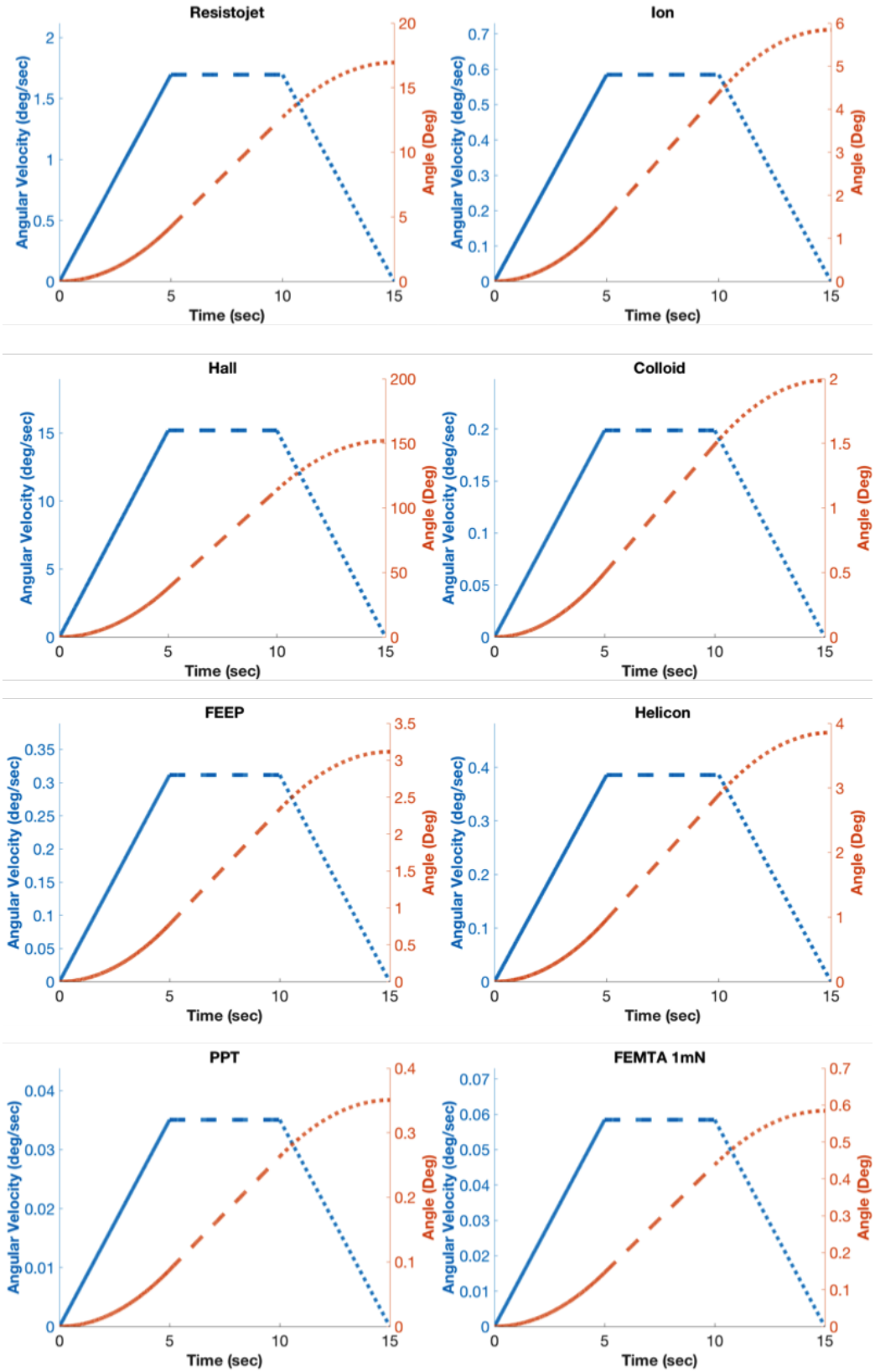

Figure H.6.: 6U rotation for x axis

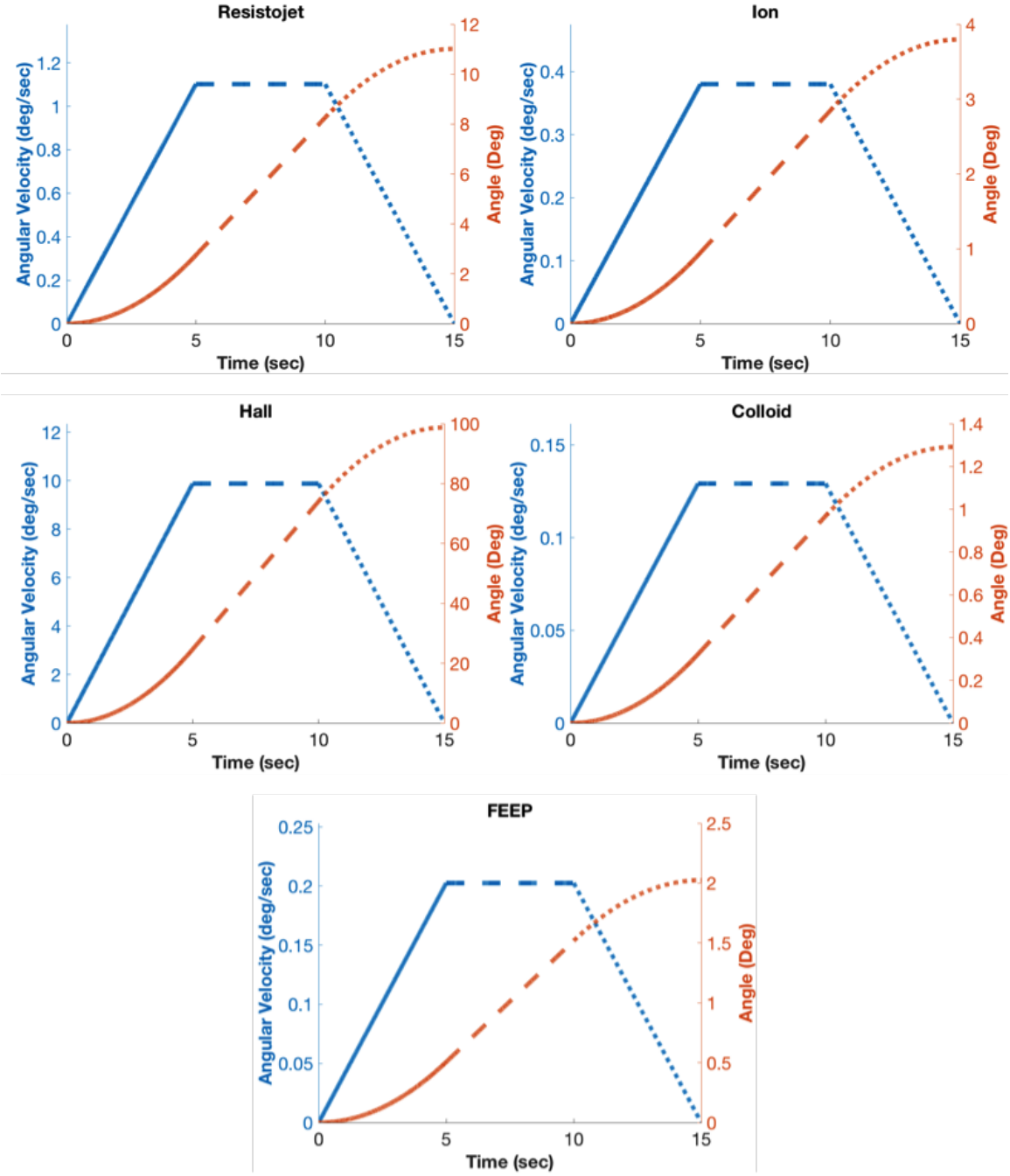

Figure H.7.: 12U rotation for z axis

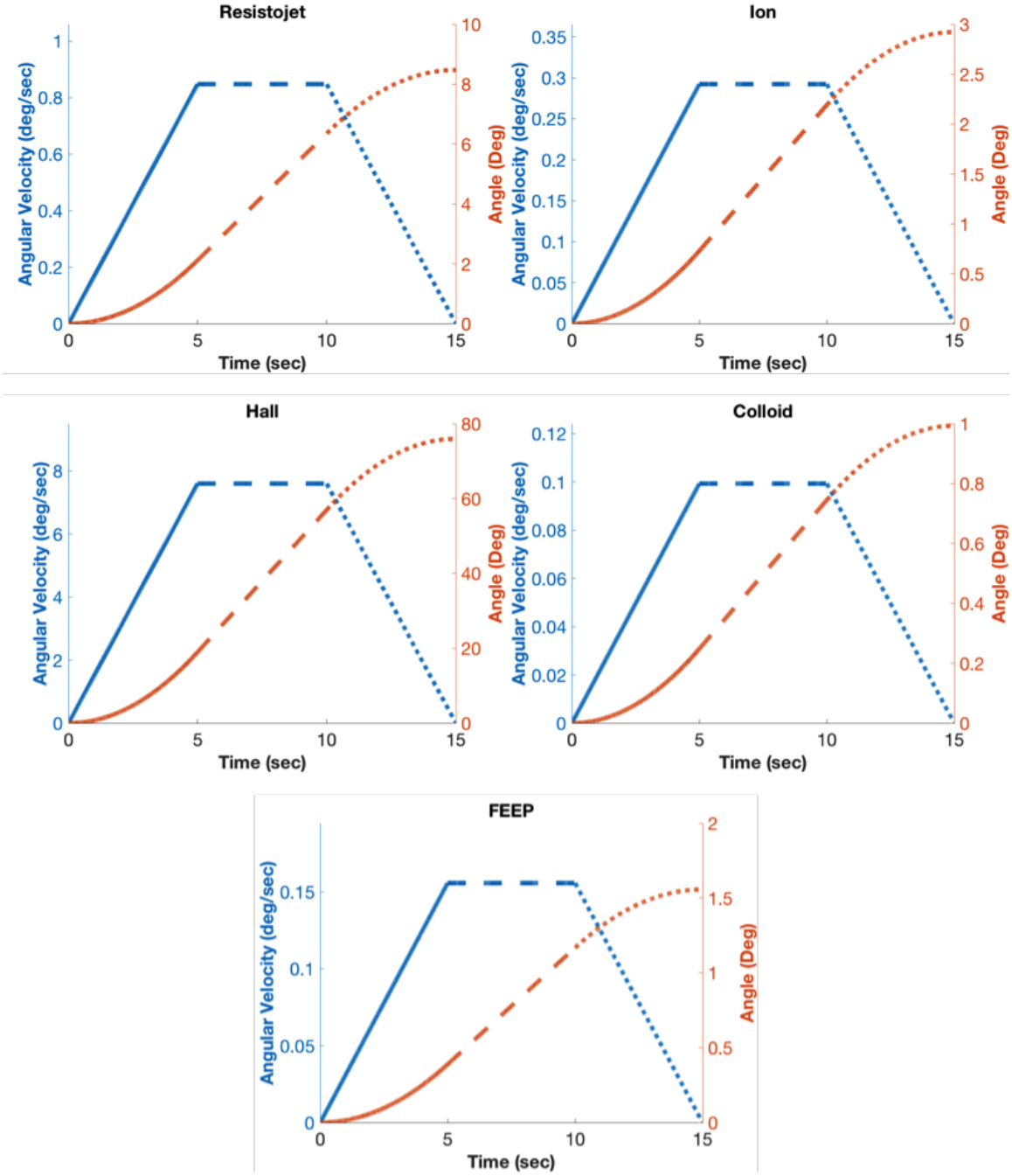

Figure H.8.: 12U rotation for x and y axes

I. MATLAB Script for Mathematical Model

This is the MATLAB script for the mathematical model and the ODE function.

```
% Attitude Dynamics
clear all
clc
close all

string = 'Name of the Thruster';
F1 = .06e-3; %thrust from a single thruster N
F2 = 0; %thrust from a single thruster N
F3 = F1; %thrust from a single thruster N
w = 0.2; %width in meters
l = 0.2; %length in meters
h = 0.3; % height in meters
U = 12; %number of units
axis = 1; % 1- z axis rotation, 2 - yaxis rotation, 3 - x-axis rotation
num_torques = 3;
M = (1+1/3)*U; %mass of cube in kg

%inertia matrix of an even desnity distribution cube
I = (M/12)*[(l^2+h^2),0,0;0,(w^2+h^2),0;0,0,(l^2+w^2)];

if axis ==1
    % zaxis rotation
    riz = [-(w/2);l/2;0]; %position vector from geometric center, M
    rcom = [0;0;0]; %position vector from g center to center of gravity, M
    reffz = riz - rcom; %effective position vector
    niz = [-sind(45);-sind(45);0]; % vector thrust direction

    Ft1 = F1*(cross(reffz,niz)); %Torque from the thruster
```

```
    Ft2 = F2*(cross(reffz,niz)); %Torque from the thruster
    Ft3 = F3*(cross(reffz,-niz)); %Torque from the thruster
    disp('z axis')
elseif axis == 2
    % yaxis rotation
    riy = [(w/2);0;h/2]; %position vector from geometric center, M
    rcom = [0;0;0]; %position vector from g center to center of gravity, M
    reffy = riy - rcom; %effective position vector
    niy = [sind(45);0;-sind(45)]; % vector thrust direction

    Ft1 = F1*(cross(reffy,niy)); %Torque from the thruster
    Ft2 = F2*(cross(reffy,niy)); %Torque from the thruster
    Ft3 = F3*(cross(reffy,-niy)); %Torque from the thruster
    disp('y axis')
else
    % xaxis rotation
    rix = [0;l/2;h/2]; %position vector from geometric center, M
    rcom = [0;0;0]; %position vector from g center to center of gravity, M
    reffx = rix - rcom; %effective position vector
    nix = [0;-sind(45);sind(45)]; % vector thrust direction

    Ft1 = F1*(cross(reffx,nix)); %Torque from the thruster
    Ft2 = F2*(cross(reffx,nix)); %Torque from the thruster
    Ft3 = F3*(cross(reffx,-nix)); %Torque from the thruster
    disp('x axis')
end



T(:,1) = Ft1; % torque definition
T(:,2) = Ft2;
T(:,3) = Ft3;
e = [0 0 0]';
e4 = 1;
w = [0 0 0]';
```

```
Interval = [0 5];

%% ode45
IC = [e;e4;w];
mx_stp = 1e-3;
Tol = 1e-8;
options = odeset('MaxStep',mx_stp,'RelTol',Tol,'AbsTol',Tol);
t0 = 0;
theta = [0,0,0];
precession(1) = 0;
nutation(1) = 0;
spin(1) = 0;
for ii = 1:num_torques %runs code for each torque

% solve the equation of motion with the function att_dyn.m
X = ode45(@att_dyn,Interval,IC,options,T(:,ii),I);
figure(1)
hold on
yyaxis left
if axis == 1
    plot(X.x+t0,(X.y(7,:)*180/pi)/(360)*60,'linewidth',5)
elseif axis == 2
    plot(X.x+t0,X.y(6,:)*180/pi/(360)*60,'linewidth',5)
    disp('y axis')
else
     plot(X.x+t0,X.y(5,:)*180/pi/(360)*60,'linewidth',5)
end

figure(2)
hold on
yyaxis left
if axis == 1
    plot(X.x+t0,(X.y(7,:)*180/pi),'linewidth',5)
elseif axis == 2
    plot(X.x+t0,X.y(6,:)*180/pi,'linewidth',5)
```

```
    disp('y axis')
else
     plot(X.x+t0,X.y(5,:)*180/pi,'linewidth',5)
end



E1 = X.y(1,:); E2 = X.y(2,:); E3 = X.y(3,:); E4 = X.y(4,:);

C = zeros(3);
C11 = 1 - 2*E2.^2 - 2*E3.^2;
C12 = 2*(E1.*E2 - E3.*E4);
C13 = 2*(E3.*E1 + E2.*E4);
C21 = 2*(E1.*E2 + E3.*E4);
C22 = 1 - 2*E3.^2 - 2*E1.^2;
C23 = 2*(E2.*E3 - E1.*E4);
C31 = 2*(E3.*E1 - E2.*E4);
C32 = 2*(E2.*E3 + E1.*E4);
C33 = 1 - 2.*E1.^2 - 2*E2.^2;

%change the euler angles into degrees
nutation_raw = -sind(C31);
precession_raw = asind(C21./(cosd(nutation_raw)));
spin_raw = asind(C32./cosd(nutation_raw));

%ensure the angles continue with the correct oscillation
for n = 1:length(precession_raw)-1
    precession(n+1)=abs(precession_raw(n+1)-precession_raw(n))+precession(n);
end

for n = 1:length(nutation_raw)-1
    nutation(n+1)=abs(nutation_raw(n+1)-nutation_raw(n))+nutation(n);
end

for n = 1:length(spin_raw)-1
    spin(n+1)=abs(spin_raw(n+1)-spin_raw(n))+spin(n);
```

```
end


figure(1)
yyaxis right
if axis == 1
plot(X.x+t0,(precession)/360,'linewidth',5)
elseif axis == 2
plot(X.x+t0,nutation/360,'linewidth',5)
disp('y axis')
else
plot(X.x+t0,spin/360,'linewidth',5)
end


figure(2)
yyaxis right
if axis == 1
plot(X.x+t0,(precession),'linewidth',5)
elseif axis == 2
plot(X.x+t0,nutation,'linewidth',5)
disp('y axis')
else
plot(X.x+t0,spin,'linewidth',5)
end
precession(1) = precession(end);
nutation(1) = nutation(end);
spin(1) = spin(end);

IC = X.y(:,end);
t0 = t0+Interval(end);

end
if axis == 1
disp(precession(end)/360)
```

```
disp(precession(end))
elseif axis ==2
disp(nutation(end)/360)
disp(nutation(end))
else
disp(spin(end)/360)
disp(spin(end))
end

h=figure(1);
label_size = 20;
set(gca, 'FontSize', 20)
ylabel('Revolutions','fontsize',label_size,'FontWeight','bold')
title(string, 'fontsize',label_size);
yyaxis left
xlabel('Time (sec)','fontsize',label_size,'FontWeight','bold')
ylabel('Angular Velocity (RPM)','fontsize',label_size,'FontWeight','bold')

if axis ==1
    ylim([0, X.y(7,1)*180/pi/360*60/4+X.y(7,1)*180/pi/360*60])
elseif axis == 2
    ylim([0, X.y(6,1)*180/pi/360*60/4+X.y(6,1)*180/pi/360*60])
else
    ylim([0, X.y(5,1)*180/pi/360*60/4+X.y(5,1)*180/pi/360*60])
end

figure(2)
label_size = 20;
set(gca, 'FontSize', 20)
ylabel('Angle (Deg)','fontsize',label_size,'FontWeight','bold')
title(string, 'fontsize',label_size);
yyaxis left
xlabel('Time (sec)','fontsize',label_size,'FontWeight','bold')
ylabel('Angular Velocity (deg/sec)','fontsize',label_size,'FontWeight','bold')
if axis ==1
```

```
    ylim([0, X.y(7,1)*180/pi/4+X.y(7,1)*180/pi])
elseif axis == 2
    ylim([0, X.y(6,1)*180/pi/4+X.y(6,1)*180/pi])
else
    ylim([0, X.y(5,1)*180/pi/4+X.y(5,1)*180/pi])
end


function [ X] = att_dyn( t,x,T,I )


e = x(1:4);
w = x(5:7);
%  E = [e(4) -e(3) e(2) e(1);...
%       e(3) e(4) -e(1) e(2);...
%       -e(2) e(1) e(4) e(3);...
%       -e(1) -e(2) -e(3) e(4)];
w_dot = I\(T - cross(w,I*w));
e_dot = .5*e(4)*w+cross(e(1:3),w);
e4_dot = -.5*dot(w,e(1:3));
X = [e_dot;e4_dot;w_dot];
end
```